

# INFERRING THE COMPOSITIONS AND INTERIOR STRUCTURES OF SMALL PLANETS

By

David R. Rice

Bachelor of Arts – Integrated Science  
Bachelor of Arts – Physics and Astronomy  
Bachelor of Arts – Earth and Planetary Sciences  
Northwestern University  
2016

Master of Science – Astronomy  
University of Nevada, Las Vegas  
2019

A dissertation submitted in partial fulfillment  
of the requirements for the

Doctor of Philosophy – Astronomy

Department of Physics and Astronomy  
College of Sciences  
The Graduate College

University of Nevada, Las Vegas  
May 2023

## Abstract

Although there are now over 10,000 confirmed and candidate extrasolar planets, accurate masses and radii have been determined for around 200 planets of less than 10 Earth-masses. This number will grow exponentially over the next decade as extreme precision radial velocity spectrographs see first light. The densities of small planets hint at a diverse range of compositions for terrestrial worlds from super-Mercuries to super-Ganymedes. Uncertainty in density is as low as 3% in the Trappist-1 system. To determine composition from observed parameters, the community uses a variety of interior structure models. Underlying these models are multiple computational techniques, numerous experimental measurements and theoretical estimates of the equations of state for planet-building materials, and differing treatments of temperature. I present MAGRATHEA, an open-source interior structure solver which can be customized to user-defined planet models for reproducible characterizations. Our code features adaptable phase diagrams for the core, mantle, hydrosphere, and atmosphere and transparent storage for equations of states. I demonstrate how I use MAGRATHEA in concert with high-pressure physicists to improve our interior models and with observational data to characterize planets. While previous works have looked at how models affect mass-radius relationships, I carry through uncertainties to the characterization of small planets with known density. I show how observed, model, and experimental uncertainties affect inferences of water mass fraction in the Trappist-1 system. The Earth's composition and interior structure can soon be understood in the greater context of exoplanet diversity.

## Acknowledgements

My advisor, Dr. Jason H. Steffen, has supported and motivated me throughout this work. I thank him for his many years of advising. I thank Dr. Chenliang Huang for his partnership in developing our interior code. I acknowledge the valuable discussions and feedback from my research group—Dr. Anna Childs, Cody Shakespeare, Nick Juliano, Stanley Baronett, Bo Royer, Abigail Graham, and Noah Ferich along with many other colleagues at UNLV and across the world. I acknowledge support from the Department of Physics and Astronomy, Nevada Center for Astrophysics, and the College of Sciences at the University of Nevada, Las Vegas. This work was supported by a 2018 Graduate Fellowship from The Nevada Space Grant Consortium, UNLV Graduate Assistantships, the Graduate College Rebel Research and Mentorship Program, and a 2023 UNLV President’s Foundation Graduate Research Fellowship. Computational resources were provided by the Cherry Creek Cluster at the UNLV National Supercomputing Institute.

I am forever thankful for the love and support of my parents, sister, and family in-law. My wife, Nicole Rice, is the brightest star in my life and has been the foundation that made the completion of this work possible.

## Table of Contents

Abstract .....	iii
Acknowledgements .....	iv
List of Tables .....	vii
List of Figures .....	viii
Chapter 1 Introduction .....	1
1.1 Small Exoplanet Demographics .....	1
1.2 Main Components of Small Planet Interiors .....	5
1.2.1 Cores .....	6
1.2.2 Mantles .....	7
1.2.3 Volatile Layers .....	8
1.3 Planet Interior Solvers .....	9
1.3.1 Applications to Small Planets .....	12
1.4 Overview .....	13
Chapter 2 MAGRATHEA: an Open-Source Spherical Symmetric Planet Interior Structure Code	14
2.1 Background .....	14
2.2 Interior Structure Solver .....	16
2.2.1 Phase Diagrams .....	18
2.2.2 Equation of State Formulae .....	20
2.2.3 Tabulated Equation of State .....	26
2.2.4 User-Defined Function .....	26
2.3 Overview of the Code Structure .....	27
2.3.1 Solver .....	27
2.3.2 Simplified Two Layer Mode .....	29
2.3.3 Phase Diagram Implementation .....	30
2.3.4 Built-In Equations of State .....	31
2.3.5 Core/Iron .....	33
2.3.6 Mantle/Silicate .....	33
2.3.7 Hydrosphere/Water .....	34
2.3.8 Atmosphere/Gas .....	36
2.4 Known Limitations .....	38
2.5 Test Problems and Utility .....	39
2.5.1 One-Earth Mass and Comparison with ExoPlex .....	39
2.5.2 Run Time .....	41

2.5.3	Uncertainty from Equation of State .....	43
2.5.4	Ternary Diagram .....	45
2.5.5	Ternary with Atmosphere .....	49
2.6	EoS Storage Structure .....	49
2.7	Modify a Built-In EoS in Runtime .....	54
2.8	Summary .....	56
Chapter 3	Further MAGRATHEA Developments .....	57
3.1	Background .....	57
3.2	Composition Finder .....	58
3.3	3D Planet Rendering .....	63
3.4	Summary and Future Development .....	67
Chapter 4	Advancements in EoS and Expansion of EoS Library .....	71
4.1	Background .....	71
4.2	New Water-Ice Experimental EoS .....	73
4.3	Core Iron EoS .....	76
4.4	FCC and BCC Iron .....	79
4.5	Upper Mantle Materials .....	81
4.6	Summary and Future Work .....	85
Chapter 5	Characterizing the Composition of Planets .....	89
5.1	Background .....	89
5.2	K2-138 Planetary System .....	90
5.3	Water Worlds and Super Earths .....	97
5.4	TRAPPIST-1 Planets from Formation Models .....	102
5.5	Summary .....	105
Chapter 6	Uncertainties in Inferences of Internal Structure .....	107
6.1	Background .....	107
6.2	Graphical Representations .....	109
6.3	TRAPPIST-1 System Default Compositions .....	113
6.3.1	T1f Default Model .....	115
6.4	T1f Uncertainties .....	118
6.4.1	Observational .....	118
6.4.2	Model Choices .....	122
6.4.3	Experimental .....	124
6.5	Summary .....	127
Chapter 7	Conclusion .....	128
References	.....	132
Curriculum Vitae	.....	146

## List of Tables

2.1	List of status information of the planet profile object .....	29
2.2	EoS parameters for Smith et al. (2018), Sakai et al. (2016), and Grande et al. (2022) with uncertainty and the uncertainty in radius for a $10 M_{\oplus}$ single-layer planet from uncertainty in EoS parameters. ....	44
2.3	Index for types of isothermal EoS formulae .....	50
2.4	Temperature profile option .....	51
2.5	List of EoS parameters .....	52
3.1	Inputs for the composition finder with line numbers in <i>main.cpp</i> . ....	59
4.1	Frank et al. (2004) and Grande et al. (2022) best fit EoS parameters. The Zeng et al. (2016) paper uses a different parameterization for their EoS (see Zeng & Sasselov 2013). ....	75
5.1	Core mass fraction (cmf), mantle mass fraction (mmf), water mass fraction (wmf) and resulting radius for the T1 planets using the average bulk compositions from the simulated planets. We report these properties for starting bodies with a wmf of 0.20 and 0.50. ....	103
6.1	2,500 samples of mass and radius were generated for each row of properties and with median values of Trappist-1f. Uncertainty in wmf shown at 0.33 and 0.60 r-cmf. Final column is uncertainty in cmf at 0% wmf. ....	118
6.2	2,500 samples of radius were generated from skewed distributions and paired with with masses drawn from a Gaussian with $1.039 \pm 0.31 M_{\oplus}$ . <i>Skew</i> is the Fisher-Pearson coefficient of skewness. <i>Earth W%</i> is the wmf % at a given 0.33 RCM. ....	120

## List of Figures

1.1	The bulk density with planet mass of confirmed exoplanets with both accurately determined mass and radius. Null-albedo equilibrium temperature of the planets are represented by color. Three lines of constant interior structure are shown for 100% core, 100% mantle, and 100% water planets. ....	2
1.2	The works that inform the planet interior model in two recent planet interior works—Acuña et al. (2021) and Dorn & Lichtenberg (2021). Tree structure shows previous works the models are built upon which are not all cited in the top-level paper. Works color coded by layer they inform. Works in figure: Brugger et al. (2016; 2017); Sotin et al. (2007); Valencia et al. (2007b); Frank et al. (2004); Duffy et al. (1995); Bouhifd et al. (1996); Vacher et al. (1998); Anderson et al. (1991); Lide (2002); Fei et al. (1993); Poirier (2000); Stixrude & Lithgow-Bertelloni (2005); Tsuchiya et al. (2004); Williams & Knittle (1997); Uchida et al. (2001); Mousis et al. (2020); Mazevet et al. (2019); Báez & Clancy (1995); Tulk et al. (1997); Tchijov (2004); Shaw (1986); Feistel & Wagner (2006); Bezacier et al. (2014); Dunaeva et al. (2010); Dorn et al. (2015; 2017b); Hakim et al. (2018); Miozzi et al. (2020); Dorogokupets et al. (2017); Ichikawa & Tsuchiya (2020); Kuwayama et al. (2020); Anzellini et al. (2013); Stixrude (2014); Connolly (2009); Stewart et al. (2020); Faik et al. (2018); Melosh (2007); Belonoshko et al. (2005a); Stixrude (2014; 2012); Haldemann et al. (2020); Journaux et al. (2020); Wagner & Pruß (2002); Brown (2018); Gordon & McBride (1994); McBride & Gordon (1996); Mazevet et al. (2019). ....	11
2.1	A schematic overview of MAGRATHEA. Showing an example input, <i>left</i> , of a $1.1 M_{\oplus}$ planet with $0.4 M_{\oplus}$ core, $0.4 M_{\oplus}$ mantle, and $0.3 M_{\oplus}$ hydrosphere. The planet is not in thermal equilibrium with a surface temperature of 300 K and jumps in temperature across boundary layers of 600 K and 1200 K. <i>Center</i> , shows MAGRATHEA’s four input layers with cartoons of phase diagrams defined for each layer with an EoS chosen for each phase. Default phase diagrams shown in Fig. 2.2. <i>Right</i> , shows the pressure and temperature with enclosed mass. The radius at boundaries and the planet radii is also shown. ....	19
2.2	Default phase diagrams for hydrosphere, mantle, and core layers. EoS and phase transitions from a variety of sources detailed in Sec. 2.3.4. Type of EoS fitting equation shown from Sec. 2.2.2. Additionally, the parameters for mantle EoSs are shown, <i>middle</i> . The phase diagrams and choice of EoS can be customized by the user. <i>N.I.</i> is <i>not implemented</i> . The atmosphere layer also has a phase function, but our default is ideal gas at all pressure and temperatures, see Sec. 2.3.8 ....	20

2.3	<i>Top</i> , mass-radius relationship for planets with 100 per cent of mass in either the core, mantle, or hydrosphere demonstrating many of the EoSs implemented in MAGRATHEA. <i>Bottom</i> , percent difference in final planet radii compared to our selected “default” EoSs for water ( <i>top</i> ), mantle ( <i>middle</i> ), and core ( <i>bottom</i> ). Table lists the major components of each model with 300 K surface temperature unless designated with a “-2000”. Near the surface, water planets have water and Ice VI, and hot mantle planets have silicate melt. ....	32
2.4	Density, pressure, and temperature verses radius solution for a two-layer, one Earth-mass planet with 33 per cent by mass core. The three models shown are <i>Magrathea Default</i> with hcp-Fe core (Smith et al. 2018) and Brg/PPv mantle (Oganov & Ono 2004; Sakai et al. 2016), <i>Magrathea Adjusted</i> with Fe-Si alloy core (Wicks et al. 2018) and PREM mantle (Zeng et al. 2016) and a temperature discontinuity, and the default settings in <i>ExoPlex</i> . <i>Magrathea Default</i> is set to 300 K at the surface while <i>ExoPlex</i> suggests a 1600 K mantle. Temperature is solved throughout <i>Magrathea Default</i> and in <i>ExoPlex</i> ’s mantle. <i>Magrathea</i> returns no change in temperature when a phase does not have temperature parameters available while <i>ExoPlex</i> returns zero Kelvin. The planet’s radius and the average run time over 100 integrations is listed in the legend. ....	40
2.5	Plot of run time, <i>top</i> , and of run time divided total number of steps, <i>bottom</i> , for our default model across six planet masses and four compositions: 100% core, 30% core 70% mantle, 30% core 40% mantle 30% water, and 30% core 40% mantle 29.99% water 0.01% H/He atmosphere with 300 K surface temperature. The last set of planets, <i>orange</i> , have 30% core, 70% mantle, and surface temperature of 2000 K. The run time is the average time measured across 100 runs. Sizes of the markers are proportional to the planet radius. ....	42
2.6	<i>Left</i> , ternary diagram where the axes are the percentage of mass in a core, mantle, and water/ice layer. The radius in Earth radii is shown by the color scale for 5151, one Earth-mass planets at integer percentages with our default model. Color map is interpolated between the simulations. <i>Right</i> , plot of MAGRATHEA’s run time for each planet. <i>Middle</i> , histogram of run time on a log-log scale showing mean time of 1.014 seconds. Ternary plots are generated with the python-ternary package by Harper et al. (2015) with colormaps from Van der Velden (2020). ....	46
2.7	Core-Mantle-Water mass percentage ternary plot with colored contours of constant radius for one Earth-mass planets. Four types of planets, represented by the line-style, are calculated: one with no atmosphere and three with 0.01 per cent of their mass in an atmosphere layer. The atmosphere mass was subtracted equally from both the mantle and core to keep total mass equal to one Earth-mass. The three atmospheres have varying mean molecular weight: CO <sub>2</sub> with 44 g mol <sup>-1</sup> , H <sub>2</sub> O with 18 g mol <sup>-1</sup> , and H/He mixture with 3 g mol <sup>-1</sup> . ....	48
3.1	<i>Left</i> , a Blender rendering of an Earth-like planet with 32.5% of mass in the core with changes in mineralogy marked by changes in color in the interior. <i>Right</i> , in <i>blue</i> the density, pressure, and temperature of the Earth-like planet compared to a isothermal profile for PREM mantle and hcp-iron core. The radius of discontinuities in density on <i>top right</i> correspond with changes in color in 3D <i>left</i> . ....	65



3.2	<i>Top</i> , 100% mantle planets. <i>Bottom</i> , planets with significant hydrospheres. <i>Top left</i> , planet that is $1 M_{\oplus}$ and $1.07 R_{\oplus}$ surface of 300 K. <i>Top right</i> , planet that is $1.1 M_{\oplus}$ and $1.1 R_{\oplus}$ and surface of 1000 K. The second planet's temperature leads to a wds layer shown in green/grey under the olivine layer. <i>Bottom left</i> , planet that is $0.63 M_{\oplus}$ and $0.97 R_{\oplus}$ with 42% core. <i>Bottom, right</i> , planet that is $0.56 M_{\oplus}$ and $0.99 R_{\oplus}$ with 35% core. ....	66
3.3	The density inside the Earth-like planet in Fig. 3.1. The density increases fairly linearly in the mantle with density jumps in the liquid outer core and solid inner core. The current method does not resolve the upper mantle materials well. Colors are rendered differently in Blender based on lighting and other "material properties" of the 3D sphere so may not correspond exactly to the colorbar. ....	68
4.1	The density with depth of two $1 M_{\oplus}$ planets made of pure gold and platinum. This is for illustrative purposes as planets are not made out of pure gold and platinum. Inset shows percent difference between the two planets' densities as a function of depth. ....	72
4.2	Impact of ice EoS measurements on inferences of minimum atmospheric weight for K2-18b. The three EoS shown are EOS I: Grande et al. (2022), EOS II: Zeng et al. (2016), EOS III: Frank et al. (2004). Lines show the fraction of planet mass in an atmosphere needed to reproduce the radius of K2-18b across a range of likely masses. Planets are modeled as pure water with a $3.0 \text{ g/mol}$ ideal gas atmosphere and a equilibrium temperature of 255 K. The grey areas show the one and two sigma mass bounds of K2-18b. Planets with varying atmosphere are run at each half step in sigma. The shaded regions show the atmosphere needed to reproduce the radius of K2-18b to within one sigma for each EoS. One error bar is shown at $8.63 M_{\oplus}$ . Planet parameters from Benneke et al. (2019). ....	77
4.3	Impact of iron's bulk modulus on the inferred water mass fraction of Trappist-1 f at median value of mass and radius assuming an earth like core to mantle ratio. The lower bulk modulus of Smith et al. (2018) leads to the planet needing more water to match observed characteristics. Planet parameters from Agol et al. (2021). ....	78
4.4	Grüneisen parameter as a function of density, <i>blue</i> , with error, <i>light blue</i> , from Fig. 2b in Smith et al. (2018). Relationship with best fit parameters for Eq. 2.13 shown in <i>orange</i> . ....	80
4.5	<i>Left</i> , this graph shows a mass-radius plot with comparison between planets with low pressure iron and without and with different surface temperatures. <i>Right</i> , this graph shows the percent difference between the planets with low pressure iron and without. ....	82
4.6	A phase diagram showing temperature-pressure profiles for the mantles of three masses of planets with an Earth-like 32.5% of their mass in the core and a mantle adiabat which starts at 2000 K. A diamond marks the central temperature and pressure for each planet mass. The planets pass through many phases of magnesium silicates. Depths shown for the $1 M_{\oplus}$ Earth-like planet. ....	84
4.7	<i>Left</i> , a comparison of the output radius of the models based on given 100% mantle planetary masses. <i>Right</i> , the graph displays the percentage differences between two models given in legend. ....	85

4.8	A phase diagram showing temperature-pressure profiles for the cores of planets from Fig. 4.6. Planets are simulated with a 1200 K increase in temperature at the CMB. All three cores are pure hcp Iron, but the melt curve for a iron sulfur mix is also plotted. ....	88
5.1	Mass-radius diagram with the radius and mass estimates of K2-138's planets. These estimates were pulled from normal distributions centered on the values from Lopez et al. (2019), with standard deviations equal to the uncertainties. We overplot composition curves of Earth-like (solid), 1% H/He atmosphere (short dash), and 100% water (long dash). We find that K2-138b is consistent with an Earth-like and terrestrial compositions, but that planets c-f require at least 1% H/He envelopes to satisfy their densities. ....	92
5.2	Ternary diagram where the axes are the percentage of mass in a core, mantle, and hydrosphere. Background thin lines are solutions from MAGRATHEA to 1000 samples of each planet's observed mass and radius. The wmf needed to match the observed radius is found across core:mantle ratio. Large solid lines of the corresponding planet color is the median wmf while dashed lines are the $1\sigma$ bounds. K2-138b ( <i>blue</i> ) is the only planet where all 1000 samples have non-atmosphere solutions. The median sample of K2-138c ( <i>green</i> ) and d ( <i>orange</i> ) require an atmosphere and only the $-1\sigma$ bound of wmf is shown. Grey dashed line shows a constant Earth-like core to mantle ratio. ....	95
5.3	The water and atmosphere mass needed to match 100 and 1000 observed samples of mass and radius. The remaining mass is split 33:67 into the core and mantle. Thin background lines are solutions to each sample. Solid thick lines are the mean and $1\sigma$ bounds of samples with solutions at the given water mass. An isentropic temperature profile is used with the surface temperature set to the equilibrium temperature from Lopez et al. (2019). The statistics for K2-138b are only calculated up to when half of the samples have solutions requiring more than $10^{-4}\%$ atmosphere mass. 186 samples of K2-138b are too dense to require an atmosphere mass of more than $10^{-4}\%$ . ....	96
5.4	Water-Mantle-Core mass ternary diagram with interior solutions to GJ 1252b from mass and radius in Luque & Pallé (2022). <i>Red</i> , shows the median and $1-\sigma$ bounds of valid solutions. The most-probable water mass fraction is below 50% for all r-cmf. ....	99
5.5	<i>Left</i> , nine planets reanalyzed by Luque & Pallé (2022) on a mass-radius diagram. Curves for Earth-Like (32.5% mantle, 67.5% core) and Water-World (50% water, 50% mantle) interiors shown. <i>Right</i> , plot of bulk density normalized to Earth and uncompressed density. The planets are modeled with MAGRATHEA to find the uncompressed density with uncertainty. Trappist-1 f and Solar System bodies also shown. ....	101

6.1	The two primary representations of planet composition in this chapter. <i>Left</i> , a water-mantle-core mass ternary diagram. <i>Right</i> , a water mass fraction with r-cmf (refractory core mass fraction) plot. Helpful definitions are supplied on the plot for the axes. A line of solutions for three-layer internal structure for a planet of given mass and radius at 0.01 steps in r-cmf is shown on both plots. Planets consistent with the r-cmf of Mercury and Earth shown with dashed-dotted and dotted lines. Earth and Ganymede shown on the ternary diagram. ....	111
6.2	1- and 2- $\sigma$ mass and radius for Trappist-1 d-h from Agol et al. (2021). Four lines of constant interior structure are shown. ....	113
6.3	<i>Left</i> , interior structures which match 5000 draws of mass and radius for T1d. <i>Right</i> , interior structures for T1h. <i>Red lines</i> show the median and $\pm 1\sigma$ bounds of wmf across uniform r-cmf. ....	114
6.4	<i>Top</i> , the $1\sigma$ wmf of all 5 planets across r-cmf on a ternary. <i>Bottom</i> , same as top on a wmf vs r-cmf plot with $1\sigma$ shaded. ....	116
6.5	<i>Left</i> , the wmf at uniform r-cmf which match the observations of Grimm et al. (2018). <i>Right</i> , the wmf at uniform r-cmf which match the observations of Agol et al. (2021). <i>Red lines</i> show the median and $\pm 1\sigma$ bounds of wmf across uniform r-cmf. <i>Right</i> , the wmf of Agol et al. (2021) at a given cmf and the $\pm 1\sigma$ compositions from Acuña et al. (2021). ....	117
6.6	Three likely structures of T1f visualized in Blender. In a.) the best-fit wmf for an Earth-like R-CMF with a Ice Ih surface (lightest blue). The planet still has layer of olivine (lightest green) and rwd (under olivine). In b.) the best-fit wmf for a Mercury-like R-CMF with ice X (darkest blue) layer above bridgmanite (medium green). In c.) the best-fit for no water with 14% cmf showing many mantle materials. Post-perovskite is shown in the darkest green. ....	117
6.7	The $1\sigma$ ( <i>darker dashed</i> ) and $2\sigma$ ( <i>light dotted</i> ) bounds and median in solid line of wmf with r-cmf for samples of gaussian mass and radius similar to that of T1f with varying mass uncertainty represented by the three colors. ....	119
6.8	<i>Left</i> , $1\sigma$ and $2\sigma$ ellipses of mass and radius for uncorrelated data ( <i>red</i> ), Agol et al. (2021) ( <i>blue</i> ), and highly correlated data ( <i>cyan</i> ). All distributions have the same median and standard deviation. <i>Right</i> , inferred wmf at given r-cmf for the three distributions from <i>left</i> with the shown correlation-coefficient. ....	120
6.9	<i>Top</i> , distributions of radius and density for my injected skewed distributions. <i>Bottom</i> , likely wmf of the model data with various skewness. Skew-1, Skew-2, and Skew-3 correspond to the third, fourth, and fifth data set (row) in Table 6.2, and Skew-n is the negative skewed first sample. ....	121
6.10	Wmf with four large model differences. “Default” is our default model shown in Fig. 6.5. “water” raises the surface temperature to 300 K melting the layer of ice ih. “No-RWD” ignores upper-mantle materials removing the small layer of RWD. “Melt” has a 1500 K discontinuity at the mantle-hydrosphere boundary and core-mantle boundary which creates a liquid core layer. ....	123

6.11	Wmf for the median values of mass and radius for T1f, but with varying values for experimentally determined EoSs. We vary parameters such as the bulk modulus but the uncertainty reported in the literature in 5000 draws. <i>Top</i> , uncertainty in our default EoSs. <i>Bottom</i> , uncertainty including uncertainty in the thermal conductivity of ice VII from Fei et al. (1993). . . . .	126
------	--	-----

## Chapter 1

### Introduction

#### 1.1 Small Exoplanet Demographics

There are currently 5312 confirmed planets in 3981 stellar systems outside of the Solar System<sup>1</sup>. While 4011 of these exoplanets are transiting allowing us to measure their radii from the periodic decreases in the light curve of their star, exoplanet discovery and observing techniques are diverse including pulsar timing variations (Konacki & Wolszczan 2003), radial velocity (RV) (Butler et al. 2006), astrometry (Sahlmann et al. 2013), microlensing (Bennett et al. 2008), and direct imaging (Chauvin et al. 2004). “Hot Jupiters” with large sizes and short orbital periods, which most observational techniques are biased toward, were the first exoplanet category to be discovered Mayor & Queloz (1995). These extreme worlds of expanded hot gas showed that exoplanet systems may look wildly different from the Solar System.

Discoveries such as Kepler-10b, LHS 1140b, the seven planets of the Trappist-1 system, Ross 128b, and Proxima Centuari b (Batalha et al. 2011; Dittmann et al. 2017; Gillon et al. 2017; Bonfils et al. 2018; Anglada-Escudé et al. 2016) show that small exoplanets, less than ten Earth-masses, are now also firmly within observational capabilities. While they are difficult to observe, occurrence rates show that small planets between 1-4  $R_{\oplus}$ , although not present in our solar system, are the most common type of planet in our galaxy (e.g. Batalha et al. 2013; Fressin et al. 2013; Pe-

---

<sup>1</sup>NASA Exoplanet Archive, <https://exoplanetarchive.ipac.caltech.edu/>, as of 20 March 2023

figura et al. 2013). The search for planets with bulk properties similar to Earth is a focus of many current and future space and ground based observatories such as the Transiting Exoplanet Survey Satellite (TESS) which has an expected 4000 planets yet to be confirmed (Huang et al. 2018), the PLATO (Planetary Transits and Oscillations of stars) mission which is scheduled to launch in 2026 (Heller et al. 2022), and the Extremely Large Telescope scheduled for completion in 2025 which is designed with the capabilities to image rocky planets (Udry et al. 2014).

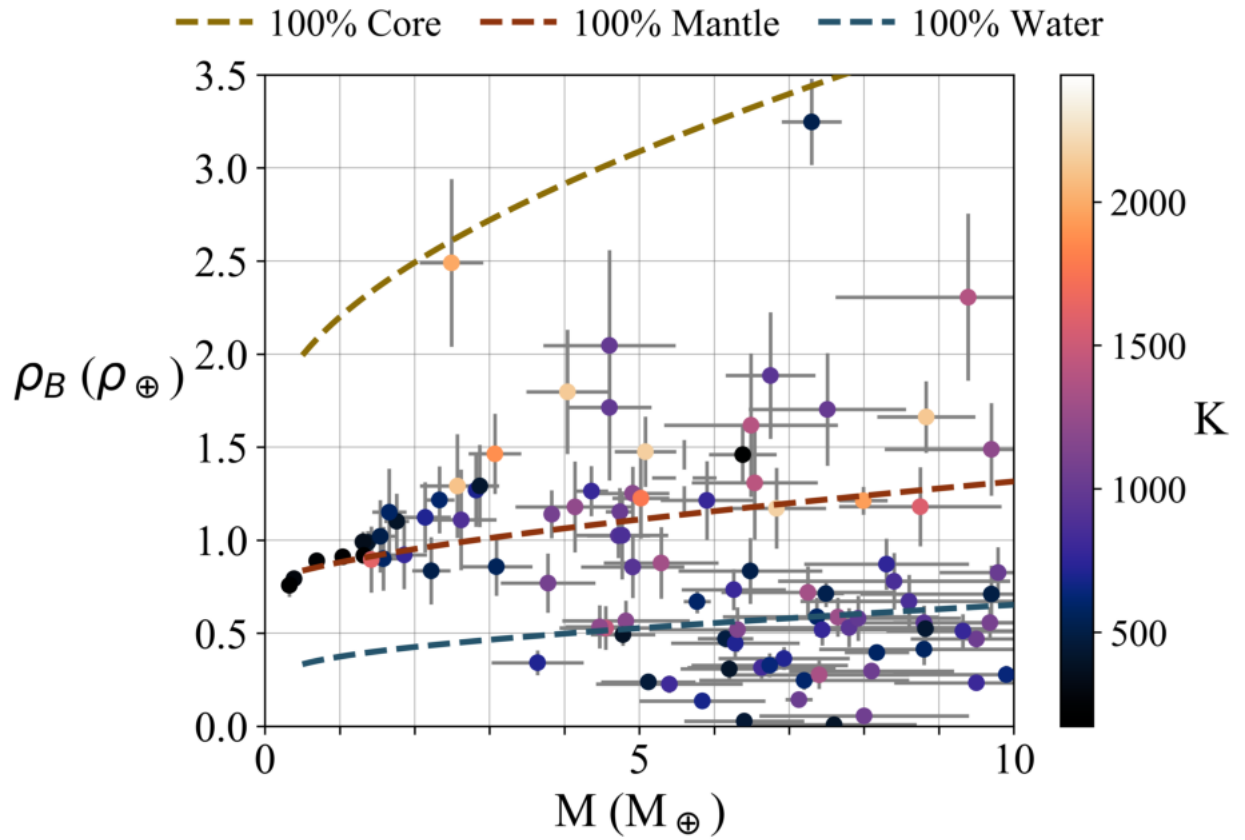


Figure 1.1: The bulk density with planet mass of confirmed exoplanets with both accurately determined mass and radius. Null-albedo equilibrium temperature of the planets are represented by color. Three lines of constant interior structure are shown for 100% core, 100% mantle, and 100% water planets.

The sample of confirmed planets gets smaller as we divide the parameter space. Only 2400 planets have a confirmed mass or projected planetary mass ( $m \sin i$ , measured by RV), and only 288 of those planets have masses less than ten times the mass of the Earth (defined as “small” in this work). Figure 1.1 shows the 98 confirmed planets with accurately determined radii and masses below 10 Earth-masses and with a null-albedo equilibrium temperatures below 2500 K<sup>2</sup>. “Accurate” here refers to mass uncertainties less than 20% and radius uncertainties less than 10%. The melting temperature of olivine is approximately 1800 K. Equilibrium temperature is calculated by

$$T_{eq} = T_* \sqrt{\frac{R_*}{2a}} (1 - A_B)^{1/4} \quad (1.1)$$

where  $T_*$  and  $R_*$  are the stellar temperature and radius,  $a$  is the semi-major axis, and  $A_B$  is the albedo which we take as 0. The null-albedo equilibrium temperature is a maximum temperature of the outer region of the planet. The bulk density

$$\rho_B = M/R^3 \quad (1.2)$$

is found from the planet’s mass,  $M$ , and radius,  $R$ , with uncertainties  $\sigma_M$  and  $\sigma_R$ . The uncertainty in density is thus given by propagation of error,

$$\sigma_{\rho_B} = \rho_B \sqrt{\left(\frac{\sigma_M}{M}\right)^2 + \left(3\frac{\sigma_R}{R}\right)^2}, \quad (1.3)$$

if the mass and radius uncertainties are assumed independent. The planets are in 72 planetary systems. Mass and radius uncertainties are treated as symmetric, and we take an average of the

---

<sup>2</sup>NASA Exoplanet Archive, <https://exoplanetarchive.ipac.caltech.edu/>, as of 10 August 2022

upper and lower standard error if unsymmetrical. Density uncertainties are a maximum of 28%.

This sample of planets show that exoplanets have bulk densities which range from dense and iron-rich (Santerne et al. 2018) to low density and volatile-rich (Léger et al. 2004). Although they are the most difficult to observe because they have the smallest radii, we see planets near the 100% core line in Fig. 1.1 and ones with various core mass fractions (cmf) between the 100% core and 100% mantle lines. Below the 100% mantle line, planets require greater volatile contents which may be in the form of a water-rich hydrosphere or below the 100% water line small planets require thick atmosphere envelopes. “Small” planets in this work thus encompasses classes of planets previously suggested like Mars-like, Earth-like, Super-Earth, mini-Neptune, sub-Neptune, water world, and super-Ganymede.

One of the most influential results in recent small exoplanet science is Fulton et al. (2017) which shows that the radii of 2025 small planets observed by *Kepler* form two distinct populations. The smaller planets are likely terrestrial-like and the larger are enriched in volatiles (e.g. Owen & Wu 2013; Rogers 2015; Ginzburg et al. 2016) with a low probability of planets having radii between 1.5 and 2 Earth-radii. The bi-modality is most commonly explained by planets forming with H/He dominated primary atmosphere envelopes which are either lost or held onto. The loss process could be dominated by photoevaporation (Lopez & Fortney 2013; Rogers et al. 2021) or core-powered mass-loss (Gupta & Schlichting 2019; 2020). Studying these two populations around various stellar types, various stellar ages, modeling their evolution, and quantifying the emptiness of the gap are active areas of study.

Investigations into these populations and identifying further categories of small exoplanets will require demographic studies of composition. However, the interior structure of a differentiated planet is degenerate with the bulk density as explored in Rogers & Seager (2010). Mass-Radius



relationships, which describe the relationship of mass and radius for a given planet composition and interior structure, are useful when probing planet populations (e.g. Sotin et al. 2007; Weiss & Marcy 2014; Neil & Rogers 2020), but are not unique when considering differentiated planets of three or more layers. We must understand planet building materials and have accurate models for planet interiors to understand the small planet population.

## 1.2 Main Components of Small Planet Interiors

The Solar System has diverse small planetary bodies with only one that supports abundant life. This diversity extends beneath the surface of the terrestrial planets. Mercury’s core makes up 70-80% of its mass (Hauck et al. 2013) compared to the 33% cmf of the Earth. Icy moons, like Ganymede, hold upwards of 45% of their mass in a water-ice hydrosphere (Kuskov & Kronrod 2005). Above the surface, Venus’s atmosphere is  $\sim 0.01\%$  of its mass making the surface pressure 90 times that of Earth. These differences in structure are tied to important aspects of habitability such as volatile abundance, cooling history, chemical cycling, and the generation of a magnetic field (Astro2020 white papers: Pontoppidan et al. 2019; Apai et al. 2019; Lazio et al. 2019; Hu et al. 2019).

We have little information on the interiors of planetary bodies as the deepest hole ever dug, Kola Superdeep Borehole, made it to a depth only 0.2% of the Earth’s radius (Kozlovsky 1982). Most of our knowledge on interiors comes from seismology which we have abundant observations of on Earth (Romanowicz 2008). *InSight* also gathered limited seismic data on the interior of Mars (Khan et al. 2021; Knapmeyer-Endrun et al. 2021; Stähler et al. 2021). Satellites, such as MESSENGER, Cassini, and Juno, gather important data on the gravitational moment of plan-

ets and moons which constrains the interior structure (Helled & Fortney 2020). BepiColumbo and a future Uranus probe will be important to better understanding Mercury and Uranus's interior structure. From meteorites, we know the primordial composition in the Solar System from calcium-aluminum rich inclusions, and we know that even small bodies differentiate into layers of distinctive density (McSween Jr & Huss 2022). Vesta in the asteroid belt is 20,000 times smaller than the Earth but it and similar bodies are the progenitor of the differentiated (achondritic) HED meteorites (McSween Jr et al. 2013). Because of our limited data, many of our assumptions on interiors is Earth-centric. In this section, I review a few important aspects of major differentiated layers.

### 1.2.1 Cores

Iron and nickel are two orders of magnitude more abundant in the Solar System than elements of higher atomic number. As major rock forming elements with high density, iron differentiates early in planetary bodies as it rains from molten mantles releasing gravitational energy as heat as it forms an iron core. The heat from core formation creates somewhere between a 500-1800 K temperature discontinuity between the hot core and mantle (Nomura et al. 2014; Lay et al. 2008). The iron and nickel alloy with estimates ranging from 5-20% nickel for the Earth (Hirose et al. 2021). The nickel content of iron meteorites is measured in Benedix et al. (2000).

Planetary cores are at extreme heat and pressure. The Earth's central pressure is over 350 GPa and temperature is over 5500 K similar to the temperature of the sun's photosphere. A planet ten times the mass of the Earth reaches 6 TPa in the center near 10 times the highest pressures reached in the laboratory. At these pressures iron takes a hexagonal close-packed (HCP) structure. The

HCP arrangement has the highest packing efficiency of sphere along with face-centered cubic at 74%.

The core of Earth is inferred to be 5-10% less dense than pure iron, also known as the “density deficiency” (Hirose et al. 2013). The core has some mix of unknown lighter elements such as silicon, oxygen, sulfur, carbon, and hydrogen. These lighter element affect the crystalline phases, physical properties, and melting temperature of the core. Mars’s core may be entirely liquid which is most likely a result of sulfur decreasing the melting temperature (Stähler et al. 2021).

### 1.2.2 Mantles

The mantle of the Earth holds diverse silicates made with lithophile elements. The upper mantle is 60% olivine,  $(\text{Mg, Fe})_2\text{SiO}_4$ , by volume. The other 40% varies by depth in proportion of garnet to pyroxene in the clinopyroxene to orthopyroxene crystalline structure. These minerals hold the aluminum and calcium in the mantle. The major orthopyroxene mineral is enstatite,  $\text{MgSiO}_3$ . At pressures above 15 GPa the olivine changes to wadsleyite with an orthorhombic structure and at above 20 GPa to ringwoodite in a spinel structure. At this pressure, in the uppermost parts of the lower mantle, the other major mineral becomes majorite (majoritic garnet,  $\text{MgSiO}_3$ ) which forms solid solutions with Al, Fe, and Ca-bearing garnets.

The upper (and upper-lower mantle) is complex, but as pressures reach 25 GPa at depths over 650 km the main mineral becomes bridgmanite,  $(\text{Mg, Fe})\text{SiO}_3$ . While periclase/magnesiowüstite is about 10% of the lower mantle by volume, bridgmanite is over 80% by volume. Hence, over 40% of the Earth’s entire mass is in bridgmanite. Deep in the Earth’s mantle above 100 GPa the bridgmanite takes another crystalline form referred to as post-perovskite. Although post-perovskite

layer is small in the Earth it influences thermal transport in the D'' layer above the core-mantle boundary, and would be a major component of mantles for larger planets. See Kaminsky (2012) for a review of these topics.

The mantles of exoplanets may have large differences in the Ca, Al, Mg, and Fe abundances changing the dominate mineralogy Unterborn et al. (2023). However, less Earth-like mantles may be possible in other systems. Carbon planets are proposed to have mantles that are composed of SiC, graphite and diamond, or even carbonates in rare situations Kuchner & Seager (2005); Seager et al. (2007); Unterborn et al. (2014). Mantles may also hold large amounts of water and other volatiles; possibly enough to change the bulk properties of the rock (Dorn & Lichtenberg 2021)

### 1.2.3 Volatile Layers

Water is the most abundant volatile in the Solar System after hydrogen and helium. Thus past the ice-line planetary bodies are formed from water rich materials and have water mass fractions over 50%. While the water storage of the mantle is an active area of research, water's low density leads it to forming a hydrosphere on the planet's surface. Earth's hydrosphere is only 0.023% of Earth's mass.

A planet with a large hydrosphere will reach pressures which forces the water to the solid phase at depths as low as 80 km (comparable to depth of Earth's lithosphere). H<sub>2</sub>O's polar nature leads to a complex phase diagram with at least 18 known phases. While hexagonal ice, Ice Ih, is the kind we experience at standard pressure and cold temperatures, at high pressure pressure water transforms to tetragonal Ice VI and cubic Ice VII. At a debated pressure between 30 and 120 GPa Ice VII transitions from a double well potential to a single well potential. This Ice X is 2 times

stiffer than Ice VII. The water phase diagram is under active investigation (see Hansen 2021). Grande et al. (2022) describes a transitional tetragonal phase Ice VII<sub>t</sub> between Ice VII and Ice X. While I do not consider this assumption in this work, little work has been done on non-pure water in exoplanet systems. Since water is a powerful solvent, a planet’s hydrosphere may have different properties from the common pure water assumption.

In this work, I focus primarily on planets with no or small secondary atmospheres. However, atmospheres are essential to understanding the entire population of planets less than 10 Earth-masses. Many concluding sections of chapters (Sec. 3.4, 4.6) discuss future work on combining interiors and atmospheres.

### 1.3 Planet Interior Solvers

Solving the interior of a planet brings together multiple disciplines from geology to high-pressure material physics to planetary science. Interior models were first used for exoplanets in Léger et al. (2004), Valencia et al. (2006), Sotin et al. (2007), and Seager et al. (2007). These models are one dimensional modelling the planet as spherically symmetric. Inside of the planet the equations of hydrostatic equilibrium must be satisfied—the pressure must be continuous and the gradient increasing inside of the planet balanced by the gravitational force acting on the planet.

With an interior structure model the pressure, density, temperature, and radius can be found as a function of enclosed mass. Boundary conditions are a radius of zero at an enclosed mass of zero and a surface temperature and pressure. Models generally assume that the planet is fully differentiated into distinct compositional shells. With a shell model, each layer can be solved with a different material. The equation of state (EoS) of each material describes the volume at pressure

and temperature conditions.

Planets are generally assumed to follow isentropic temperature gradients. This temperature gradient assumes that heat transfer occurs only through conduction, without any convective heat transfer or energy being added or removed from the system. This approximation is reasonable for large, old, slowly cooling planets. With an isentropic temperature profile, temperature changes with depth due to changes in pressure and density following the adiabat based on material properties. An isentropic temperature gradient with discontinuities at boundary layers matches the seismic data from Earth (Stacey & Davis 2008).

Underlying the many different models used for exoplanet interiors are various computational techniques (e.g. shooting Nixon & Madhusudhan (2021) or relaxation Unterborn et al. (2018)) and treatments of temperature (e.g. isothermal Seager et al. (2007) or isentropic Hakim et al. (2018)). Most importantly, these models must choose for each material an EoS. These choices often differ between studies.

In Fig. 1.2, I show the works that inform two recent interior studies. The two studies each exemplify a theme of this thesis: improving interior models and characterizing exoplanets. Dorn & Lichtenberg (2021) explores the storage of water in hot planets. Acuña et al. (2021) characterizes the interiors of the Trappist-1 planets. These two studies are built upon different legacies of interior codes with some model parameters not cited in the top-level publication. Take for example the ice phases which are based on Bezacier et al. (2014) in Acuña et al. (2021) and Wagner & Pruß (2002) in Dorn et al. (2015). Acuña et al. (2021) relies on EOS from the 1990s in both the mantle and core. In addition, both of these models are not open-source.

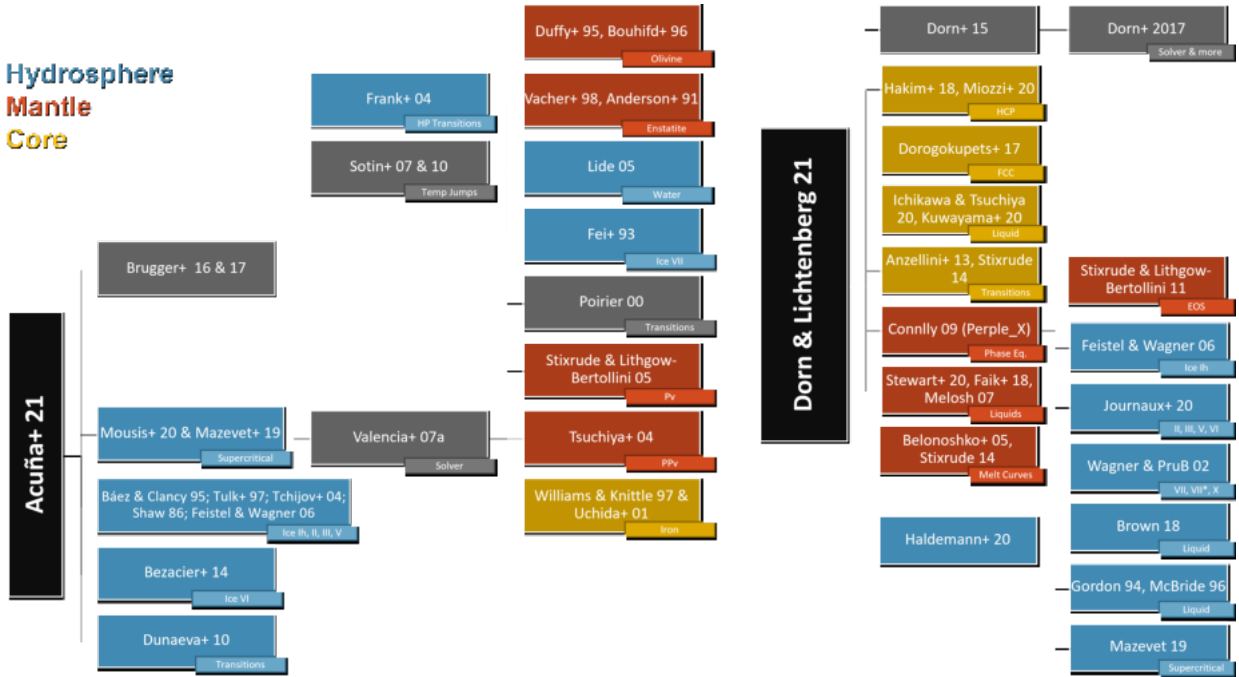


Figure 1.2: The works that inform the planet interior model in two recent planet interior works—Acuña et al. (2021) and Dorn & Lichtenberg (2021). Tree structure shows previous works the models are built upon which are not all cited in the top-level paper. Works color coded by layer they inform. Works in figure: Bruggen et al. (2016; 2017); Sotin et al. (2007); Valencia et al. (2007b); Frank et al. (2004); Duffy et al. (1995); Bouhifd et al. (1996); Vacher et al. (1998); Anderson et al. (1991); Lide (2002); Fei et al. (1993); Poirier (2000); Stixrude & Lithgow-Bertollini (2005); Tsuchiya et al. (2004); Williams & Knittle (1997); Uchida et al. (2001); Mousis et al. (2020); Mazevet et al. (2019); Báez & Clancy (1995); Tulk et al. (1997); Tchijov (2004); Shaw (1986); Feistel & Wagner (2006); Bezacier et al. (2014); Dunaeva et al. (2010); Dorn et al. (2015; 2017b); Hakim et al. (2018); Miozzi et al. (2020); Dorogokupets et al. (2017); Ichikawa & Tsuchiya (2020); Kuwayama et al. (2020); Anzellini et al. (2013); Stixrude (2014); Connolly (2009); Stewart et al. (2020); Faik et al. (2018); Melosh (2007); Belonoshko et al. (2005a); Stixrude (2014; 2012); Haldemann et al. (2020); Journaux et al. (2020); Wagner & Prub (2002); Brown (2018); Gordon & McBride (1994); McBride & Gordon (1996); Mazevet et al. (2019).

### 1.3.1 Applications to Small Planets

There are numerous works built upon interior models for small planets. Demographic-focus studies focus on the mass-radius relationship and describing compositions of planet populations. Zeng et al. (2016) develops semi-empirical mass-radius relations for two-layer rocky planets empowering quick approximations. Suissa et al. (2018) give the minimum and maximum core mass fraction an observed planet may have. Neil & Rogers (2020) develop a broken power-law relationship which match the mass-radius measurements of *Kepler* planets. They find the planets are best fit by a mixture model which considers gaseous envelope, evaporated core, and intrinsically rocky planets.

A number of studies tie other observable properties than mass and radius to planet interiors. Stellar composition may be used as a constraint on interiors. Scora et al. (2020), Schulze et al. (2021a), and Bonsor et al. (2021) explore this possibility from formation and observations and find evidence that most planet reflect their stars elemental abundances, although they may need to be devolatalized (Wang et al. 2019). Putirka & Xu (2021) investigates mantle material in white dwarf pollution finding non-Earth like mineralogy and Buchan et al. (2022) shows Ni and Cr in pollution can be used to constrain the core mass of the polluting body. As a last example, Price & Rogers (2020) constrain the cmf that an ellipsoid planet stretched by its close in orbit must have to stay intact.

Several sub-fields are building upon interior studies. Zhang & Rogers (2023) focuses on liquid layers in planets and explores the thermal evolution of planets from their formation. O'Neill & Lenardic (2007) and Meier et al. (2021) investigate planet convection. VPLANET (Barnes et al. 2020) compiles and couples a number of models related to habitability including a module for



interior thermal evolution with a focus on magnetic fields and plate tectonics. Works on planet collisions like Marcus et al. (2009; 2010) and Lock & Stewart (2017) involve using interior models to inform smoothed-particle hydrodynamics simulations. As a final example, a large body of work is concerned with coupling thick sub-Neptune atmospheres to interiors starting with Fortney et al. (2007) and including Howe & Burrows (2015) and Chen & Rogers (2016).

## 1.4 Overview

To determine if small exoplanets exhibit as diverse interior structures as the Solar System, we need robust and reproducible community standards for interior modeling. Communicating results from geology and material physics to the astronomy community and visa versa must be a priority. We must understand how model choices and uncertainty are affecting our inferences of planet composition.

In this work, I develop an open-source interior model with flexible model parameters, Chapter 2. I further its abilities to characterize observed planets, Chapter 3, and improve several aspects of our model, Chapter 4. I then turn to characterizing observed planets in a number of collaborative works, Chapter 5. This improved model and my understanding of planet characterizations culminates in a study which quantifies the uncertainties in our planet inferences for small planets from observation, model, and experimental uncertainties, Chapter 6. Throughout this work, I reiterate this introduction, give background on important concepts in exoplanets and planet interiors, and connect my work with the expansive literature on exoplanets. I summarize the work in Chapter 7.

## Chapter 2

### MAGRATHEA: an Open-Source Spherical Symmetric Planet Interior Structure Code

#### 2.1 Background

As explored in Chapter 1, the community uses a variety of models to characterize the interior structure of planets. Underlying these models are differing computational techniques (e.g. shooting in Nixon & Madhusudhan (2021), relaxation in Unterborn et al. (2018), or calculus of variation in Zeng et al. (2021)) and numerous experimental measurements and theoretical estimates of the equation of state (EoS) for planet-building materials. For example, a number of models use bridgmanite primarily in the mantle and do not include high-pressure post-perovskite (Grasset et al. 2009; Zeng et al. 2016; Brugger et al. 2017; Michel et al. 2020) while others capture detailed upper-mantle chemistry (Valencia et al. 2007b; Dorn et al. 2017b; Unterborn & Panero 2019) and recent work adds liquid silicates (Noack & Lasbleis 2020). Another point of difference is the model’s temperature profile with some using an isothermal mantle (Seager et al. 2007) rather than isentropic (Hakim et al. 2018). While others limit isothermal modeling to the water layer (Sotin et al. 2007; Brugger et al. 2016) and the atmosphere (Madhusudhan et al. 2021; Baumeister et al. 2020). Newer models try to capture the complex phase diagram of water (Mousis et al. 2020; Journaux et al. 2020; Haldemann et al. 2020), the hydration of mantle materials (Shah et al. 2021; Dorn & Lichtenberg 2021), and couple the atmosphere to the interior (Madhusudhan et al. 2020; Acuña et al. 2021).

In Huang et al. (2022), collaborators (Dr. Chenliang Huang and Dr. Jason Steffen) and I (second author) document the development of MAGRATHEA<sup>1</sup> an open-source planet interior solver that can be customized to different user-defined planet models. Compared to other codes, the package is designed to enhance ease-of-use and flexibility. MAGRATHEA features phase diagram options and transparent EoS formatting, which enables the user to choose between a large library of EoSs (equations of state) and add/change materials and equations.

We are motivated by our collaboration with high-pressure physicists to understand how uncertainties in experimental EoSs affect predictions of planet interiors. In Huang et al. (2021), also reported in Sec. 4.2, we use our adaptable planet interior model to implement new measurements for high-pressure water-ice from Grande et al. (2022). Their experiments confirmed the pressure of the transition from ice-VII to ice-X and identified a transitional tetragonal ice-VII<sub>t</sub> phase. This improved H<sub>2</sub>O equation of state changed the predicted radius of a pure water, 10 M<sub>⊕</sub> planet by over four per cent from Zeng et al. (2016).

In this chapter, we document the features and demonstrate the functionality of MAGRATHEA. The most up-to-date version is hosted on the GitHub platform. This chapter is laid out as follows. We describe the fundamentals of a planet interior solver in Section 2.2. In Section 2.3, we describe the specifics of our code and how to build a planet model within the code. A model is designated by defining a phase diagram for each layer and choosing an equations of state from our library for each phase. We discuss limitations to our default model in 2.4. We describe the code’s functionality and discuss various tests in Section 2.5. We demonstrate the EoS storage and functionality in Section 2.6 and 2.7 and end with some summarizing remarks in Section 2.8.

---

<sup>1</sup>Magrathea is the legendary planet where hyperspatial engineers manufacture custom-made planets in Douglas Adams’s *The Hitchhiker’s Guide to the Galaxy* (Adams 1995-2001).

## 2.2 Interior Structure Solver

We consider a simplified planet structure with four layers: an iron core, a silicate-dominated mantle, a hydrosphere of water/ice, and an ideal gas atmosphere. We assume these layers are spherically symmetric and that a single solution to composition at a given pressure and temperature exists within each layer. Our approach is similar to other interior structure solvers used for exoplanets (e.g. Léger et al. 2004; Valencia et al. 2006; Sotin et al. 2007; Seager et al. 2007). A schematic depiction of MAGRATHEA from input to output is shown in Fig. 2.1. Given the mass of each of these layers,  $M_{\text{comp}} = \{M_{\text{core}}, M_{\text{mantle}}, M_{\text{hydro}}, M_{\text{atm}}\}$ , the code calculates the radius returning the pressure  $P(m)$ , density  $\rho(m)$ , and temperature  $T(m)$  with enclosed mass  $m$  by solving the following four equations:

### 1. Mass continuity equation

$$\frac{dr(m)}{dm} = \frac{1}{4\pi r^2 \rho(m)}, \quad (2.1)$$

### 2. Hydrostatic equilibrium

$$\frac{dP(m)}{dm} = -\frac{Gm}{4\pi r^4}, \quad (2.2)$$

### 3. Temperature gradient

If the isothermal option is chosen, the temperature gradient is 0. When the isentropic option is chosen, depending on the available thermal properties of the phases, the temperature gradient can be calculated using either of the following two formulae. If the Grüneisen parameter

$\gamma$  is available, we can have

$$\begin{aligned}\frac{dT(m)}{dm} &= \frac{dT}{dV}\bigg|_S \frac{dV}{d\rho} \frac{d\rho}{dm} \\ &= -\frac{m_{\text{mol}}}{\rho^2} \frac{dT}{dV}\bigg|_S \left( \frac{\partial \rho}{\partial P} \frac{dP}{dm} + \frac{\partial \rho}{\partial T} \frac{dT}{dm} \right).\end{aligned}$$

Thus,

$$\frac{dT(m)}{dm} = \frac{\frac{dT}{dV}\big|_S \frac{Gm}{4\pi r^4}}{\frac{\rho^2}{m_{\text{mol}}} \frac{\partial P}{\partial \rho}\bigg|_T - \frac{dT}{dV}\bigg|_S \frac{\partial P}{\partial T}\bigg|_\rho}, \quad (2.3)$$

where

$$\frac{dT}{dV}\bigg|_S = -\frac{\gamma T}{V}, \quad (2.4)$$

$m_{\text{mol}}$  and  $V$  are the molar mass and volume respectively.

Alternatively, if the thermal expansion  $\alpha$  is available, we can have

$$\frac{dT(m)}{dm} = -\frac{\alpha T G m}{4\pi r^4 \rho c_p}, \quad (2.5)$$

where  $c_p$  is the specific heat capacity at constant pressure.

#### 4. Equation of state (EoS)

$$P(m) = P(\rho(m), T(m)), \quad (2.6)$$

which is unique for each material/phase.

The boundary conditions of the model are  $r = 0$  at  $m = 0$  and the user-defined surface temperature and pressure,  $T(M_p)$  and  $P(M_p)$ . The default surface pressure is 100 mbar approximately the pressure level of the broad-band optical transit radius probes (Grimm et al. 2018). Since a rapid

temperature jump may occur at the boundary between chemically distinct layers, where heat can only transfer conductively (Valencia et al. 2006), the user can also set a temperature discontinuity,  $T_{\text{gap}}$ , at the boundary of adjacent layers. The Earth is often modeled with a discontinuity ranging from a 300 to 1100 K increase across the core mantle boundary (Nomura et al. 2014; Lay et al. 2008) and (Valencia et al. 2007b) and (Sotin et al. 2007) use discontinuities in their exoplanet models. In our demonstrations in Section 2.5, we use planets that are in thermal equilibrium between their layers with  $T_{\text{gap}} = \{0, 0, 0, T(M_p)\}$ .

The user can choose between isothermal and isentropic temperature mode by adjusting an *isothermal* flag of the integrator. When the flag is set to true, the whole planet is assumed to be isothermal (except the atmosphere layer, see section 2.3.8). When the input EoS parameters of a phase are not sufficient to calculate the isentropic temperature gradient (see section 2.2.2), this specific phase would be treated as isothermal, regardless of the value of the *isothermal* flag.

### 2.2.1 Phase Diagrams

We model our planets with distinct differentiated layers with defined mass fractions. However, within each layer the phase may change due to the large pressure and temperature ranges. When integrating within a layer, the code first checks the pressure and temperature to determine the appropriate region of the phase diagram. A built-in phase function outputs a link to the EoS of the material or phase in the region. The density  $\rho$  or the volume of unit cell  $V$  can then be solved from the EoS (Eq. 2.6).

A key feature of MAGRATHEA is the user’s ability to change the phase diagram in each layer and choose between EoSs for each phase. Fig. 2.2 shows our default phase diagram and Sec. 2.3.3

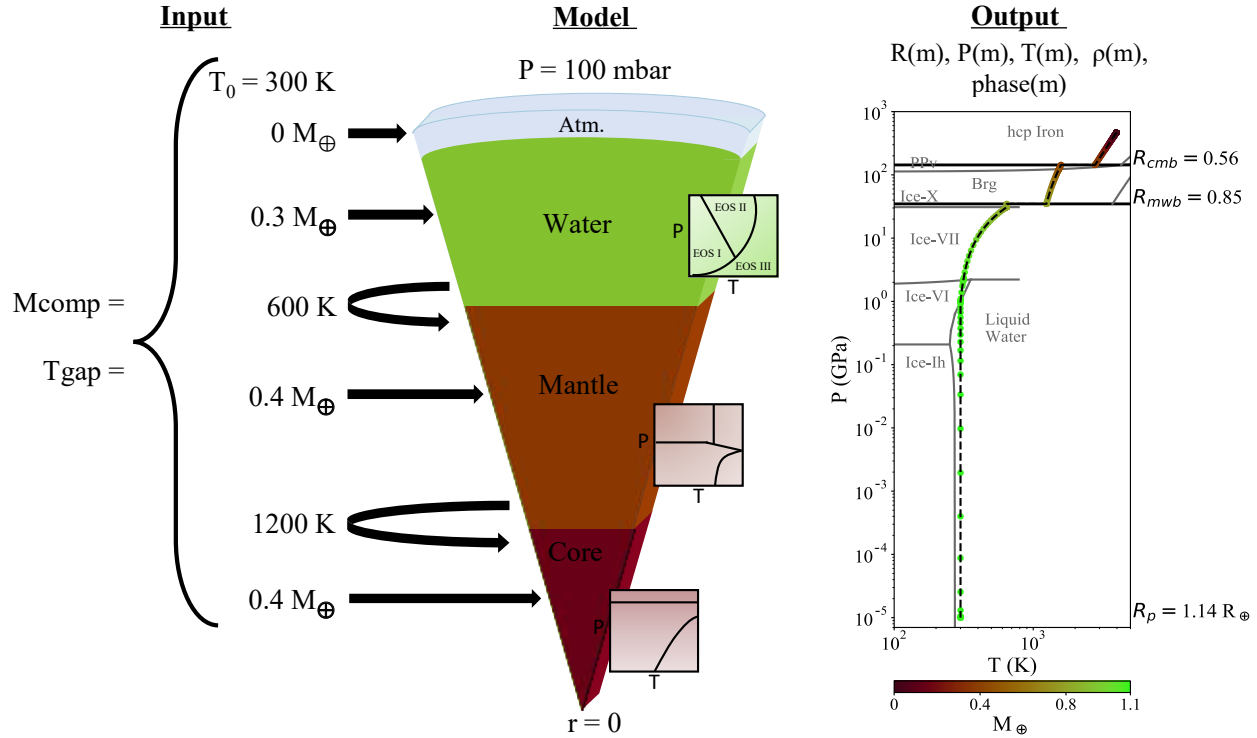


Figure 2.1: A schematic overview of MAGRATHEA. Showing an example input, *left*, of a  $1.1 M_{\oplus}$  planet with  $0.4 M_{\oplus}$  core,  $0.4 M_{\oplus}$  mantle, and  $0.3 M_{\oplus}$  hydrosphere. The planet is not in thermal equilibrium with a surface temperature of 300 K and jumps in temperature across boundary layers of 600 K and 1200 K. *Center*, shows MAGRATHEA's four input layers with cartoons of phase diagrams defined for each layer with an EoS chosen for each phase. Default phase diagrams shown in Fig. 2.2. *Right*, shows the pressure and temperature with enclosed mass. The radius at boundaries and the planet radii is also shown.

further details their implementation. The atmosphere layer is not shown in the plots and has two “phases”, isothermal for  $P < 100$  bar and adiabatic for  $P > 100$  bar.

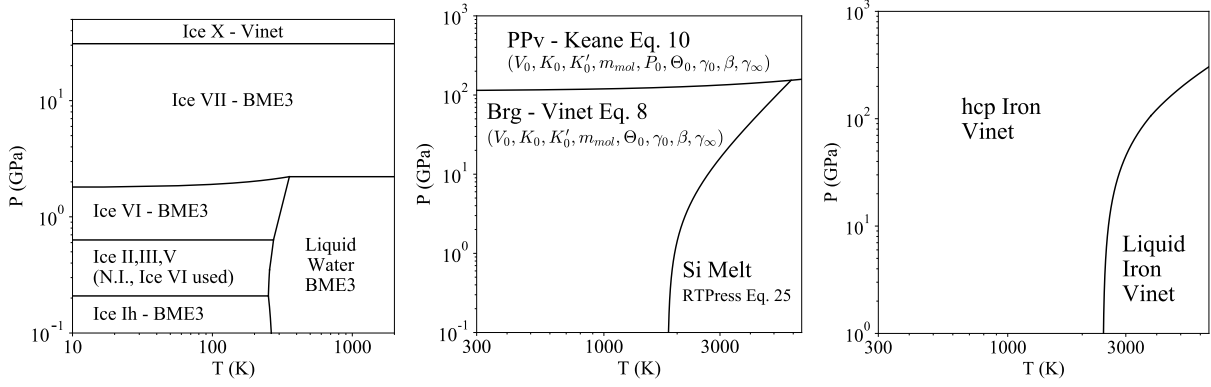


Figure 2.2: Default phase diagrams for hydrosphere, mantle, and core layers. EoS and phase transitions from a variety of sources detailed in Sec. 2.3.4. Type of EoS fitting equation shown from Sec. 2.2.2. Additionally, the parameters for mantle EoSs are shown, *middle*. The phase diagrams and choice of EoS can be customized by the user. *N.I.* is *not implemented*. The atmosphere layer also has a phase function, but our default is ideal gas at all pressure and temperatures, see Sec. 2.3.8

## 2.2.2 Equation of State Formulae

The density of a phase at certain temperature and pressure is determined by the EoS, which can be fed into MAGRATHEA either through an analytical fitting formula or a tabulated pressure-density table. For the first option, each material’s EoS must provide the parameters for one of the following formulations.

According to the Mie-Grüneisen-Debye (MGD) formulation, the total pressure  $P$  can be divided into an isothermal term  $P_c$ , and a thermal term,  $P_{th}$ , expressed as (Dewaele et al. 2006):

$$P(V, T) = P_c(V) + P_{th}(V, T) - P_{th}(V, T_0) \quad (2.7)$$



MAGRATHEA includes four common types of the EoS that give the reference isotherm  $P_c$ , including:

1. The Eulerian finite strain Birch-Murnaghan EoS (BME) is the most commonly used EoS.

The fourth-order BME (Seager et al. 2007) is

$$P_c = \frac{3}{2}K_0 (\eta^{7/3} - \eta^{5/3}) \quad (2.8)$$

$$(1 + \zeta_1(1 - \eta^{2/3}) + \zeta_2(1 - \eta^{2/3})^2),$$

where

$$\eta = V_0/V, \zeta_1 = \frac{3}{4}(4 - K'_0)$$

$$\zeta_2 = \frac{3}{8} \left( K_0 K''_0 + K'_0(K'_0 - 7) + \frac{143}{9} \right).$$

$K = -V(\partial P/\partial V)_T$  is the isothermal bulk modulus,  $K'$  is the first derivative of the bulk modulus with respect to pressure, and  $K''$  is the second of the bulk modulus with respect to pressure. The subscript 0 refers to quantities at ambient-pressure conditions. If  $\zeta_2$  is set to zero the EoS reduces to third-order BME.

2. Vinet EoS (Seager et al. 2007; Smith et al. 2018; Wicks et al. 2018), which is considered to give more accurate result than BME at high pressure or large compression (Poirier 2000)

$$P_c = 3K_0\eta^{2/3} (1 - \eta^{-1/3}) \quad (2.9)$$

$$\exp \left( \frac{3}{2}(K'_0 - 1) (1 - \eta^{-1/3}) \right);$$

### 3. Holzapfel EoS (Bouchet et al. 2013)

$$\begin{aligned}
 x &= (V/V_0)^{1/3} \\
 c_0 &= -\ln \left( \frac{3K_0}{1003.6 \text{ GPa cm}^5 \text{ mol}^{-5/3} (Z/V_0)^{5/3}} \right) \\
 c_2 &= \frac{3}{2}(K'_0 - 3) - c_0 \\
 P_c &= 3K_0 x^{-5} (1 - x) \\
 &\quad \exp(c_0(1 - x)) (1 + c_2 x(1 - x));
 \end{aligned} \tag{2.10}$$

### 4. Keane EoS (Sakai et al. 2016)

$$\begin{aligned}
 y &= V_0/V \\
 K'_\infty &= 2 \left( \gamma_\infty + \frac{1}{6} \right) \\
 P_c &= \frac{K'_0 K_0}{K_\infty'^2} \left( y^{K'_\infty} - 1 \right) - (K'_0 - K'_\infty) \frac{K_0}{K'_\infty} \ln(y)
 \end{aligned} \tag{2.11}$$

5. An empty placeholder is available for an additional formulation of the EoS such as from Choukroun & Grasset (2007).

For phases that only exist at high pressure, the bulk modulus,  $K_P$ , can be measured more precisely at the phase transition pressure,  $P_0$ , than at ambient pressure (Salamat et al. 2013). If  $K_P$  is applied instead of  $K_0$ , a constant pressure  $P_0$  under which the bulk modulus is measured is added to the isotherm pressure. If the parameters to calculate the thermal term,  $P_{th}$ , are not provided, only  $P_c$  is calculated and a constant temperature is returned.

$P_{th}$  is most commonly calculated from a quasi-harmonic Debye thermal pressure and the an-

harmonic and electronic thermal pressure, which are obtained from (Belonoshko et al. 2008; Duffy et al. 2015)

$$P_{th}(T) = \frac{\gamma}{V} E_{th}(T) + \frac{3nR}{2V} e_0 x^g g T^2, \quad (2.12)$$

where

$$x = V/V_0 = \eta^3, \gamma = \gamma_\infty + (\gamma_0 - \gamma_\infty) x^\beta \quad (2.13)$$

$$\Theta = \Theta_0 x^{-\gamma_\infty} \exp\left(\frac{\gamma_0 - \gamma_\infty}{\beta} (1 - x^\beta)\right) \quad (2.14)$$

$$z = \Theta/T, E_{th} = 3nRT D_3(z). \quad (2.15)$$

$D_3$  indicates a third-order Debye function.  $\Theta_0$ ,  $\gamma_\infty$ ,  $\gamma_0$ ,  $\beta$ ,  $e_0$ , and  $g$  are fitting parameters,  $R$  is the gas constant, and  $n$  is the number of atoms in the chemical formula of the compound. A numerical derivative of Eq. 2.7 gives the  $\frac{\partial P}{\partial \rho}\bigg|_T$  and  $\frac{\partial P}{\partial T}\bigg|_\rho$  that are required in the Eq. 2.3.

A different framework for the thermal term, referred to as RTpress in the following, is used in Wolf & Bower (2018) and built upon the Rosenfeld-Trazona model. In addition to the Grüneisen parameters, it has additional fitting terms with derivation in Wolf & Bower (2018).

In RTpress, the Grüneisen parameter can be written as

$$\gamma = \gamma_{0S} \frac{C_V(V, T_{0S})}{C_V(V, T)} + V \frac{b'(V)}{b(V)} \frac{\Delta S^{\text{pot}}(T_{0S} \rightarrow T)}{C_V(V, T)}. \quad (2.16)$$

The subscript 0S stands for the quantity evaluated along the reference adiabat,

$$T = T_{0S} = T_0 \sqrt{1 + a_1 f + \frac{1}{2} a_2 f^2}, \quad (2.17)$$

with,

$$f \equiv f(V) = \frac{1}{2} \left[ \left( \frac{V_0}{V} \right)^{\frac{2}{3}} - 1 \right], \quad (2.18)$$

$$a_1 = 6\gamma_0, \quad \text{and} \quad a_2 = -12\gamma_0 + 36\gamma_0^2 - 18\gamma_0', \quad (2.19)$$

where  $\gamma_0$  is the Grüneisen parameter at zero GPa and  $\gamma_0' = V_0(d\gamma/dV)_0$ .

The Grüneisen parameter variation along the reference adiabat is

$$\gamma_{0S} = \frac{(2f + 1)(a_1 + a_2 f)}{6(1 + a_1 f + \frac{1}{2}a_2 f^2)}. \quad (2.20)$$

$$b(V) = \sum_n b_n \left( \frac{V}{V_0} - 1 \right)^n, \quad (2.21)$$

and

$$b'(V) = \sum_n b_n \left( \frac{n}{V_0} \right) \left( \frac{V}{V_0} - 1 \right)^{n-1} \quad (2.22)$$

are a polynomial representation of the thermal coefficients and its volume derivative in cgs units.

The total heat capacity

$$C_V(V, T) = b(V)f_T^{(1)} + \frac{3}{2}nR \quad (2.23)$$

is the sum of potential and kinetic contributions<sup>2</sup>, where

$$f_T = \left( \frac{T}{T_0} \right)^\beta - 1, \quad f_T^{(1)} = \frac{\beta}{T_0} \left( \frac{T}{T_0} \right)^{\beta-1}. \quad (2.24)$$

---

<sup>2</sup>We believe that Eq. B.3 in Wolf & Bower (2018) should read  $C_V^{\text{kin}} = \frac{3}{2}k_B$ . To be consistent with the unit eV/atom chosen for  $b_n$  in their work, the number of atoms per formula unit should not be a factor.

The difference in entropy from the reference adiabat from the potential contribution is

$$\Delta S^{\text{pot}}(T_{0S} \rightarrow T) = \frac{b(V)}{\beta - 1} \left( f_T^{(1)}(T) - f_T^{(1)}(T_{0S}) \right). \quad (2.25)$$

Finally, the thermal term of the pressure in the framework of Wolf & Bower (2018) can be written as

$$\begin{aligned} P_{th} = & -b'(V)f_T + \gamma_{0S}(V) \frac{C_{V,0S}(V) \cdot (T - T_0)}{V} \\ & + \frac{b'(V)}{\beta - 1} \left[ T \left( f_T^{(1)} - f_T^{(1)}(T_{0S}) \right) \right. \\ & \left. - T_0 \left( f_T^{(1)}(T_0) - f_T^{(1)}(T_{0S}) \right) \right] \end{aligned} \quad (2.26)$$

Besides the MGD representation, the P-V-T equation of state can also be expressed as (Fei et al. 1993)

$$V(P, T) = V(P, T_0) \exp \left[ \int_{T_0}^T \alpha(P, T') dT' \right], \quad (2.27)$$

$\alpha(P, T)$  is the thermal expansion, which has the form of

$$\alpha(P, T) = \alpha(T) \left( 1 + \frac{K'_0}{K_0} P \right)^{-\xi}. \quad (2.28)$$

$\alpha(T)$  is the zero-pressure thermal expansion coefficient. For  $T > T_0$ , it is expressed as a linear function of temperature

$$\alpha(T) = \alpha_0 + \alpha_1 T. \quad (2.29)$$

For phases that adopt the thermal expansion representation, the Eq. 2.5 can be used to calculate

adiabatic temperature gradient. The heat capacity in the equation can be calculated using the fitting formula

$$c_p = c_{p0} + c_{p1}T - c_{p2}T^{-2}. \quad (2.30)$$

### 2.2.3 Tabulated Equation of State

In place of a fitting equation, the EoS can take the form of a tabulated density-pressure table which then code then interpolates. For `MAGRATHEA` the input file should have two columns, the first column is the density in  $\text{g cm}^{-3}$  and the second column is the pressure in GPa. The pressure must be strictly ordered. The first row of the table file, which contains header information, is skipped when the file is parsed. The program interpolates the table monotonically using the Steffen spline (Steffen 1990; no relation to our co-author) from the *gsl* package (Galassi et al. 2009).

### 2.2.4 User-Defined Function

For further flexibility, users can create or modify the EoS of a phase using their own C++ functions. `MAGRATHEA` supports three types of user-defined functions. First, a user can provide an EoS function that returns the material density as a function of pressure and temperature. In addition, either a temperature gradient,  $dT/dP$ , as a function of pressure and temperature or an entropy function dependent on density and temperature can be used to set up the temperature solver in a phase. If a user-defined temperature gradient function is set up, the temperature profile of this phase is not restricted to isentropic. The density function and the temperature function ( $dT/dP$  or entropy) can also be used in combination for a phase. The method to import these user-defined functions is shown in Appendix 2.7.

## 2.3 Overview of the Code Structure

MAGRATHEA is written in C++ and relies on the *GNU Scientific Library (GSL)*<sup>3</sup> (Galassi et al. 2009). A step by step guide to run the code can be found in the *README* file on our GitHub repository.

The code is compiled with the included *Makefile*. The central interaction with the user occurs through *main.cpp*. The user may choose between seven modes by setting *input\_mode*. They include the regular solver, a temperature-free solver, a two-layer solver (Sec. 2.3.2), three methods to change the EoS during run-time (Sec. 2.5.3), and a bulk input mode for solving many planets with the regular solver in a single run (Sec. 2.5.4). Each mode requires the user to define the mass of each layer in the planet. In modes where the regular solver is used, the user defines a temperature array which gives the temperature at the surface and any discontinuities between layers. This section covers the specific design of the code and options that the user may choose between—the solver in Sect. 2.3.1, the phase diagram in 2.3.3, and the EoSs in Sec. 2.3.4.

### 2.3.1 Solver

Solving the ordinary differential equations (ODE), Eq. 2.1-2.4, is a two-point boundary value problem (Press et al. 2007). We have a total of three differential equations for  $r$ ,  $P$ , and  $T$  verses the independent variable  $m$ .  $P$  and  $T$  need to satisfy boundary condition at  $m = M_p$ , and the boundary condition for  $r$  is located at  $m = 0$ . The density may be discontinuous at a phase boundary whose location is unknown. Therefore, in our case, MAGRATHEA solves this problem with the method of shooting to a fitting point which is preferred to a relaxation method because it does not require

---

<sup>3</sup>*GNU Scientific Library* can be found at <http://www.gnu.org/software/gsl/>

predefined grids.

MAGRATHEA integrates ODEs using GSL’s *gsl\_odeiv2* (Galassi et al. 2009) with a Runge-Kutta-Fehlberg method, which is a fourth order integrator with a fifth order error estimator and an automated adaptive step-size. To have a better estimation on the boundary conditions,  $P(m = 0)$ ,  $T(m = 0)$ , and  $R_p$ , we conduct an extra round of iteration using a “pure” shooting method. In this first iteration, the ODEs are integrated from an estimated planet radius  $R_p$  at  $M_p$  outside-in toward the center until  $m = 0$  or  $P(m) > 10^5$  GPa. The  $R_p$ , which is the only unset boundary condition at  $M_p$ , is iterated using Brent-Dekker root bracketing method. The initial estimated radius is calculated based on a crude density assumption for each layer (15, 5, 2, and  $10^{-3}$  for iron, mantle, ice, and atmosphere respectively in the unit of  $\text{g cm}^{-3}$ ).

Predetermined by the user, the values of the enclosed mass at each layer interface are set as the bounds of the ODE integrator. In contrast, the enclosed mass where the phase changes within a layer is determined by the phase diagram in  $P$ - $T$  space. Thus, the step of the ODE integral typically does not land exactly on the location of the phase change. To avoid introducing extra inaccuracy, when the ODE integration reaches a different phase the integrator is restored to the previous step and the integration step is cut into half. The integrator can only move forward to the new phase when the step size that crosses the phase boundary is less than the ODE integrator accuracy tolerance multiplied by  $M_p$ .

Using the estimated boundary condition, we conduct the shooting to a fitting point method, which start ODE integration from both  $m = 0$  and  $m = M_p$  toward a fitting point with mass  $m_{fit} = 0.2M_p$ . The code will automatically adjusted  $m_{fit}$  if it occurs at a layer’s boundary. The code uses GSL’s *gsl\_multiroot\_fsolver\_hybrids* to adjust  $P(0)$ ,  $T(0)$ , and  $R_p$ , until  $P$ ,  $T$ , and  $r$  at  $m_{fit}$  obtained integrating from the inner branch and from the outer branch agrees within a



Table 2.1: List of status information of the planet profile object

Value	Meaning
0	Normal.
1	The result includes phase(s) that is(are) not formally implemented in MAGRATHEA.
2	The two shooting branches do not match within the required accuracy at the fitting point.
3	Under two-layer mode, the error of planet surface pressure is larger than the required accuracy.

relative error  $< 10^{-4}$ . The ODE integrator tolerance will be reduced (made more strict) by a factor of three if the multidimensional root-finder can not find a solution within 15 tries. After the ODE integrator tolerance is reduced four times (three additional times, each by the stated factor of three), if the solver still cannot find a solution that satisfies the required joint accuracy at the fitting point, the code will output an error message as well as the best result it can find.

The solver returns a planet interior profile object after completion, which includes the  $r$ ,  $P$ ,  $T$ ,  $m$ ,  $\rho$ , and the component phase at each grid step. A *print* function is available to save the profile into an ASCII table. The function *getRs* returns the list of radii of the outer boundary of each component. Users can use *getstatus* to access the status information of the returned object which indicates whether precautions should be taken regarding the iteration result. A list of potential problems and their assigned return value is summarized in Table 2.1.

### 2.3.2 Simplified Two Layer Mode

In addition to the regular solver, we include a mode for a simplified two layer solver. We use this for quick calculations of water/mantle and mantle/core planets in Huang et al. (2021). We recommend using our complete solver in most instances, but this method can be used for quicker

and cheaper calculations; one such use is demonstrated in Sec. 2.5.3.

Two-layer mode can only calculate the structure of 300 K isothermal planets and does not support an atmosphere. Without the temperature differential equation, the program only solves the radius and pressure differential equations, with the radius boundary condition at the center, and the pressure boundary condition at the surface. This simpler problem is solved using the "pure" shooting method inside-out, starting from the equations' singular point at the planet center. The solver iterates the center pressure using the Brent-Dekker root bracket method until either the center pressure reaches the set accuracy target, or the surface pressure  $P(M_p)$  is within 2% of the user specified value. If the iteration ends because the first criteria is satisfied first, an abnormal status value 3 will be returned by *getstatus*. To avoid this, users may adjust the ODE integration tolerance and center pressure accuracy target accordingly based on the specific problem.

With this solver, the two-layer input modes provide an interface to calculate mass-radius curves for hypothetical planets that are composed of only two components with fixed mass ratio (e.g. figure 3 in Huang et al. (2021)).

### 2.3.3 Phase Diagram Implementation

Phase diagrams are defined in *phase.cpp*. The file contains four functions corresponding to the four layers: *find\_Fe\_phase*, *find\_Si\_phase*, *find\_water\_phase*, and *find\_gas\_phase*. The *if* statement is used within each function to create the region of P-T space to which an EoS applies. The return value of each *if* statement should be the name of the pointer corresponding to the EoS for the given phase (further described in Appendix 2.6).

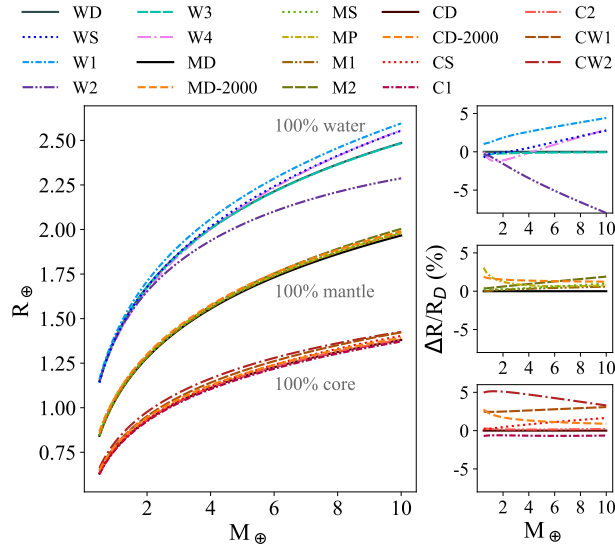
Transitions can be defined as pressure or temperature conditionals. Our default phase diagrams

are shown in Fig. 2.2. We use phase transitions which are linear with pressure/temperature within the conditionals for the transfer between solid and liquid iron (Dorogokupets et al. 2017) and between bridgmanite and post-perovskite (Ono & Oganov 2005). Parameterized phase transition curves can also be defined as separate functions in *phase.cpp* and called within the “find phase” functions. We define the function *dunaeva\_phase\_curve* to implement the fitting curve with five coefficients,  $T(P) = a + bP + c \ln P + d/P + e\sqrt{P}$ , from Dunaeva et al. (2010) for the transitions between phases of water.

#### 2.3.4 Built-In Equations of State

We have over 30 EoSs available in MAGRATHEA which can be called within the phase diagrams. These include EoS functions for various planet building materials, and different parameter estimates for the same material from various works. We discuss the equations currently available for each layer in the following four subsections. New EoSs can be added to *EOSlist.cpp* by following the storage structure described in Appendix 2.6. In Fig. 2.3 we show mass-radius relationships up to ten Earth-masses for planets of one layer with a large selection of our implemented equations. The index of equations in Fig. 2.3 is also noted in the text in brackets.

In addition to the equations listed below, the program includes tabulated EoS of iron, silicate, and water from Seager et al. (2007) [CS, MS, WS], who combined empirical fits to experimental data at low pressure and Thomas-Fermi-Dirac theory at high pressure.



Index	Description	Source
*D	Default EoSs	Multiple
*S	Tabulated	Seager et al. (2007)
*-2000	2000 K surface	Multiple
WD	Ice VI & VII	Bezacier et al. (2014)
	Ice X	Grande et al. (2022)
W1	Ice VII	Frank et al. (2004)
	Ice X	French et al. (2009)
W2	Ice VII	Frank et al. (2004)
W3	Ice VII, VII', X	Grande et al. (2022)
W4	Ice VI & VII	Bezacier et al. (2014)
	Ice X	Hermann & Schwerdtfeger (2011)
MD	Brg	Oganov & Ono (2004)
	PPv	Sakai et al. (2016)
MP	PREM	Zeng et al. (2016)
M1	Brg/PPv	Oganov & Ono (2004)
M2	Brg	Shim & Duffy (2000)
CD	Fe HCP	Smith et al. (2018)
C1	Fe HCP	Bouchet et al. (2013)
C2	Fe HCP	Dorogokupets et al. (2017)
CW1	Fe-7wt%Si	Wicks et al. (2018)
CW2	Fe-15wt%Si	Wicks et al. (2018)

Figure 2.3: *Top*, mass-radius relationship for planets with 100 per cent of mass in either the core, mantle, or hydrosphere demonstrating many of the EoSs implemented in MAGRATHEA. *Bottom*, percent difference in final planet radii compared to our selected “default” EoSs for water (*top*), mantle (*middle*), and core (*bottom*). Table lists the major components of each model with 300 K surface temperature unless designated with a “-2000”. Near the surface, water planets have water and Ice VI, and hot mantle planets have silicate melt.

### 2.3.5 Core/Iron

At the extreme pressures of a planetary core, iron is stable in a hexagonal close-packed (HCP) phase. The program includes HCP iron EoSs from Bouchet et al. (2013) [C1], Dorogokupets et al. (2017) [C2], and Smith et al. (2018) [CD] (see Fig. 2.3). We choose as our default equation the Vinet fit (Eq. 2.9) from Smith et al. (2018) measured by ram compressing iron to 1.4 TPa. We determine the fitting parameters of the Grüneisen by fitting Eq. 2.13 to Fig. 3b in Smith et al. (2018) through maximum likelihood estimation. The default core layer includes a liquid iron EoS and melting curve from Dorogokupets et al. (2017) who compressed iron to 250 GPa and 6000 K.

Iron-silicate alloy EoSs are implemented as well. Wicks et al. (2018) experimentally determined the EoS for Fe-Si alloys with 7 wt per cent Si [CW1] and 15 wt per cent Si [CW2]. These alloy equations are useful in reproducing the density of the Earth’s core which contains an unknown mixture of light elements (Hirose et al. 2013). An additional liquid iron equation is included from Anderson & Ahrens (1994).

At lower temperatures and pressures, fcc (face-centered cubic) iron is not currently implemented. The EoS of fcc iron has similar parameters to that of hcp iron ( $K_{0,fcc} = 146.2$ ,  $K_{0,hcp} = 148.0$ ). The fcc-hcp-liquid triple point is at 106.5 GPa and 3787 K (Dorogokupets et al. 2017).

### 2.3.6 Mantle/Silicate

The main mineral constituent of the Earth’s mantle is bridgmanite (Brg), referred to in the literature cited here as silicate perovskite, which at high pressure transitions to a post-perovskite (PPv) phase (Tschauner et al. 2014). MAGRATHEA includes third-order BME (Eq. 2.8) Brg from Shim & Duffy (2000) [M2] and Vinet EoSs (Eq. 2.9) for Brg and PPv measured with *ab initio*

simulations and confirmed with high pressure experiments from Oganov & Ono (2004) and Ono & Oganov (2005) [M1].

Our default mantle [MD] includes Brg from Oganov & Ono (2004) and an updated PPv thermal EoS from Sakai et al. (2016). Sakai et al. (2016) compressed PPv to 265 GPa with a laser-heated diamond anvil cell and extended the EoS using a Keane fit (Eq. 2.11) to 1200 GPa and 5000 K with *ab initio* calculations. At high temperatures ( $>1950$  K at 1.0 GPa), we use a liquid  $\text{MgSiO}_3$  with RTPress EoS from Wolf & Bower (2018) with melting curve from Belonoshko et al. (2005b). The silicate melt transfers directly to PPv when  $P > 154$  GPa and  $T > 5880$  K since the behavior in this regime is unknown. An alternate silicate melt is implemented from Mosenfelder et al. (2009).

Our default mantle is thus pure  $\text{MgSiO}_3$  in high-pressure phases which is more  $\text{SiO}_2$  rich than the Earth. At low pressure ( $\lesssim 25$  GPa), materials such as olivine, wadsleyite, and ringwoodite are the main constituents (Sotin et al. 2007). Although we don't include these minerals and more complex mantle chemistry at this time, we include a tabulated EoS for the mantle using the mantle properties in the Preliminary Reference Earth Model (PREM) (Stacey & Davis 2008; Appendix F) [MP]. We also have not explored additional measurements of transition curves between compositions/phases.

### 2.3.7 Hydrosphere/Water

Similar to the icy moons in the Solar System; exoplanets with low density are theorized to have a large fraction of mass in a hydrosphere composed of primarily high-pressure water-ice. Laboratory measurements of the thermal properties of ice at high pressures are difficult to obtain and sometimes inconsistent (Thomas & Madhusudhan 2016; Myint et al. 2017). Due to the complex-

ity of the phase diagram of water and large uncertainties in current measurements, in the current version of MAGRATHEA, we use a simplified hydrosphere phase diagram.

At pressures below 2.216 GPa, we applied liquid water (Valencia et al. 2007b) if the temperature is above the melting curve (Dunaeva et al. 2010). Below the melting curve, we have Ice Ih (Feistel & Wagner 2006; Acuña et al. 2021) at pressures below 0.208 GPa and Ice VI (Bezacier et al. 2014) (described below) at pressures above 0.632 GPa. Ice II, III, and V, which exist at pressures in between, are currently not built-in since this layer is thin and has negligible impact on the planet. If a planet passes through these phases, the Ice VI EoS is used and the user is notified that they passed through this region. For water and Ice Ih the isothermal temperature is applied regardless the value of the *isothermal* flag.

At high pressure, our default hydrosphere layer uses Ice VII with thermal expansion (Bezacier et al. 2014). Instead of using the MGD representation, most high pressure ice studies express their result with thermal expansivity, with the exception of Fei et al. (1993) which present their result with both methods. Although the isobaric specific heat capacity  $c_p$  is necessary to determine the temperature gradient using the thermal expansivity representation (see Eq. 2.5), it is not reported in most studies. Similar to Zeng et al. (2021), we include a formulation using the thermal expansion representation for Ice VI and VII from Bezacier et al. (2014) with estimated  $c_p$  of 2.6 and  $2.3 \text{ J g}^{-1} \text{ K}^{-1}$  based on Tchijov (2004).

At this time, we do not include a phase boundary or EoS for supercritical water. To avoid extrapolating the Ice VII EoS to high temperature that may lead to non-physical density, an artificial melting curve at constant temperature 1200 K is drawn in between 2.216 GPa and 30.9 GPa. The water EoS (Valencia et al. 2007b) is used as an approximation in supercritical regions and the user is notified. Lastly, the default hydrosphere transitions at 30.9 GPa to a Vinet EoS for Ice X from

Grande et al. (2022) which is calculated at 300 K and returns a constant temperature throughout regardless the value of the *isothermal* flag.

The following high-pressure water-ice EoSs are also available as alternative. Third-order BME Ice VII EoS with thermal expansion and heat capacity from Frank et al. (2004) and 3rd order BME Ice VII EoS using MGD expression from Sotin et al. (2007). Other ice EoSs that implemented do not support the isentropic temperature gradient. They include Ice VII EoS along the melting curve (Frank et al. 2004) and tabulated Ice X (French et al. 2009) which combined were used in the planetary models of Zeng et al. (2016) [W1]. Our library has three fits to the 300 K Ice VII measurements from Frank et al. (2004) – their original 3rd order BME, their BME parameters in a Vinet equation [W2], and a Vinet fit to their results. We have the three phases of ice including the transitional Ice VII' from Grande et al. (2022) which was used in Huang et al. (2021) [W3]. Lastly, we have a 3rd order BME Ice X from Hermann & Schwerdtfeger (2011) [W4]. A future version of MAGRATHEA will expand upon these options with results from French & Redmer (2015), Journaux et al. (2020), and other water phases from the AQUA collection (Haldemann et al. 2020).

### 2.3.8 Atmosphere/Gas

The ideal gas equation of state:

$$P = \frac{\rho RT}{m_{mol}}, \quad (2.31)$$

and temperature relation:

$$T \propto P^{(\gamma_{gas}-1)/\gamma_{gas}} \quad (2.32)$$



is applied to the gas layer at all pressures and temperatures, where  $\gamma_{\text{gas}}$  is the adiabatic index of the gas. Combining Eq. 2.1, 2.2, 2.31, and 2.32, we have the ideal gas temperature gradient

$$\frac{dT(m)}{dm} = -\frac{(\gamma_{\text{gas}} - 1)m_{\text{mol}}Gm}{4\pi r^4\gamma_{\text{gas}}R\rho}. \quad (2.33)$$

The temperature profile can be chosen between isothermal and isentropic by setting the number of atoms per molecule  $n$  (see Table 2.5), which further determines  $\gamma_{\text{gas}}$ . The adiabatic index  $\gamma_{\text{gas}}$  can be chosen from  $\gamma_{\text{gas}} = \frac{5}{3}$  for monatomic gas,  $\gamma_{\text{gas}} = \frac{7}{5}$  for diatomic gas, and  $\gamma_{\text{gas}} = \frac{4}{3}$  for polyatomic gas. An isothermal gas EoS can be achieved by setting its  $n = 0$ . The temperature profile of the gas layer is determined by the properties of the gas EoS and will not be overwritten by the *isothermal* flag.

Nixon & Madhusudhan (2021) shows that self-consistently modelled atmosphere temperature profiles can be closely matched by a radiative profile above a radiative-convective boundary, and an adiabatic profile below the boundary. The pressure of the radiative-convective boundary can span from 1 bar to over 1 kbar, mainly depending on the intrinsic effective temperature and equilibrium temperature of the planet (Fortney et al. 2007). To simulate this temperature structure, the default settings for the atmosphere in MAGRATHEA include an isothermal atmosphere at  $P < 100$  bar to approximate the radiative temperature gradient, and an adiabatic temperature gradient at  $P \geq 100$  bar. The mean molecular weight of each gas EoS is fixed. The dependence of planetary radius on atmosphere mean molecular weight is explored in Fig. 2.7.

Radiative temperature profile and coupled atmosphere-interior models such as Mousis et al. (2020) are potential future avenues of work. Additionally, we anticipate that future versions of MAGRATHEA will include non-ideal atmospheres from Saumon et al. (1995) and Chabrier et al.

(2019).

## 2.4 Known Limitations

We design MAGRATHEA with a focus on extensibility. MAGRATHEA permits users to extrapolate EoS functions beyond the temperature and pressure bounds from experimental and theoretical works. The phase diagram can be set up to allow a material where it would not be physical (e.g. use water in place of supercritical water). If the integrator passes through these extrapolated regions, it may find an incorrect solution or may fail to continue to integrate. Here we detail some limitations one should be aware of for each layer with our current defaults.

For the core, the liquid iron EoS from Dorogokupets et al. (2017) has no solution when the temperature of a given step gives a thermal pressure much larger than the total pressure at that step. This occurs most often when the iron core outer boundary is near the surface of the planet and at unusually high temperatures. In this case, a *no solution found* tag will be returned.

Extrapolated EoS functions may have two density solutions that satisfy the equation set at given  $P$  and  $T$ . The nonphysical solution typically has a lower density and the  $\frac{\partial \rho}{\partial P} < 0$ . The Newton's method density solver may converge to the incorrect branch at a transition from a low density phase to a higher density phase because the initial density guess of the high density phase is too small. We experienced this problem in the mantle when transitioning from Si melt to Brg from Oganov & Ono (2004) at low pressures. To avoid this, if the initial density guess gives  $\frac{\partial \rho}{\partial P} < 0$ , a density larger than  $\rho(P = 0, T = T_0)$  will be applied as the initial density guess of the Newton's solver, instead of the density solution of the previous step.

For the hydrosphere, users should be aware that MAGRATHEA will use the water EoS and return

a constant temperature even if the water would be in the vapor or supercritical phase. Because water EoS is softer and the thermal expansion is not included, the density is overestimated in supercritical regions. This may lead to a density drop at the phase transition from supercritical fluid to Ice X. Other phases without thermal parameters, such as Ice X, will return a constant temperature. Lastly, the adiabatic portion of the default atmosphere quickly rises in temperature and pressure and could force internal layers into extreme regions of the phase diagram. Ideal gas atmospheres with constant mean molecular weight are less realistic for large gas envelopes with pressures over 0.1 GPa (Zeng et al. 2021; Nixon & Madhusudhan 2021).

## 2.5 Test Problems and Utility

### 2.5.1 One-Earth Mass and Comparison with ExoPlex

We turn our attention to showing the outputs and utility of MAGRATHEA. We first simulate a one-Earth mass, two-layer planet with our full solver. The planet has a structure similar to Earth with 33 per cent of its mass in the core (Stacey & Davis 2008). With the default EoSs described in Sec. 2.3.4 and a surface temperature of 300 K, MAGRATHEA produces a planet with radius of 6166 km or  $0.967 R_{\oplus}$ . Fig. 2.4 shows the pressure, density, and temperature found throughout the planet.

Our default model differs from a detailed model of Earth in that our mantle is only Brg/PPv, the core has no lighter elements, and there is thermal equilibrium between the layers. Rather than choosing our default settings, users can choose to use an iron-silicate alloy EoS (Wicks et al. 2018) in the core and PREM in the mantle. The user can also start the mantle hot at 1600 K and implement a 2900 K jump across the core-mantle boundary which creates a layer of liquid iron.

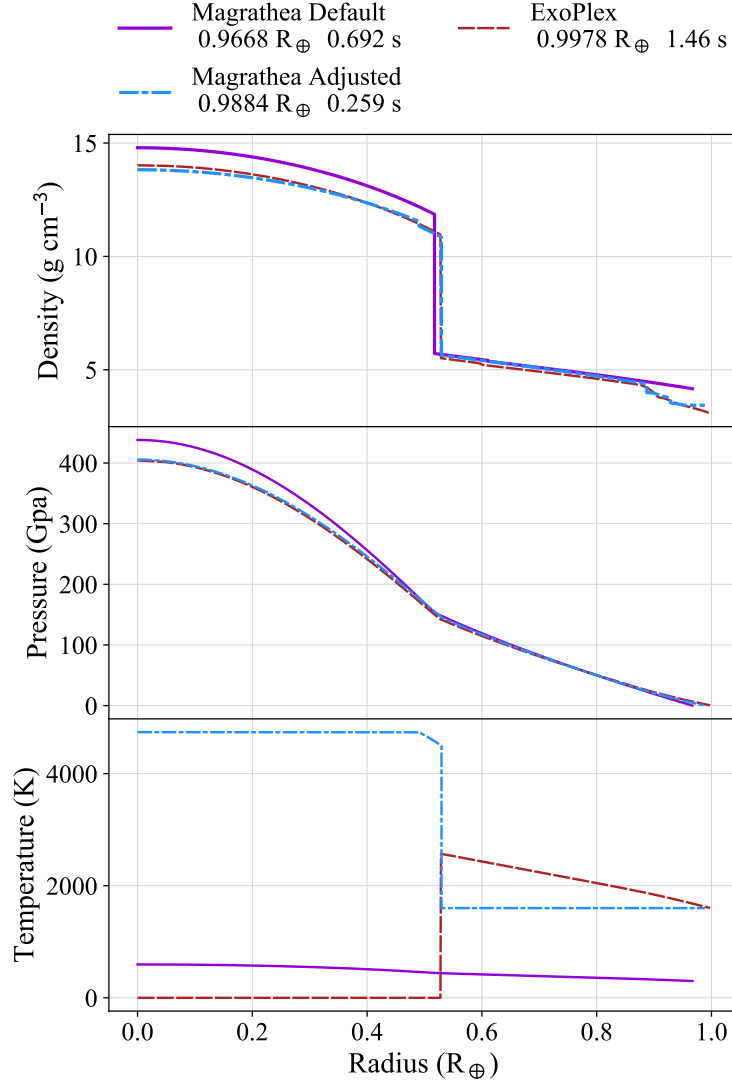


Figure 2.4: Density, pressure, and temperature verses radius solution for a two-layer, one Earth-mass planet with 33 per cent by mass core. The three models shown are *Magrathea Default* with hcp-Fe core (Smith et al. 2018) and Brg/PPv mantle (Oganov & Ono 2004; Sakai et al. 2016), *Magrathea Adjusted* with Fe-Si alloy core (Wicks et al. 2018) and PREM mantle (Zeng et al. 2016) and a temperature discontinuity, and the default settings in *ExoPlex*. *Magrathea Default* is set to 300 K at the surface while *ExoPlex* suggests a 1600 K mantle. Temperature is solved throughout *Magrathea Default* and in *ExoPlex*'s mantle. *Magrathea* returns no change in temperature when a phase does not have temperature parameters available while *ExoPlex* returns zero Kelvin. The planet's radius and the average run time over 100 integrations is listed in the legend.

This “adjusted” model, shown in Fig. 2.4, has a radius within 1.16 per cent of the radius of Earth ( $0.9884 R_{\oplus}$ ).

We compare our Earth-like planets to one created with a version of *ExoPlex*<sup>4</sup>, an open-source interior structure solver written in Python. *ExoPlex* is used in Unterborn et al. (2018); Unterborn & Panero (2019); Schulze et al. (2021b). The code uses a liquid iron core (Anderson & Ahrens 1994) and self-consistently calculates mantle phases with *Perple\_X* (Connolly 2009) using EoS for mantle materials from Stixrude & Lithgow-Bertelloni (2005). *ExoPlex* comes with predetermined grids of mineralogy to capture the mantle chemistry of planets between  $0.1$  and  $\sim 2 M_{\oplus}$ .

As seen in the top panel of Fig. 2.4, *ExoPlex* captures changes in density in the upper mantle that our Brg/PPv model does not. *ExoPlex* creates an Earth-like planet with a radius of  $0.9978 R_{\oplus}$  which is 3.2 per cent larger than our default planet and 1.0 per cent larger than our adjusted model. At least half of this difference is from a different choice in core EoS; *ExoPlex*’s innermost density is  $14.0$  while our default is  $14.8 \text{ g cm}^{-3}$ . The rest of the difference is *ExoPlex*’s ability to capture upper-mantle chemistry which decreases the density from our default for approximately 15% of the planet’s mass.

### 2.5.2 Run Time

We perform timing tests for both MAGRATHEA and *ExoPlex* for 100 repeat simulations of the Earth-like planet from the above section. MAGRATHEA takes on average  $0.69 \text{ s}$  to converge. This is 2.1 times faster than *ExoPlex* ( $1.46 \text{ s}$ ). The “adjusted” model uses a tabulated EoS for the mantle and a core EoS with no thermal information, thus most of the planet is isothermal with temperature only solved in the small region of liquid iron. This model runs 5.6 times faster than

---

<sup>4</sup><https://github.com/CaymanUnterborn/ExoPlex>

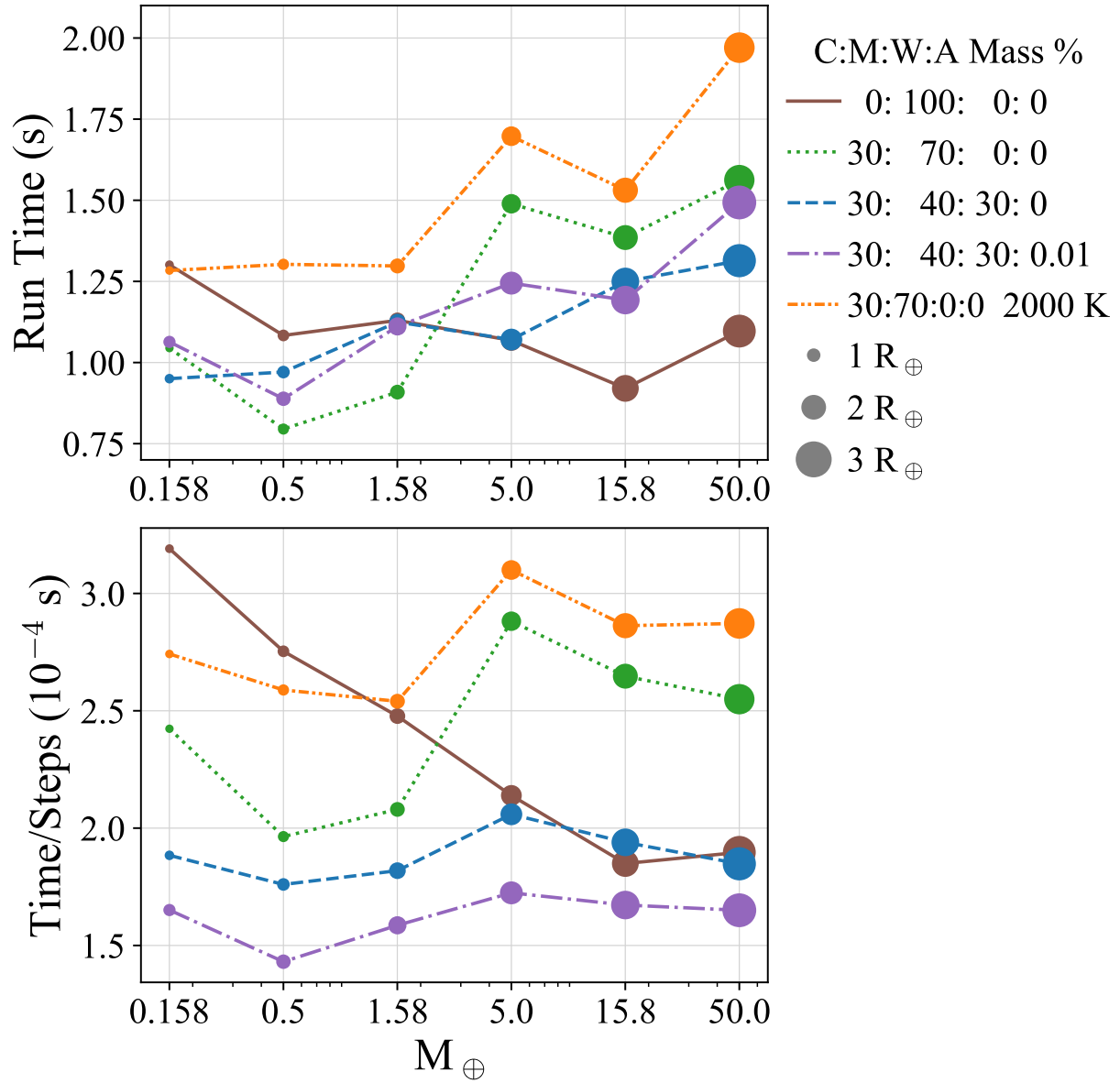


Figure 2.5: Plot of run time, *top*, and of run time divided total number of steps, *bottom*, for our default model across six planet masses and four compositions: 100% core, 30% core 70% mantle, 30% core 40% mantle 30% water, and 30% core 40% mantle 29.99% water 0.01% H/He atmosphere with 300 K surface temperature. The last set of planets, *orange*, have 30% core, 70% mantle, and surface temperature of 2000 K. The run time is the average time measured across 100 runs. Sizes of the markers are proportional to the planet radius.

*ExoPlex*. Average times are also listed in Fig. 2.4.

The run time of MAGRATHEA is dependent on the mass of the planet, the user's choice of planet model, and the error tolerances. In Fig. 2.5, we show run times of some typical planet masses and compositions with our default settings. Four compositions are run with a surface temperature of 300 K. A final set has a surface temperature of 2000 K which has a region of silicate melt at the surface. The figure shows that time remains near one second, but is not easily determined by input mass and composition. Here the average run time is 1.2 seconds. The longest and shortest run times are a factor of 2.5 times slower/faster. These solutions take between 15 and 30 iterations, and the final solutions have between 520 and 840 steps in mass.

In general the run time increases with mass, though not strictly since the step size is adaptable. Crossing phase or compositional boundaries costs an insignificant amount of run time. However, certain phases may take shorter or longer to solve. The planets with atmospheres have the most compositional layers, but the ideal gas solves quickly resulting in the shortest time per step. The runs which take the longest to converge are large, hot planets with a surface of silicate melt and large mantles.

### 2.5.3 Uncertainty from Equation of State

MAGRATHEA's structure allows the user to change the EoS and test their effects on planet structure. In Fig. 2.3, we show how choice of EoS can change the radius of single layer planets of masses from one to ten Earth-masses. For the hydrosphere, further discussed in Huang et al. (2021), new measurements of Ice VII, Ice VII<sub>t</sub>, and Ice X change the resulting planet radius from those in Zeng et al. (2016) by 1-5 per cent across this range of masses.

Table 2.2: EoS parameters for Smith et al. (2018), Sakai et al. (2016), and Grande et al. (2022) with uncertainty and the uncertainty in radius for a  $10 M_{\oplus}$  single-layer planet from uncertainty in EoS parameters.

Phase	TP GPa	$V_0$ $\text{cm}^3 \text{mol}^{-1}$	$K_0$ GPa	$K'_0$ GPa	$\sigma_R/\mu_R$ for $10 M_{\oplus}$ %
Fe HCP	-	6.625	177.7(6)	5.64(1)	0.089
PPv	112.5(8.1)	24.73	203(2)	5.35(9)	0.19
ice-VII	-	12.80(26)	18.47(4.00)	2.51(1.51)	0.24
ice-VII <sub>t</sub>	5.10(50)	12.38(16)	20.76(2.46)	4.49(35)	
ice-X	30.9(2.9)	10.18(13)	50.52(16)	4.5(2)	

The mantle’s EoS has the smallest effect on radius in agreement with Unterborn & Panero (2019). Comparing the tabulated EoS from PREM to our default mantle, we find that the radii of pure mantle planets differ by less than one percent for  $2\text{--}5 M_{\oplus}$ . Planets  $<2 M_{\oplus}$  have a larger difference in simulated radii. Capturing the density of the upper mantle is more important for these smaller planets.

HCP iron measurements generally agree when looking at bulk planet properties. However, it is uncertain how much lighter elements can be incorporated into a planet’s core. Included in MAGRATHEA are two silicate alloy EoSs from Wicks et al. (2018). Using a 15 per cent by weight silicate alloy EoS results in a  $1 M_{\oplus}$ , core-only planet that differs by five per cent in radius to our default. For comparison to the above radius changes, the 1-sigma uncertainties in radii of the seven Trappist-1 planets are 1-2 per cent (Agol et al. 2021).

A single measured EoS also has uncertainties in its own parameters. MAGRATHEA includes the ability to modify an EoS at run-time to determine the effects that measurement uncertainty has on a planet radius estimates. This feature is available in *input\_mode* 3, 4, and 5. It’s implementation is further detailed in Appendix 2.7. The first two modes are limited to using the isothermal *twolayer*



solver explained in Sect. 2.3.2. The *input\_mode=5* runs the full model with user specified planet composition and mass. MAGRATHEA iterates over EoS parameters from an input file and outputs the planet radius for each EoS modification.

In Table 2.2, we show the reported uncertainties in three experimental EoS from Sakai et al. (2016); Smith et al. (2018); Grande et al. (2022). We model  $10 M_{\oplus}$  planets each with a single layer. We then modify the EoS of that layer from 1000 values of the reference volume, bulk modulus, and the derivative of the bulk modulus drawn from Gaussians centered at the reported mean and using the given uncertainties. For the 100 per cent mantle and 100 per cent hydrosphere models we also draw 1000 values of the transition pressure (TP) between phases. The mantle planets have a Brg phase, but it's parameters are held constant as they are derived from *ab initio* simulations. The resulting uncertainty in planet radius for each single-layer model is  $< 1$  per cent for  $10 M_{\oplus}$  planets. Although the choice of EoS is of more consequence to a single measurement's uncertainty, this module allows users to investigate new measurements and their associated uncertainties.

#### 2.5.4 Ternary Diagram

In Section 2.3.4, we show mass-radius relationships for single-layer planets. However, these relationships are not unique when considering a planet with three or more layers. For a three-layer planet, ternary diagrams provide a way to visualize the radius parameter space for a planet with a certain mass (conversely we could show the various masses for a certain radius). Ternary diagrams have been used for exoplanet interiors in Valencia et al. (2007a), Rogers & Seager (2010), Madhusudhan et al. (2012), Brugger et al. (2016), Neil & Rogers (2020), and Acuña et al. (2021).

The location of a point on the equilateral triangle is given by the percentages of mass in the

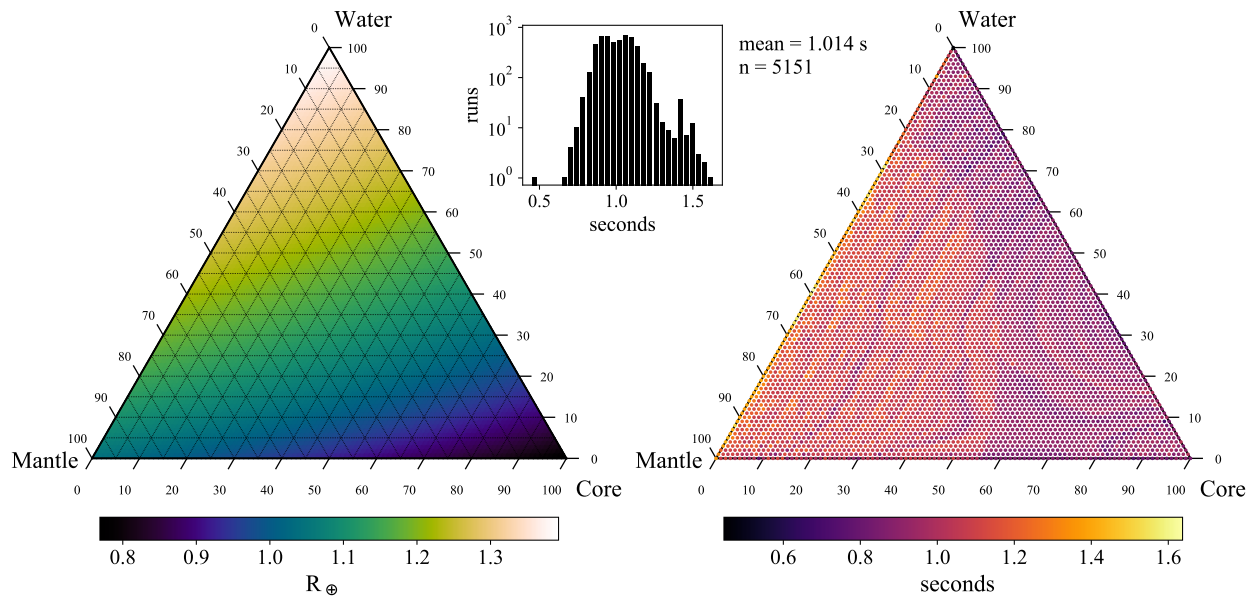


Figure 2.6: *Left*, ternary diagram where the axes are the percentage of mass in a core, mantle, and water/ice layer. The radius in Earth radii is shown by the color scale for 5151, one Earth-mass planets at integer percentages with our default model. Color map is interpolated between the simulations. *Right*, plot of MAGRATHEA’s run time for each planet. *Middle*, histogram of run time on a log-log scale showing mean time of 1.014 seconds. Ternary plots are generated with the python-ternary package by Harper et al. (2015) with colormaps from Van der Velden (2020).

three layers—core, mantle, and water. The three coordinates add to a constant 100%. Since axes are interchangeable, we decide to use the same representation as Zeng & Seager (2008). With this orientation the core to mantle ratio increases along the bottom axes and the water percentage increases perpendicular to the bottom axis.

We include with MAGRATHEA, a ternary plotting python script that uses python-ternary by Harper et al. (2015). To run 5151 planets with integer percentages of mass in each layer we use MAGRATHEA’s bulk input mode (*input\_mode=6*). This function requires an input file that contains each planet’s total mass and the mass fraction of core, mantle, and hydrosphere. Any mass not allocated to a layer is put into an atmosphere layer.

In Fig. 2.6 *left* each position on the triangle gives the radius of a unique one Earth-mass planet. We use planets in thermal equilibrium, a 300 K surface temperature, and with our default EoSs. This model underestimates the Earth’s radius as discussed in Sec. 2.5.1. A dry, one Earth-mass, and one Earth-radius planet in these simulations has approximately a 19 per cent core mass fraction (cmf). Because of the difference between water’s and iron’s density, we can see that the radius varies most dramatically along the water-core axis. A one Earth-mass and Earth-radius planet is also consistent with having 75 per cent cmf and 25 per cent of mass in a hydrosphere.

The entire suite of simulations needed for the one Earth-mass ternary takes approximately 87 minutes to complete. The time for each run is shown in Fig. 2.6, *right*. The average run time is 1.014 seconds. In agreement with Fig. 2.5, time has a weak correlation with mantle percentage.

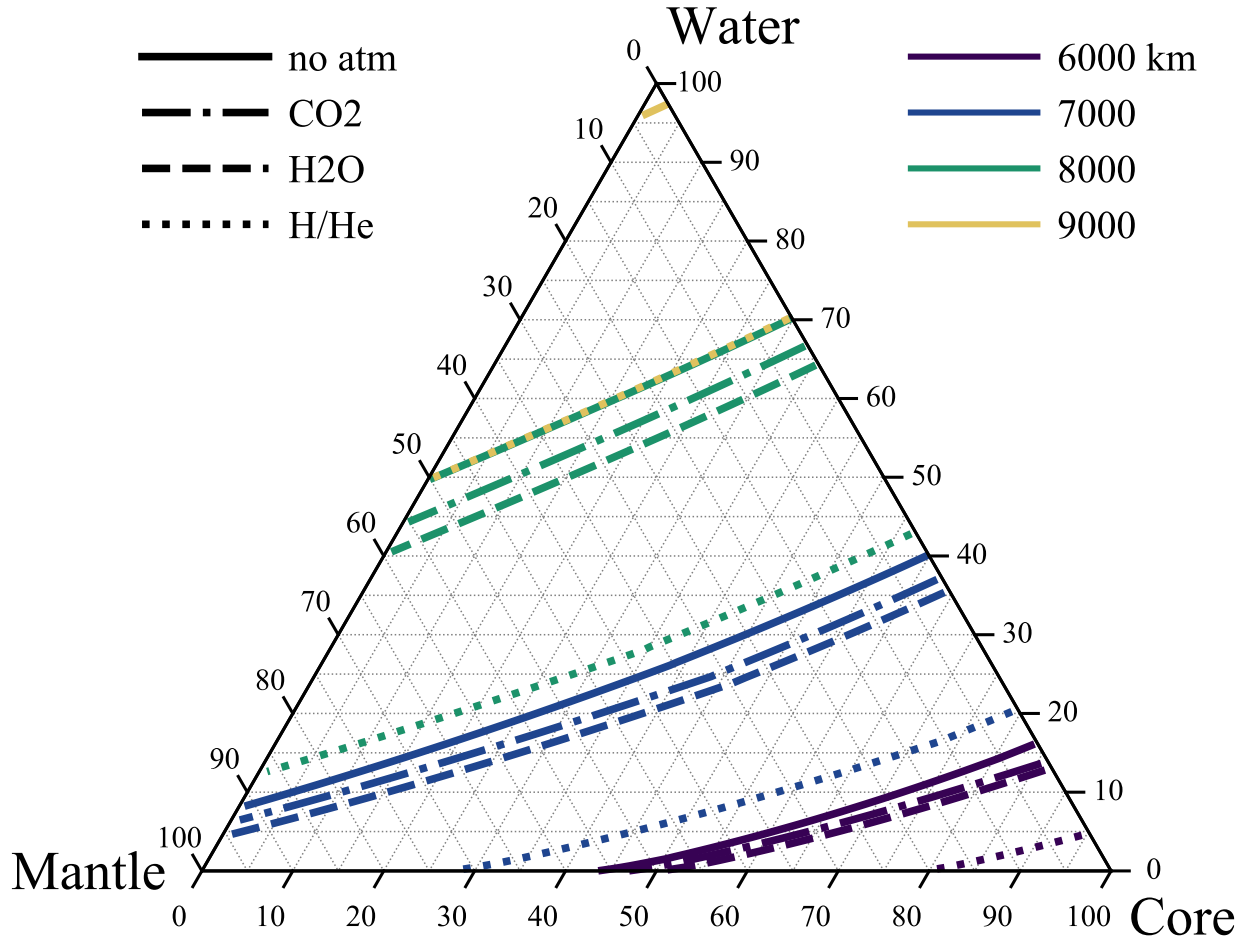


Figure 2.7: Core-Mantle-Water mass percentage ternary plot with colored contours of constant radius for one Earth-mass planets. Four types of planets, represented by the line-style, are calculated: one with no atmosphere and three with 0.01 per cent of their mass in an atmosphere layer. The atmosphere mass was subtracted equally from both the mantle and core to keep total mass equal to one Earth-mass. The three atmospheres have varying mean molecular weight:  $\text{CO}_2$  with  $44 \text{ g mol}^{-1}$ ,  $\text{H}_2\text{O}$  with  $18 \text{ g mol}^{-1}$ , and  $\text{H/He}$  mixture with  $3 \text{ g mol}^{-1}$ .

### 2.5.5 Ternary with Atmosphere

As a final example, we add an atmosphere to our ternary planets using our default two “phase” ideal gas atmosphere. In Fig. 2.7, we show contour lines of constant radius. The solid lines come from Fig. 2.6. The 5151, one Earth-mass planets are simulated again with 0.01 per cent of their mass taken equally from the core and mantle and put it into an atmosphere layer. This is comparable to the atmospheric mass fraction of Venus. Three types of ideal gas are used with varying molecular weight.

A small atmosphere of a hydrogen/helium mixture inflates the planets by almost 1000 km for all interior structures. A 6000 km, one-earth mass planet with a small H/He atmosphere is consistent with a 2-layer planet of 20:80 mantle:core (intersection of mantle-core axis, bottom) or 5:95 water:core (intersection of core-water axis). Together, the one Earth-mass ternaries explore the radii of a large range of possible interior (plus atmosphere) structures.

## 2.6 EoS Storage Structure

Calculating the density for a variety EoS formulae or tabulated EoS is packaged in the structure *EOS* declared in *EOS.h* and accomplished in *EOS.cpp*. The EoS of each phases needed for the calculation is an object of the *EOS* structure.

The name of pointers to *EOS* objects should be declared as an external variable in the header file *EOSlist.h* and then accomplished in *EOSlist.cpp*. To use the formula method, user should create a dictionary style two-dimensional double array with a shape of  $(length, 2)$ , where *length* is the number of provided EoS parameters. Table 2.3 - 2.5 explains all acceptable parameters. In the array, the first number of each row is the index key of the parameter according to Table 2.5. The

Table 2.3: Index for types of isothermal EoS formulae

Index	Function Name	Comment
0	BM3	3rd order Birch-Murnaghan <sup>a</sup>
1	BM4	4th order Birch-Murnaghan
2	Vinet	
3	Holzapfel	
4	Keane	
5		Empty
6		Ideal gas law
7		Interpolation
8-12	Same as 0-4	In combination with RTPress

<sup>a</sup> Default

second number is the value in the required unit. Not all spaces in the table need to be filled up. Not available values can be skipped.  $V_0$  and  $m_{mol}$  are required for all types of EoSs.  $K_0$  is required for condensed phase material.  $\gamma_0$  and  $\beta$  are required for isentropic temperature profile and thermal expansion. The minimum required parameters can be determined by the corresponding formulae listed in Section 2.2.2 and default values in Table 2.5.

Then the EoS object pointer can be constructed using the EoS constructor that have three arguments. The first one is a string of the phase description, then is the name of dictionary style double array, and the third argument is *length*, the number of parameters provided. The name of the EoS object pointer should be the same as the one declared in *EOSlist.h*.

The following shows the EoS of post-perovskite phase of  $\text{MgSiO}_3$  in the code as an example.

Code in *EOSlist.h*

```
\\Declare pointers to EOS objects

extern EOS *Si_PPv_Sakai;
```

Code in *EOSlist.cpp*

Table 2.4: Temperature profile option <sup>a</sup>

Index	Temperature profile calculation method
0	No temperature profile, must be isothermal
1	External entropy function
2	External temperature gradient function <sup>b</sup>
3	Ideal gas
4	EoS is fitted along isentrope <sup>c</sup>
5-7	Isentropic curve <sup>d</sup>
8	RTPress
9	Thermal expansion <sup>e</sup>

<sup>a</sup> Only need to specify this option in the input list if using external entropy function or external temperature gradient function (index 1 or 2), or the EoS is fitted along isentrope (index 4). Otherwise, the code will determine the option based on the parameters provided.

<sup>b</sup> The only method to set the gradient is using the `modify_extrn_dTdP` function.

<sup>c</sup> Selecting this option requires parameters to calculate Debye thermal pressure in Eq. 2.15. The isentrope temperature profile is enforced to the phase with this option even the isothermal option is chosen for the planet solver.

<sup>d</sup> Selecting this option requires parameters to calculate Debye thermal pressure in Eq. 2.15.

<sup>e</sup> Selecting this option requires  $\alpha$  and  $c_p$ .

Table 2.5: List of EoS parameters

Index	Variable	Unit
Comment		
0	EoS formula type	
1	$V_0$	$\text{cm}^3 \text{mol}^{-1}$
2	$K_0$	GPa
3	$K'_0$	
Default 4		
4	$K''_0$	$\text{GPa}^{-1}$
5	$m_{mol}$	$\text{g mol}^{-1}$
6	$P_0$	GPa
7	$\Theta_0$	K
Default 1		
8	$\gamma_0$	
9	$\beta$	
Fitting parameter of Grüneisen (see Eq. 2.13 and 2.24)		
10	$\gamma_\infty$	
Fitting parameter of Grüneisen (see Eq. 2.14). Default 2/3		
11	$\gamma'_0$	
12	$e_0$	$10^{-6} \text{K}^{-1}$
Helmholtz Electronic contribution (see Eq. 2.12). Default 0		
13	$g$	
Electronic analogue of the Grüneisen (see Eq. 2.12)		
14	$n$	
Number of atoms in the chemical formula <sup>a</sup> Default 1		
15	$Z$	
16	$T_0$	K
Reference temperature (see Eq. 2.7). Default 300		
17	$\alpha_0$	$10^{-6} \text{K}^{-1}$
The zeroth order coefficient of thermal expansion at a $P_0$		
18	$\alpha_1$	$10^{-6} \text{K}^{-2}$
The first order coefficient of thermal expansion at $P_0$		
19	$\xi$	
Power law index for thermal expansion (Eq. 2.28). Default 0		
20-22	$c_{p0}$	$10^7 \text{erg g}^{-1} \text{K}^{-1}$
Coefficients for specific heat capacity at constant pressure (see Eq. 2.30)		
23	Debye_approx	
Positive number for Debye, otherwise Einstein		
24	thermal_type	
See table 2.4		

<sup>a</sup> Number of atoms in the volume of  $V/N_A$ , where  $N_A$  is the Avogadro constant. The  $n$  of ideal gas is the number of atoms per molecule for the purpose of adiabatic index.



```
\\ Dictionary style double array
```

```
double Si_PPv_Sakai_array[][2]
```

```
= { {0,4}, {1,24.73}, {2,203}, {3,5.35},  
    {5,mMg+mSi+3*mO}, {8,848}, {9,1.47},  
    {10,2.7}, {11,0.93}, {15,5}};
```

```
\\ Create a EOS object pointer
```

```
EOS *Si_PPv_Sakai  
  
= new EOS("Si_PPv_(Sakai)",  
Si_PPv_Sakai_array ,  
  
sizeof(Si_PPv_Sakai_array)/2  
/ sizeof(Si_PPv_Sakai_array[0][0]));
```

For RTpress EoS framework, a list of additional polynomial fitting terms  $b_n$ , in the unit of  $\text{erg mol}^{-1}$ , are required (see Eq. 2.21). A separate array and its size *blength* are used to construct a RTpress EoS object. The following shows the EoS of liquid  $\text{MgSiO}_3$  as an example.

Code in *EOSlist.h*

```
extern EOS *Si_Liquid_Wolf;
```

Code in *EOSlist.cpp*

```
double Si_Liquid_Wolf_array[][2]
```

```
= { {0,10}, {1,38.99}, {2,13.2}, {3,8.238},  
    {5,mMg+mSi+3*mO}, {9,0.1899}, {10,0.6},  
    {12,-1.94}, {15,5}, {17,3000}};
```

```

double Si_Liquid_Wolf_b[]
= {4.738E12, 2.97E12, 6.32E12,
-1.4E13, -2.0E13};

EOS *Si_Liquid_Wolf
= new EOS("Si_liquid_(Wolf)",
Si_Liquid_Wolf_array, Si_Liquid_Wolf_b,
sizeof(Si_Liquid_Wolf_array)/2
/sizeof(Si_Liquid_Wolf_array[0][0]),
sizeof(Si_Liquid_Wolf_b)
/sizeof(Si_Liquid_Wolf_b[0]));

```

## 2.7 Modify a Built-In EoS in Runtime

Once an EoS is built-into the code, it is possible to modify its parameter in the run-time without the request of recompile the full code. This feature is useful to rapidly repeat runs with similar EoS parameters, for example when study the impact of the uncertainty of EoS parameters on planet size.

One can modify one parameter of a EoS using

```

void EOS::modifyEOS
(int index, double value),

```

where index is listed in Table 2.5. Or using

```

void EOS::modifyEOS
(double params[][2], int length)

```

to modify multiple parameters at once, where *length* is the number of parameters that need to be modified and *params* is the dictionary style 2D double array (see Appendix 2.6).

If the phase boundary between phases are independent of temperature and purely determined by the pressure, e.g. the phase boundary commonly assumed between ice VII and ice X, the phase transition pressure within a layer can also be modified using

```
void set_phase_highP  
(int k, double *start_pressure ,  
EOS** phase_name) ,
```

where *k* is the number of phases involved in this modification, *phase\_name* is an array of EoS pointers of these *k* phases, and *start\_pressure* is the array of phase transition pressures between these *k* phases in the unit of GPa with a length of *k*-1. If the name of the first EoS in the *phase\_name* EoS list matches the name of one of the original EoS of this layer, the first input EoS will replace the original one. Otherwise, the first EoS in the list will be ignored in the calculation.

External EoS function, entropy function, or temperature gradient function can be modified using

```
void modify_extern_density  
(double (*f)(double P, double T)) ,  
void modify_extern_entropy  
(double (*g)(double rho , double T)) ,
```

or

```
void modify_dTdP  
(double (*h)(double P, double T))
```

respectively.

## 2.8 Summary

In this chapter, I presented MAGRATHEA, an open-source planet interior solver, as collaborators and I published in Huang et al. (2022). MAGRATHEA is available at <https://github.com/Huang-CL/Magrathea>. Given the mass in the core, mantle, hydrosphere, and atmosphere, the code uses a shooting method to find the planet’s radius and internal conditions.

The code allows users to easily modify their planet models. Each layer is given a phase diagram where the EoS may change based on P-T conditions. Multiple formulations, both thermal and non-thermal, for the EoS are implemented. We document in this work our built-in library of EoSs and how to add new equations. Our default EoSs feature up-to-date experimental results from high-pressure physics. We show that the choice of planet model has an effect on inferences of planet composition.

The timings and results presented here show that MAGRATHEA is an efficient and useful tool for characterizing the possible interiors of planets. MAGRATHEA is currently under active development and we plan future expansions to the package. In this version, the isentropic temperature gradient is only available for the Ice VI and Ice VII in the hydrosphere. Further development of the code is detailed in Ch. 3 while expansions of the EoS library is described in Ch. 4. We describe future developments in the summary sections of each chapter. We encourage the community to contribute and use MAGRATHEA for their interior modeling needs.

## Chapter 3

### Further MAGRATHEA Developments

#### 3.1 Background

Open-source software is freely available for anyone to use, modify, and distribute. Anyone can easily access and use the software for their research. Although there are concerns about appropriate attributions, open-source resources remove the need for expensive licenses and proprietary restrictions. This accessibility can accelerate scientific progress.

In addition, open-source software is often more transparent and auditable than proprietary software. Because the source code is available, researchers can examine and modify the software to ensure it is working as intended and to adapt it to their specific needs. This transparency and accountability can increase the reliability and reproducibility of research.

Open-source software plays a critical role in astronomy. The open-source programming language, Python, is foundational to modern astronomy for data analysis. I use a number of open-source Python packages in this work including PYTHON-TERNARY (Harper et al. 2015), NUMPY (Harris et al. 2020), MATPLOTLIB (Hunter 2007), and CMASHER (Van der Velden 2020). Other open-source tools commonly used in astronomy include the Image Reduction and Analysis Facility (IRAF, Tody 1986) and ALADIN (Bonnarel et al. 2000) for astronomical catalogs.

The field of stellar interiors and evolution accelerated with the introduction of the open-source Modules of Experiments in Stellar Astrophysics (MESA, Paxton et al. 2011, which currently

has over 2500 citations). Computational methods for stellar interiors were first developed half a century before MESA in Iben & Ehrman (1962) and Henyey et al. (1964) based on theory by Chandrasekhar (1938) and Schwarzschild (1958). The computational tools improved in the early 2000 summarized in Lebreton et al. (2008). MESA’s publication, Paxton et al. (2011), now has over 2500 citations and led to many improvements and additional software even for gaseous planets in Chen & Rogers (2016). We see a similar evolution in planet interior models.

I describe our planet interior model in Chapter 2. MAGRATHEA at this time is the only open-source planet interior model with flexible model parameters. Our transparent structure allows for users to easily modify their models to their desired interior materials and conditions. This makes it a great platform to add functionality and couple various other models. We aim for it to become a community standard for interior modelling.

While, EoS-specific developments are described in Chapter 4. In this chapter, I describe a major update and a add-on that were created after Huang et al. (2022). In Sect. 3.2, I describe a compositional finder which finds interior solutions across 3-layer parameter space for a mass and radius of a planet and is used extensively in later chapters. In Sect. 3.3, I describe an add-on which represents one dimensional MAGRATHEA outputs in three dimensions. In Sec. 3.4, I focus on a list of future development that I aim to complete and partner with other researchers to add to or develop in concert with our interior solver.

### 3.2 Composition Finder

In the previous chapter in Sec. 2.5.4, I showed on a ternary diagram the range of radii for a given mass of planet with all possible 3-layer interior structures. On Fig. 2.6, you can see lines of

Table 3.1: Inputs for the composition finder with line numbers in *main.cpp*.

Variable	Details	Type	Line Number
filename	File of mass and radius	string	302
filename	Output file	string	334
–	OpenMP Options (schedule, num_threads)		343
step	Step size of r-cmf	double	346
rerr	Error tolerance in simulated radius to target radius	double	347
Tgap	Temperature of planet and discontinuities	vector	350

constant color which are planets having the same mass and radius. I developed a composition finder routine for MAGRATHEA which given the mass and radius of a planet finds this line of solutions to the interior structure. Furthermore, given observational uncertainties it finds solutions for many draws of mass and radius. I describe the routine here which can be utilized with *input\_mode=7* in *main.cpp*.

The composition finder takes in a tab separated file of mass and radius samples. These can be generated by fitting a Gaussian or two half-Gaussian to the observed median and standard deviation or can take samples of mass and radius from a observational pipeline. This more realistically captures the distribution of observed mass and radius. Besides simulating the skewness of each value, a combined analysis of mass and radius such as one utilizing transit timing variations will have a correlation between mass and radius. This correlation often is not accounted for in observed interior studies (e.g. Acuña et al. 2021). I explore the shape of distributions and how they affect inferences of planet composition in Sec. 6.4.1.

In addition to input and output file locations, the finder takes in the inputs from Table 3.1. Mass and radius are stored as double precision variables. The finder outputs the input mass, the mass and radius of each layer of the best fit planet, and the target radius as double variables in a tab separated file.

Each mass and radius does not have a unique three-layer solution, so I define the refractory core mass fraction (r-cmf) as the third variable to find solutions. R-cmf is the ratio of the core mass to the non-volatile mass and is given by

$$\text{r-cmf} = \frac{M_{\text{core}}}{M_{\text{mantle}} + M_{\text{core}}} \quad (3.1)$$

or the denominator can equally be expressed as the total mass minus the hydrosphere,  $M_{\text{tot}} - M_{\text{hydro}}$ . This quantity will be explored graphically in Sec. 6.2. The r-cmf in the case of our simple model with no silicate in the core and no iron in the mantle is equal to the  $\frac{\text{Fe}}{\text{Si}+\text{Fe}}$  ratio which may be called the Fe# in geoscience literature. R-cmf ranges from 0 to 1 including 0 and 1 and is not dependent on the hydrosphere mass. For example, Earth and Ganymede have similar r-cmf while Ganymede has half Earth's cmf at 16% (Kuskov & Kronrod 2005).

I sample the r-cmf space uniformly stepping from 1 to 0 in steps corresponding to the variable *step*. I most often use a step of 0.01 or 0.02 leading to 101 or 51 solutions to a mass and radius input. The solver starts the planet with 100% of the input mass in the core and solves a planet with the given temperatures from  $T_{\text{gap}}$  using the full MAGRATHEA solver. This gives the smallest radius for a given mass of planet, if the target radius is smaller than this the mass and radius measurement is non-physical for the given planet model. In this case an error is returned and the next mass and radius is solved.

If the target radius is larger than the 100% core planet than 0.1% of the mass is converted to hydrosphere mass and the radius of this new planet is found. I then use a secant method (Papakonstantinou & Tapia 2013) to find the optimal water mass fraction to match the target radius ( $R_{\text{targ}}$ ) with the rest of mass in the core. From the previous two radii ( $R_i$ ,  $R_j$ ) at the given water mass



fractions ( $f_{w,i}, f_{w,j}$ ), the next water mass fraction ( $f_{w,k}$ ) is found from

$$f_{w,k} = f_{w,j} - (f_{w,j} - f_{w,i}) \frac{(R_j - R_{targ})}{(R_j - R_i)}. \quad (3.2)$$

This is repeated until the error in the radius found compared to  $R_{targ}$  is within the given value of  $rerr$ . For an error of 0.1%, the finder takes approximately 5-6 runs. If an error occurs in the MAGRATHEA run an addition 0.01% of mass is converted to hydrosphere and the planet is run again.

The finder is then swept across decreasing r-cmf. The finder begins with cmf equal to r-cmf and the rest of the mass in the mantle. In the second iteration onward after determining the water mass fraction,  $f_w$ , to try the core mass fraction,  $f_c$ , is given by

$$f_c = \text{r-cmf} * (1 - f_w), \quad (3.3)$$

and the mantle mass fraction,  $f_m$ , by

$$f_m = (1 - \text{r-cmf}) * (1 - f_w). \quad (3.4)$$

The optimal water mass fraction is recorded for each r-cmf. When the initial planet's radius with no hydrosphere is larger than the target radius, there are no longer solutions at lower r-cmf and the finder moves to the next mass and radius measurement.

The routine is parallizeable with each mass and radius draw run on a different thread. I accomplish multithreading with OPENMP (Chandra et al. 2001). The entire routine is currently in *main.cpp*, but will be moved to the back-end with a callable function in *input\_mode=7*.

With average run times of 1 second and up to 600 runs needed to find solutions at steps of 0.01 in  $r$ -cmf for a mass and radius measurement, the finder takes approximately 10 minutes per mass and radius. I often run 5000 posterior input measurements of mass and radius which takes a maximum of 3 days across 12 cores. This scales linearly with step size and with number of inputs.

I use the same finder to assess atmosphere mass fractions. The atmosphere finder has two modes. First the finder can either work exactly as the hydrosphere finder by varying the  $r$ -cmf and finding the atmosphere mass as the third layer. The second option is for the user to set a  $r$ -cmf and the finder will find the atmosphere mass fraction across water mass fraction from 0% to 100% water (or a defined cutoff for physically possible water mass fractions).

I use this finder to characterize planet interiors in later chapter with many examples for different planets in Chapter 5 and variations on the Trappist-1 planets in Chapter 6. Previous works which use interior solvers to characterize planets from both mass and radius include Dorn et al. (2015); Santos et al. (2015); Dorn et al. (2017b;a); Brugger et al. (2017); Plotnykov & Valencia (2020); Baumeister et al. (2020) along with many individual observational studies. A majority of these studies use a Markov chain Monte Carlo (MCMC) method to characterize planets.

In the MCMC method, a greater number of model parameters can be explored than mass fraction in each layer. In Dorn et al. (2017b) they use MCMC to constrain the mass fraction of water and atmosphere along with the mantle Fe/Si and Mg/Si ratios. While we treat these ratios as an unknown space and generate solutions uniformly across this space, the MCMC treatment can take stellar inputs to constrain the probability of interior solutions. However, their more detailed model takes 40-90 seconds to run. In Unterborn et al. (2023), elemental ratios are set in their finder, but these are converted into mass fractions, the input of our code, through simple balances. Acuña et al. (2021) use a MCMC method built on Dorn et al. (2015), but only report the  $1-\sigma$  bounds of

interior solutions and not the distribution of results. In their models without stellar constraints, I expect their findings are uniform across r-cmf. My method can be more transparent in this case.

### 3.3 3D Planet Rendering

MAGRATHEA output files provide the radius, pressure, temperature, density, and phase at steps of enclosed mass. Although these results are 1-dimensional, the spherically-symmetric results can be used to visualize the planets in 3-dimensions. Giving the simulated planet interior results a visual representation in 3-dimensions helps our understanding of the volume of each planet material.

Blender is a free and open-source three dimensional software that can be used to create three dimensional models, animations, and simulations. Blender's physics engine allows users to create simulations of physics phenomena, such as fluid dynamics, soft body physics, and particle systems. It's powerful rigid body physics engine can be used to create realistic collisions, gravity, and other physical interactions between objects in a scene. Kent (2013) describes how Blender can be used in a number of astronomy sub-fields. Blender has an embedded Python interpreter that represents all actions in the Python language.

Sri Sudharsan, a high school mentee, and I are using Blender 3.3 to read in a tab separated output file from MAGRATHEA. We sort and record the radii where a phase transition occurs and store these points and name of material in a specified list. We then generate a primitive sphere at the outer radius of the planet and additional shells with a radius corresponding to each phase change. We give each material a specified color, roughness, and texture. We generally use grey/metallic textures for core materials, green or red for mantle, bright red for melted material, and blue for hydrosphere. Green is chosen for the mantle as a major component of the Earth's upper-mantle is

peridotite, a rock composed primarily of green-colored olivine.

The script has the flexibility to generate any planet from the outputs of MAGRATHEA. Running the Python code within the Blender’s scripting module will automatically create the planet to scale. We include this open-source package in our GitHub: <https://github.com/DavidRRice/Blender-Magrathea>.

In Fig. 3.1, we show the 3D representation of an Earth-like planet model along with the radial profile of density, pressure, and temperature. The planet is  $1 M_{\oplus}$  with a 32.5% core mass fraction. We start the mantle hot at 1800 K assuming a quick temperature rise in the thermally conductive lithosphere and add a 1700 K increase in temperature between the mantle and the core. The planet is made of forsterite, wadsleyite, ringwoodite, bridgmanite, magnesium silicate post-perovskite, liquid iron, and hcp iron. Each of these changes in material is represented by a change in color and texture in the interior.

In Fig. 3.2, we show a collection of planet interiors in 3D. We set up the camera to be the same distance from the planet with the same view, so all planets are to scale relatively in radius. Visible is many phases of water-ice and mantle materials. We use water/ice for the surface if the planet has a hydrosphere depending on the outermost material and a planet texture for the surface if the outermost layer in rock or iron.

Lastly, we are experimenting with coloring the planet by other interior characteristics. To color by a continuous variable, we apply to the sphere a radial “color ramp” for each layer. Blender color ramps can by default have 32 “color stops”. Thus we read in 32 densities within each layer or within the planet which are evenly spaced in density. We don’t record the exact radius of phase or layer changes, but MAGRATHEA returns more outputs around composition changes to resolve the exact location, so color stops are most often placed near large changes in density.

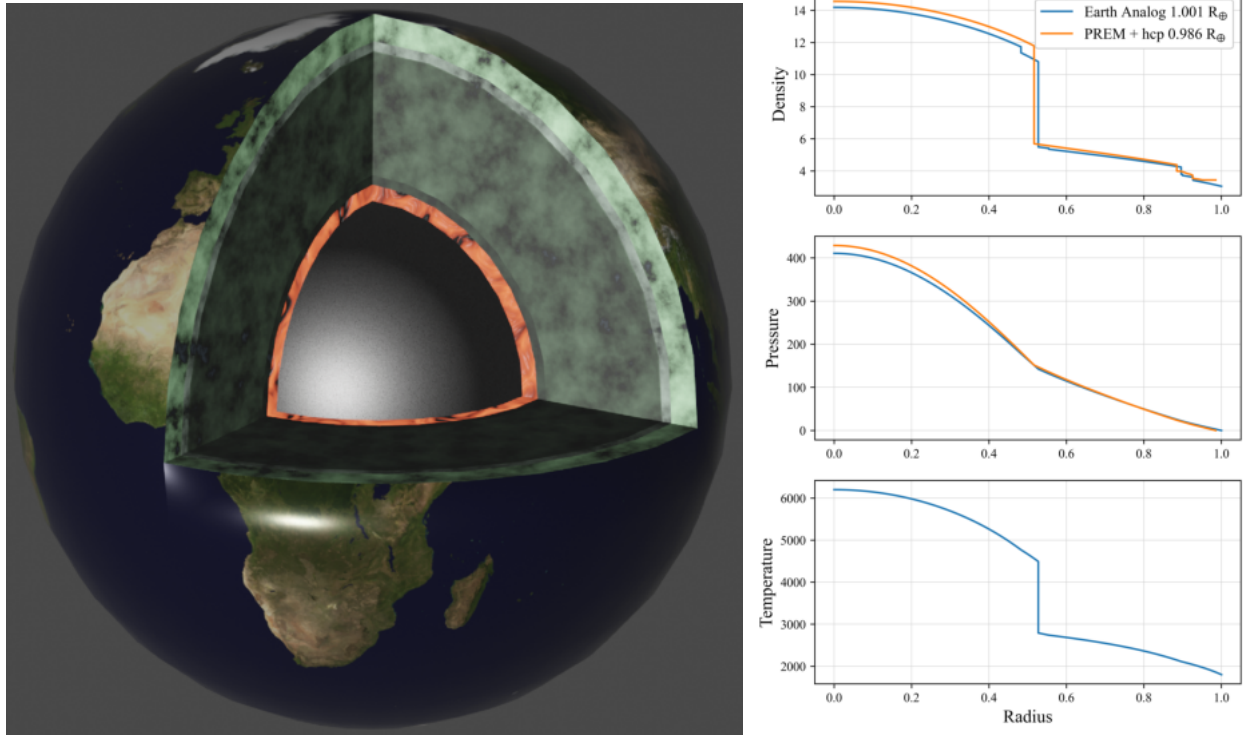


Figure 3.1: *Left*, a Blender rendering of an Earth-like planet with 32.5% of mass in the core with changes in mineralogy marked by changes in color in the interior. *Right*, in *blue* the density, pressure, and temperature of the Earth-like planet compared to a isothermal profile for PREM mantle and hcp-iron core. The radius of discontinuities in density on *top right* correspond with changes in color in 3D *left*.

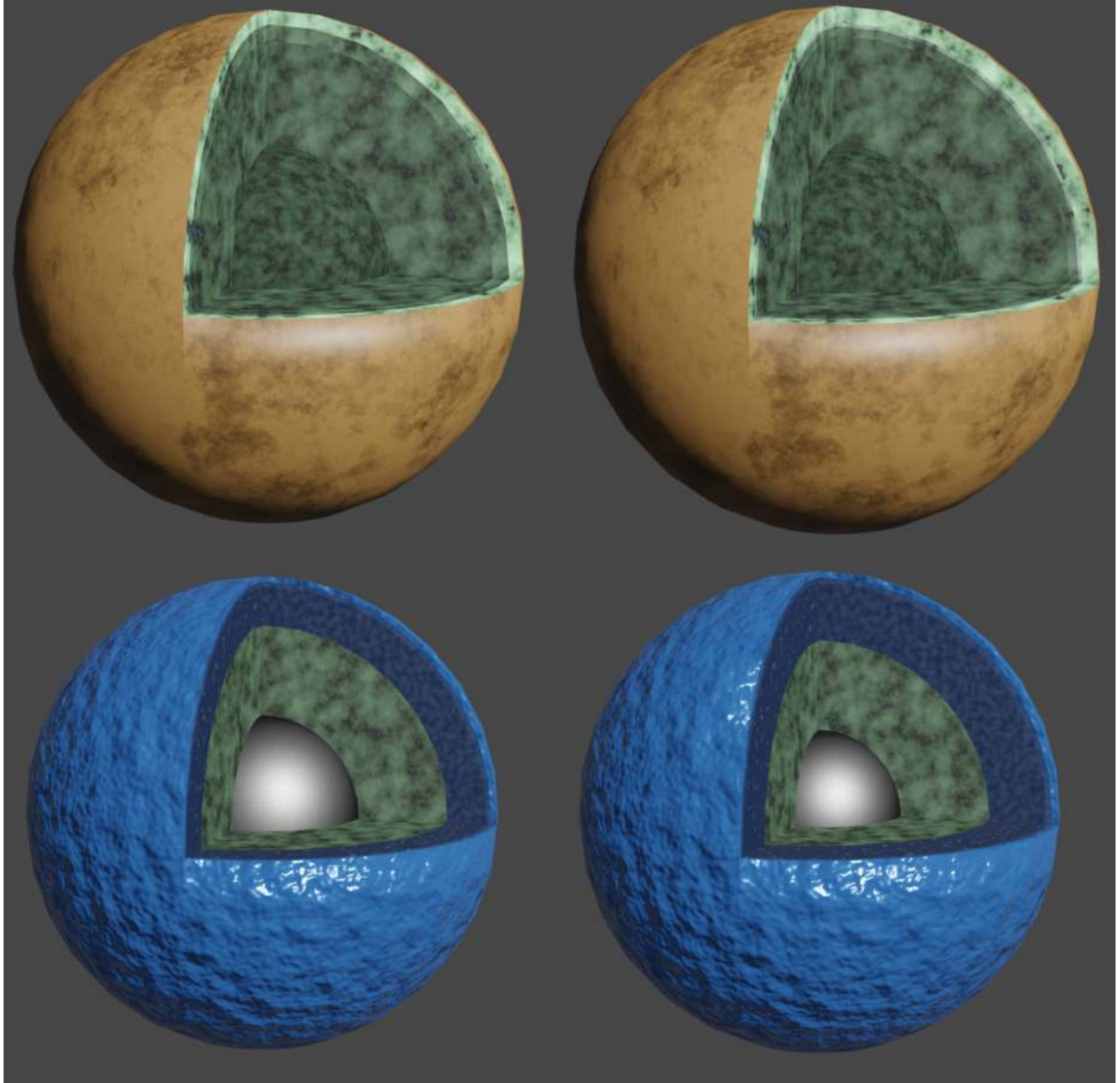


Figure 3.2: *Top*, 100% mantle planets. *Bottom*, planets with significant hydrospheres. *Top left*, planet that is  $1 M_{\oplus}$  and  $1.07 R_{\oplus}$  surface of 300 K. *Top right*, planet that is  $1.1 M_{\oplus}$  and  $1.1 R_{\oplus}$  and surface of 1000 K. The second planet's temperature leads to a wds layer shown in green/grey under the olivine layer. *Bottom left*, planet that is  $0.63 M_{\oplus}$  and  $0.97 R_{\oplus}$  with 42% core. *Bottom, right*, planet that is  $0.56 M_{\oplus}$  and  $0.99 R_{\oplus}$  with 35% core.

To apply the correct color at each location, we find each output density's linear position between a minimum,  $\rho_{min}$ , and maximum value,  $\rho_{max}$ , for each layer. The position,  $p$ , is given by

$$p = \frac{\rho_{max} - \rho}{\rho_{max} - \rho_{min}}. \quad (3.5)$$

We read in a Matplotlib colormap and find the color at each of those positions. We add color stops to the Blender colorramp at the radial position given the color and the colorramp interpolates between each output. We show the in-progress rendering in Fig. 3.3.

### 3.4 Summary and Future Development

In this chapter, I report two major updates to MAGRATHEA's functionality since the publishing of Huang et al. (2022). In Sec. 3.2, I describe my method for finding the range of possible interior structures that are solutions for a single mass and radius measurement. I will use this method extensively to characterize planets in Chapter 5 and Chapter 6. In Sec. 3.3, we take the interior conditions of a planet and represent them in three dimensions. We find this useful for visualizing the volume ratio of different components.

Looking toward the future we have a number of basic and extensive additions we aim to develop. In MAGRATHEA we prefer empirical fits for the EoS because they are lightweight in terms of storage and parameters can easily be adjusted and tested. However, we do have a two dimensional table input for the EoS. We use these to match the results of Seager et al. (2007). In the future, we plan to develop a three dimensional table interpolator for temperature dependent results also. This is important for inclusion of the AQUA package Haldemann et al. (2020), although their EoSs informing their tables can also be implemented without the use of tables. In addition

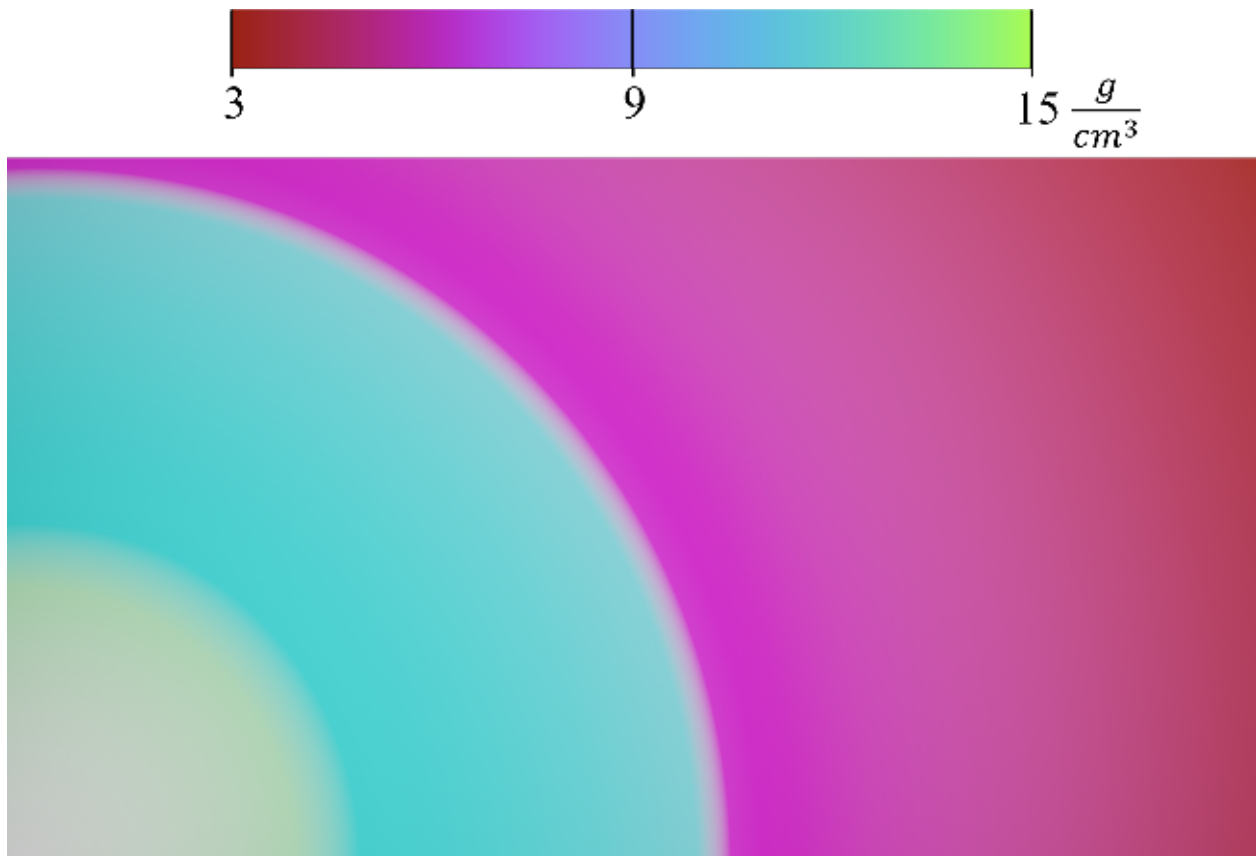


Figure 3.3: The density inside the Earth-like planet in Fig. 3.1. The density increases fairly linearly in the mantle with density jumps in the liquid outer core and solid inner core. The current method does not resolve the upper mantle materials well. Colors are rendered differently in Blender based on lighting and other “material properties” of the 3D sphere so may not correspond exactly to the colorbar.



EoS created with the quotidian EoS methodology which describe all solid or liquid phases from a free-energy model generally take the form of three-dimensional tables (More et al. 1988; Wu et al. 2019).

Future developments of MAGRATHEA focus on coupling the code to related equations and techniques to interior solvers. As the James Webb Space Telescope observes exoplanet atmospheres, interior models will need to couple to atmosphere models. Acuña et al. (2021) couples their interior model to an atmosphere model to find the properties of all 7 Trappist-1 planets including the hot planets, b and c, which, if water rich, would have a water vapor atmosphere. In most cases for small planets, the atmosphere can be solved separately and the pressure and temperature at the base used for a boundary condition. However, the next generation of models will want to consider the chemical abundances of both the atmosphere and interior, and inform one another based upon stable chemical phases.

A second future development is focused on the thermal evolution of planets. Interior models do not employ a standard assumption for the temperature profile inside of planets. While (Seager et al. 2007) uses an isothermal interior, other models start their mantle adiabat at the null albedo temperature (Baumeister et al. 2020) and ignore the rise in temperature from a thermally conducting lithosphere. Furthermore, the core temperature should be set from the energy of formation and requires a thermal evolution model. Thermal evolution models are thus needed to determine liquid layers in planets which generate magnetic fields—essential to habitability.

Like interior modeling, thermal evolution is dependent on material properties and thus is a natural extension of MAGRATHEA’s capabilities. Recently Zhang & Rogers (2022) coupled an energy balance model which considers conduction, convection, and radiogenic heating with an interior model to constrain the mass and core mass fraction (cmf) of planets which will have liquid

outer cores. The results are limited to forsterite-olivine upper mantles and pure iron cores.

To broaden their results, I aim to develop an open-source thermal model that couples to MAGRATHEA. I will then investigate a variety of planet materials. For example, majorite garnet, another component of the Earth's upper mantle, has nearly half the heat capacity as olivine (Giesting et al. 2004) leading to less thermal expansion and a lower convective heat flux. In addition, I will investigate a variable melting temperature for the core. Lastly, thermal models depend on the viscosity of rocky liquids which have large uncertainties and require further laboratory work. Through these investigations, I will develop standards for temperature profiles for interior modeling and continue the development of the MAGRATHEA platform of interior models.

## Chapter 4

### Advancements in EoS and Expansion of EoS Library

#### 4.1 Background

Material physics labs are pushing our measurements of planet-building materials to higher pressures and temperatures. Diamond anvil cells and shock experience make measurements up to several hundred gigapascals. Even theoretical works using density functional theory to derive *ab initio* equations of state fit their theories to these experimental data. Thus there is a need for inferences of planet compositions to stay up-to-date with experimental high-pressure physics and geology results. MAGRATHEA’s transparent structure for EoSs detailed in Sect. 2.6 allows users to easily expand and document our library of planet building materials.

To illustrate the importance of determining the response of materials to pressure (and temperature) and accurately using them in a planet solver, consider a planet made of pure gold and platinum (Adams 1995-2001 describes fantasy planets made from these materials for the galactic elite). The density and radius of two  $1 M_{\oplus}$  planets with adiabats starting at 300 K made of these materials is shown in Fig. 4.1. Gold ( $19.3 \text{ g cm}^{-3}$ ) is less dense at the “surface” of the planet than platinum ( $21.45 \text{ g cm}^{-3}$ ). However, the bulk modulus of gold from Matsui (2010) is 40% less than that of platinum from Matsui et al. (2009). This means gold is not as “stiff” as platinum and becomes denser quickly inside of the planet. Gold quickly becomes within 7.5% of the density of platinum. However, the first derivative of the bulk modulus of gold is 15% higher than platinum.

Thus, gold's density remains low resulting in a planet of  $0.53 R_{\oplus}$  compared to the  $0.52 R_{\oplus}$  radius of the platinum planet. Of note is how far interior models must extrapolate experimental results. Both materials are measured up to 250 GPa and 3000 K, but the central pressure and temperature of the gold planet is 3.2 TPa and 18700 K and the platinum planet is 3.5 TPa and 17000 K.

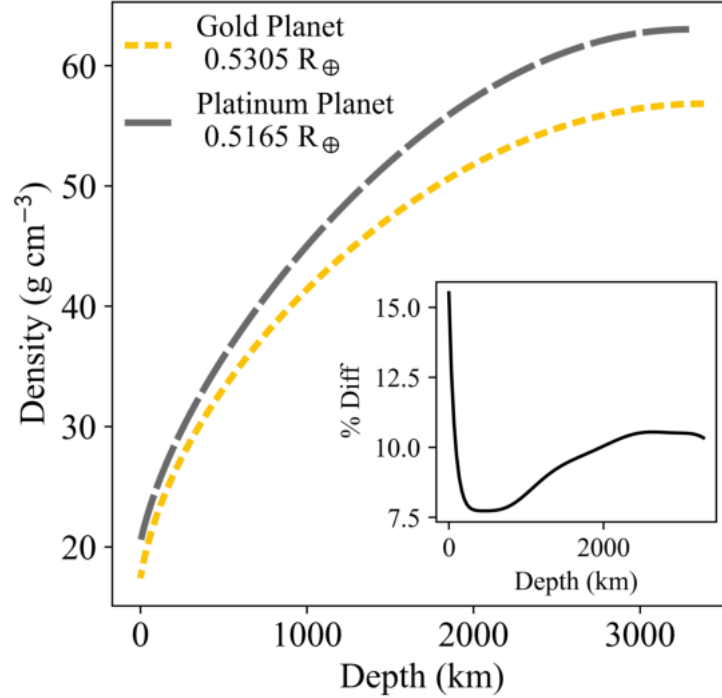


Figure 4.1: The density with depth of two  $1 M_{\oplus}$  planets made of pure gold and platinum. This is for illustrative purposes as planets are not made out of pure gold and platinum. Inset shows percent difference between the two planets' densities as a function of depth.

In this chapter, I detail our collaboration with high-pressure physicists to improve EoSs and expand our library in MAGRATHEA to include the most up-to-date planet building materials. In addition, I detail how these changes and improvements affect the characterization of planet interiors. In Sect. 4.2, I report the planet modeling I did in Huang et al. (2021) with a new water-ice

EoS from collaborators (Grande et al. 2022). In Sect. 4.3, I detail how I implement a new EoS from Smith et al. (2018) with missing thermodynamic parameters. In Sect. 4.4 and Sect. 4.5, we add lower pressure irons and silicates which are often ignored in planet modeling and summarize in Sect. 4.6

## 4.2 New Water-Ice Experimental EoS

Water,  $\text{H}_2\text{O}$ , is a fundamental building block of planets—being composed of two of the three most abundant elements in the universe. Water also has complex solid-state properties as the nature of the intermolecular bonds change with pressure and temperature. Measurements of the properties of water under conditions relevant to planetary interiors suffer from several systematic effects that have limited our understanding of its crystalline structure, compressibility, EoS, and phase boundaries. For example, the phase boundary between ice-VII and ice-X (the two dominant structures of ice above standard pressure) from various studies are inconsistent and give a broad range for the transition pressure that spans from 40 GPa to beyond 120 GPa (Hirsch & Holzapfel 1986; Guthrie et al. 2019)

Historically, the EoS of water-ice systems has been determined by compression of the sample with limited ability to address issues of non-hydrostaticity and the deviatoric stress that arises from high pressure methods associated with diamond anvil cell techniques (e.g. Frank et al. 2004). Recent measurements of the water EoS by Grande et al. (2022) applied new experimental techniques to alleviate some of these systematic effects. They used a mid-IR laser system to directly heat a water sample within a diamond anvil cell, melting and then recrystallizing the sample prior to making x-ray diffraction measurements of the structure.

Two key results from the Grande et al. (2022) work include: 1) the discovery, near 5 GPa, of a new phase of ice, denoted ice-VII<sub>t</sub>, which has a tetragonal crystalline structure rather than the cubic structure of neighbouring phases, and 2) an improved measurement of the pressure (near 31 GPa) where covalently bonded ice-VII transforms to the ionic bonded ice-X. Their measurements have important implications for the properties of water-rich planets – including bulk properties such as the mass-radius relationship and the fundamental nature of water trapped below the surface. In this work, we investigate how this new EoS could change the inferred bulk composition and structure of observed exoplanets.

The planet interior model, which relies on the EoSs of its various components, can be used to infer from its observed properties various aspects of planet composition such as water content (e.g. Unterborn et al. 2018) and atmosphere mass (Armstrong et al. 2020). However, Hakim et al. (2018) showed that the modelling uncertainty that arises from different EoSs of iron are larger than the observational uncertainties for the best-observed super-Earths. Thus, improved EoS measurements of key planet-building materials are essential for understanding the nature of observed exoplanets. For H<sub>2</sub>O specifically, many experimental and theoretical studies of the EoS across phase space (e.g. French et al. (2009); Mazevet et al. (2019); Journaux et al. (2020)) were recently compiled in Haldemann et al. (2020).

In Huang et al. (2021), we (Huang, C., myself [second author], Grande, Z. M., Smith, D., Smith, J. S., Boisvert, J. H., Tschauner, O., Salamat, A., and Steffen, J. H) implement into MAGRATHEA the new high-pressure ice EoS measurement from Grande et al. (2022) and show the interior structure of water-rich planets based upon our model. We compare the room temperature experimental high-pressure ice EoS results from Grande et al. (2022) (EOS I), to the spliced ice EoS from Zeng et al. (2016) (EOS II), and the room temperature ice EoS measured by Frank et al.

Table 4.1: Frank et al. (2004) and Grande et al. (2022) best fit EoS parameters. The Zeng et al. (2016) paper uses a different parameterization for their EoS (see Zeng & Sasselov 2013).

Phase	Transition pressure (GPa)	$V_0$ (cm <sup>3</sup> /mol)	$K_0$ (GPa)	$K'_0$
Frank	N/A	12.4(0.1)	21.1(1.3)	4.4(0.1)
ice-VII	N/A	12.80(0.26)	18.47(4.0)	2.51(1.51)
ice-VII <sub>t</sub>	5.10(0.5)	12.38(0.16)	20.76(2.46)	4.49(0.35)
ice-X	30.9(2.9)	10.18(0.13)	50.52(4.16)	4.5(0.15)

(2004) (EOS III). The fitting parameters for the room temperature EoSs are listed in Table 2.3. We clarify that Frank et al. (2004) did not identify the transitions to ice-VII<sub>t</sub> or ice-X. Thus, models that use their results are extrapolations to high pressure from the single-phase, ice-VII EoS. We treat the hydrosphere as isothermal in this work as the thermal expansivity of high-pressure ice has large uncertainties. Here, I recapitulate the interior modelling which I was the primary author of in Huang et al. (2018).

We consider an unlikely water and atmosphere model to demonstrate the impact of the EoS on inferences of minimum atmosphere mass. K2-18 b has a mass of  $8.63 \pm 1.35 M_{\oplus}$  (Cloutier et al. 2018), a radius of  $2.61 \pm 0.087 R_{\oplus}$ , and confirmed water vapor in its atmosphere (Benneke et al. 2019). The planet is in the habitable zone with an equilibrium temperature near 255 K. Madhusudhan et al. (2020) exhaustively models K2-18 b. However, here we opt to use a two layer model of pure water and an ideal gas to find the absolute minimum amount of atmosphere needed to match observations. We use MAGRATHEA with an outer temperature of 255 K. The ideal gas atmosphere has a molecular weight of 3.0 g/mol and an adiabatic temperature gradient. We model planets with varying atmosphere fractions with total mass ranging from  $\pm 3\sigma$  of K2-18 b’s observed mass at half integer steps. In Fig. 4.2, we show the fraction of mass needed in the atmosphere to reproduce the observed radius of the planet assuming a fully opaque atmosphere. The simulated

radii of the planets with atmosphere mass fractions greater than  $10^{-6}$  are all within 0.1% of the planet's observed radius and its  $\pm 1\sigma$  uncertainties.

As seen on Fig. 4.2, for EOS I from Grande et al. (2022) K2-18 b would need a minimum H/He ideal gas mass fraction of  $6.98 \times 10^{-4}$  to reproduce its observed mean radius within 0.002%. EOS I requires 6.9 times more atmosphere by mass than EOS II (Zeng et al. 2016) in order for the planet to have a radius of  $2.61 R_{\oplus}$ , and it requires 7.2 times less mass than EOS III (Frank et al. 2004) at a mass of  $8.63 M_{\oplus}$  for the same result. The difference in inferred atmosphere fraction between the EoSs increases with observed mass.

These calculations, using the new EoS measurements for water show that ongoing improvements in exoplanet mass and radius measurements require similar improvements in the EoS measurements of planetary materials. At this time, the observational uncertainty of planet mass and radius measurements is comparable to the variation of the modelled planet radii that comes from a lack of consensus in measured EoSs. Our ability to model the interior planet structure will be increasingly limited by our knowledge of the properties of the planetary material under high-pressure and high-temperature conditions.

### 4.3 Core Iron EoS

While most high-pressure experimental techniques reach several hundred gigapascals. Ramp compression can reach over a terapascal which is the central pressure of a  $2.4 M_{\oplus}$ , Earth-like planet. While we were first developing MAGRATHEA we defaulted for our iron core to an hcp-iron EoS from Bouchet et al. (2013) who used ab initio molecular dynamics simulations. In our efforts to use the most up-to-date experimental results we now default to the hcp-iron measured with ramp



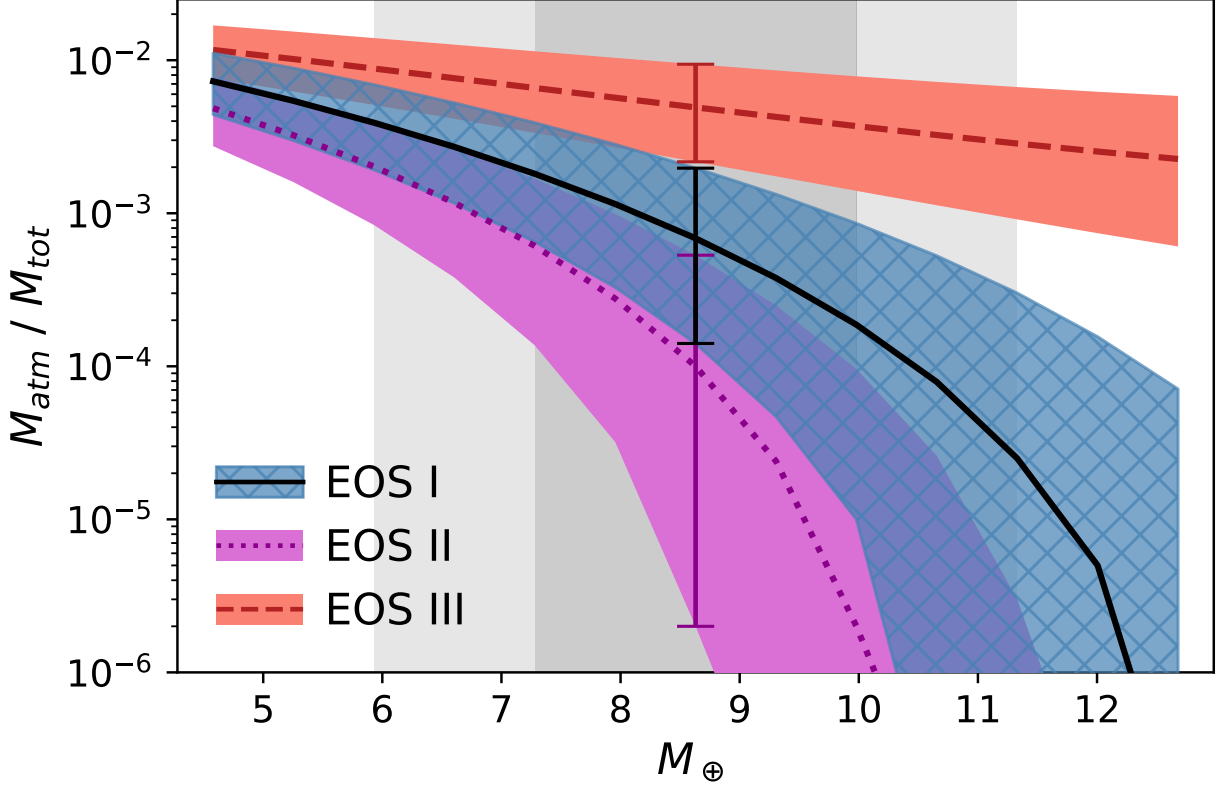


Figure 4.2: Impact of ice EoS measurements on inferences of minimum atmospheric weight for K2-18b. The three EoS shown are EOS I: Grande et al. (2022), EOS II: Zeng et al. (2016), EOS III: Frank et al. (2004). Lines show the fraction of planet mass in an atmosphere needed to reproduce the radius of K2-18b across a range of likely masses. Planets are modeled as pure water with a 3.0 g/mol ideal gas atmosphere and a equilibrium temperature of 255 K. The grey areas show the one and two sigma mass bounds of K2-18b. Planets with varying atmosphere are run at each half step in sigma. The shaded regions show the atmosphere needed to reproduce the radius of K2-18b to within one sigma for each EoS. One error bar is shown at  $8.63 M_{\oplus}$ . Planet parameters from Benneke et al. (2019).

compression in Smith et al. (2018).

In Smith et al. (2018), they use a sound-speed analysis to determine the pressure, density, and sound speed along a continuous isentropic compression path. They use a Vinet fit (Vinet et al. 1987, Eq. 2.9) to describe the compression and report the reference density ( $\rho_0 = 9.43 \text{ g cm}^{-3}$ ), the bulk modulus ( $K_0 = 177.7 \text{ GPa}$ ), and the derivative of the bulk modulus ( $K'_0 = 5.64$ ). These values are in good agreement with Stixrude (2012), but the bulk modulus is 30% lower than in the Holzapfel fit (Eq. 2.10) from Bouchet et al. (2013). In Fig. 4.3, I show Trappist-1 f needs 1.25% less water mass with bulk modulus from Smith et al. (2018) compared to Bouchet et al. (2013).

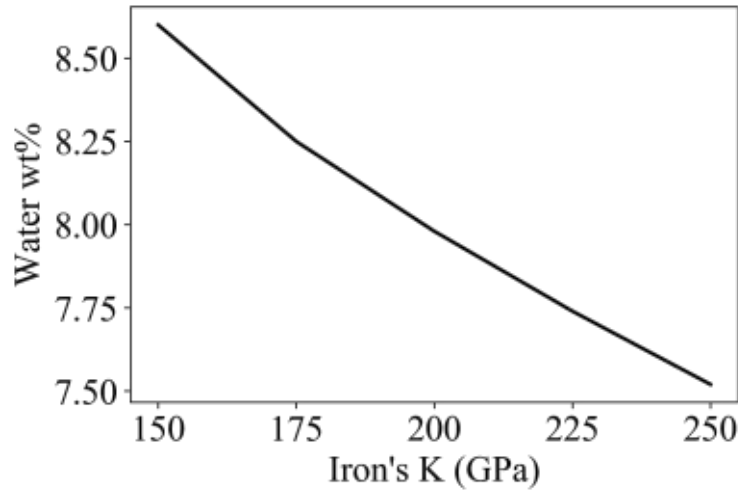


Figure 4.3: Impact of iron's bulk modulus on the inferred water mass fraction of Trappist-1 f at median value of mass and radius assuming an earth like core to mantle ratio. The lower bulk modulus of Smith et al. (2018) leads to the planet needing more water to match observed characteristics. Planet parameters from Agol et al. (2021).

While Smith et al. (2018) reports the non-thermal EoS parameters they do not report a fitting formula for the Grüneisen parameter which describes how a material's volume changes with

temperature:

$$\gamma = \left( \frac{\partial \ln T}{\partial \ln V} \right)_S. \quad (4.1)$$

By comparing the compression of iron along an isentrope and Hugoniot curves, they report the Grüneisen parameter's relation with density in their Fig. 2b and show agreement with Murphy et al. (2011).

I fit this data to the empirical formula in Al'Tshuler et al. (1987) also used in Belonoshko et al. (2008) shown in Eq. 2.13. The Grüneisen and associated error is measured from a density of  $10.783 \text{ g cm}^{-3}$  to  $20.0 \text{ g cm}^{-3}$ . I use EMCEE (Foreman-Mackey et al. 2013) and SCIPY.OPTIMIZE to find the optimal values of  $\gamma_0$ ,  $\gamma_\infty$ , and  $\beta$ . I require  $\gamma_\infty > 0$  and find  $\gamma_0 = 2.09$ ,  $\gamma_\infty = 0.05$ , and  $\beta = 1.01$  with fit shown in Fig. 4.4. At the Earth's central density of  $15 \text{ g cm}^{-3}$ , the Grüneisen from my fit is 1.19 in agreement with the theoretical predictions of Bouchet et al. (2013). I then implement this EoS with thermal parameters as our default core equation in MAGRATHEA.

#### 4.4 FCC and BCC Iron

I worked with two undergraduates as part of the Graduate College Rebel Research and Mentorship Program to add detail to the core and mantle layer in MAGRATHEA. Tristan Benally worked with me on adding core materials in this section. Rosalie Chaleunsouck worked with me to add mantle materials in the next section, Sect. 4.5. We then tested how these changes impact the radius of a given mass planet. The figures in these sections are created by the mentees.

Some planets and smaller bodies may have a large portion of their mass in iron through collisional erosion (Marcus et al. 2009) or material sorting within the protoplanetary disk (Johansen & Dorn 2022). Mercury has 70% of its mass in an iron core (Hauck et al. 2013) and a number of

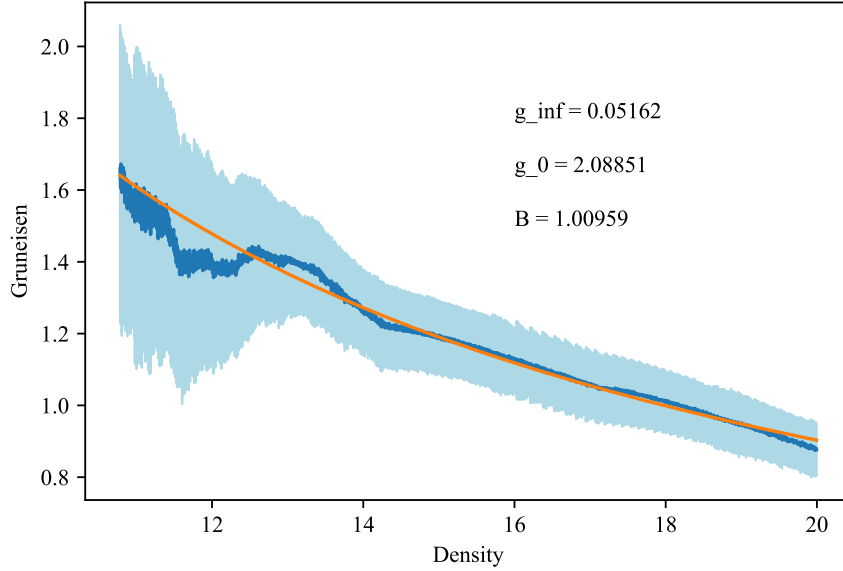


Figure 4.4: Grüneisen parameter as a function of density, *blue*, with error, *light blue*, from Fig. 2b in Smith et al. (2018). Relationship with best fit parameters for Eq. 2.13 shown in *orange*.

exoplanets are consistent with Mercury-like interiors (e.g. Rodríguez Martínez et al. 2023). KOI 1843.03 specifically is shown to have 66% of its mass in iron from its observed tidal-distortion (Price & Rogers 2020).

For these majority iron planets the assumption that the iron is a high-pressure state of hexagonal closed-packed (hcp,  $\epsilon$ ) iron needs to be considered. At lower pressures, iron takes a crystal structure of face-centered-cubic (fcc,  $\gamma$ ) and body-centered-cubic (bcc,  $\alpha$ ). There is a triple-point between these three phases at 7.3 GPa and 820 K (Dorogokupets et al. 2017). At higher temperature and pressure relevant to planet interiors, there is a triple-point between hcp, fcc, and liquid at 98.5 GPa and 3712 K (Anzellini et al. 2013). No previous planet interior solvers used for exoplanets has incorporated these lower-pressure phases.

We include in MAGRATHEA the parameters for a third-order Birch-Murnaghan equation of state and thermal parameters for fcc- and bcc-iron from Dorogokupets et al. (2017). Each responds

to pressure and temperature uniquely. The bulk modulus of bcc-Fe for example is 10% larger than that of hcp-Fe. We include phase-transitions between these three materials and liquid iron from the measurements of Anzellini et al. (2013) measured in a laser-heated diamond anvil cell.

In Fig. 4.5, we show how including all phases of iron impact the mass-radius relationship of planets. The radius of cold, pure iron planets with fcc- and bcc-Fe is less than 0.25% different from pure hcp-Fe planets for Earth-mass planets, but the difference increases for small masses. However, at higher temperatures fcc-Fe is more important to include in structure models. While hcp-Fe exists at just 7 GPa at low temperatures ( $<800$  K), at 2000 K fcc-Fe is stable up to 50 GPa before transitioning into hcp-Fe. Thus, in Fig. 4.5, pure-iron planets half the mass of Earth have radii over 1% difference when starting the adiabatic temperature gradient at 1750 K. All of the planets shown remain in the solid phase without transitioning to liquid iron.

We show that including fcc- and bcc-iron has little effect on the radius of a given mass of planet. Of larger concern to bulk planet properties is the melting temperature of iron which needs further measurement at high pressures and the equation of state of non-pure iron.

#### 4.5 Upper Mantle Materials

In MAGRATHEA presented in Ch. 2, we made an assumption that the mantle was pure  $\text{MgSiO}_3$  in the bridgmanite and post-perovskite phases (high-pressure forms of enstatite). These two high-pressure forms of magnesium silicate make up 50% of Earth's mass (74% of the mantle's mass) and 57% of the Earth's volume. Unterborn & Panero (2019) fully model planet mantles by coupling an interior solver to PerPlex Connolly (2009) which finds the percentages of stable mantle minerals at all depths and use EoSs from Stixrude (2012). They show this detailed modelling only changes

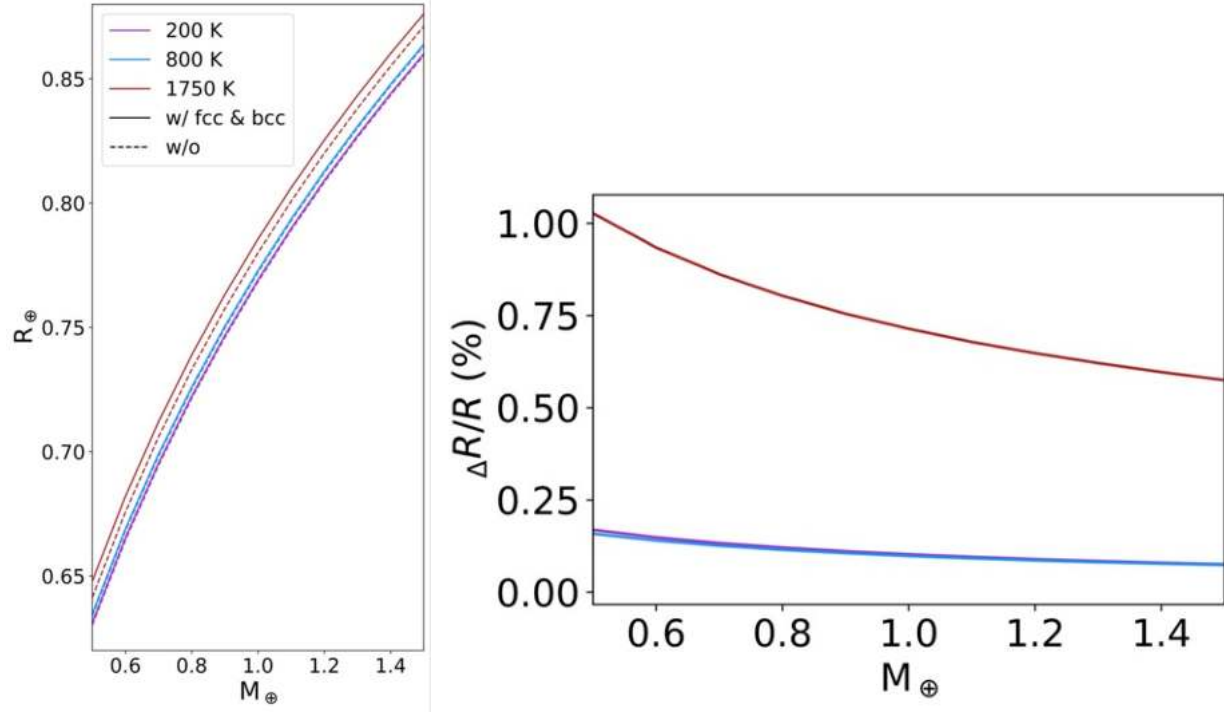


Figure 4.5: *Left*, this graph shows a mass-radius plot with comparison between planets with low pressure iron and without and with different surface temperatures. *Right*, this graph shows the percent difference between the planets with low pressure iron and without.

planet radii on order of 1% and to run solve interiors quickly Unterborn & Panero (2019) relies on large tabulated EoS for the specific mantle mixture found with the stable mineral solver.

We aim to bridge our simplified assumption and an expensive, detailed model of the mantle, by adding newer EoSs for upper-mantle magnesium silicates to our interior model. Here, we add forsterite, wadsleyite, and ringwoodite all polymorphic forms of  $\text{Mg}_2\text{SiO}_4$  to MAGRATHEA. We include the fitting parameters for a third-order Birch-Murnaghan and thermal parameters from Dorogokupets et al. (2015).

In addition to the phase transitions for melt from Belonoshko et al. (2005b) and post-perovskite from Ono & Oganov (2005), we include the phase transitions for these three new phases determined using Fig. 5. We fit a quadratic relationship to pressure as function of temperature for the

transition to bridgmanite from  $\text{Mg}_2\text{SiO}_4$  and linear functions between the polymorphs of  $\text{Mg}_2\text{SiO}_4$ .

We find bridgmanite occurs at pressures (in GPa) above

$$P > 24.3 - 0.002T - 3 \times 10^{-7}T^2. \quad (4.2)$$

Ringwoodite occurs below the above pressure and above

$$P > 8.69 + 0.006T, \quad (4.3)$$

and wadsleyite occurs below the above pressure and above

$$P > 9.45 + 0.0028T. \quad (4.4)$$

Forsterite, the magnesium end-member of olivine, occurs at lower pressure than above. In Fig. 4.6, we show mantle pressure temperature profiles passing through these phases of magnesium silicates. Starting the mantle adiabat below 2000 K means all 5 phases added to our code are present in the planet. The profile for each planet is slightly different, but indistinguishable from one another in this plot.

We test how these additions to our mantle model affect the mass-radius relationship. We simulate planets from 1-5  $M_\oplus$  with their entire mass in the mantle with our model without the upper mantle phases and with the upper mantle phases. We also compare this to a planet created with the PREM model (Stacey & Davis 2008; Appendix F). PREM is a one dimensional radial model for the average properties of Earth like density and seismic wave velocity by depth and is supported by seismic observations. We extrapolate the relationship to even higher pressures for planets with

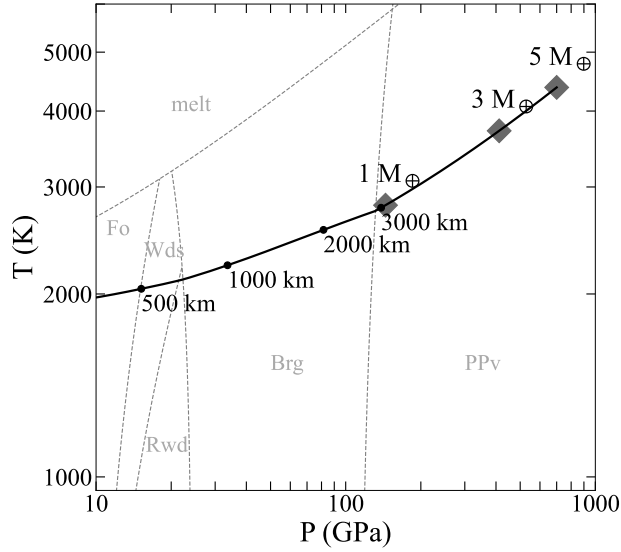


Figure 4.6: A phase diagram showing temperature-pressure profiles for the mantles of three masses of planets with an Earth-like 32.5% of their mass in the core and a mantle adiabat which starts at 2000 K. A diamond marks the central temperature and pressure for each planet mass. The planets pass through many phases of magnesium silicates. Depths shown for the  $1 M_{\oplus}$  Earth-like planet.

larger mantle masses than the Earth.

Our results are shown in Fig. 4.7. Adding an upper mantle creates a 2% difference in radius at one Earth-mass in comparison with our previous model. The new model is in good agreement with the PREM model. The resulting radius is consistent with the PREM model (Stacey & Davis 2008; Appendix F).

The PREM model is less compressible at high pressures, so the radius of planets over one Earth-mass are larger than our models. The difference can be up to 10% for  $5 M_{\oplus}$  planets. However, the upper mantle has less affect compared to our model without an upper mantle. The difference for planets over one Earth-mass remains under 2% and is only 1% for  $5 M_{\oplus}$  planets. This agrees with the findings of Unterborn & Panero (2019), and shows that for bulk planet properties modelling the upper mantle accurately has a 1% difference from simple high-pressure silicate models. In later



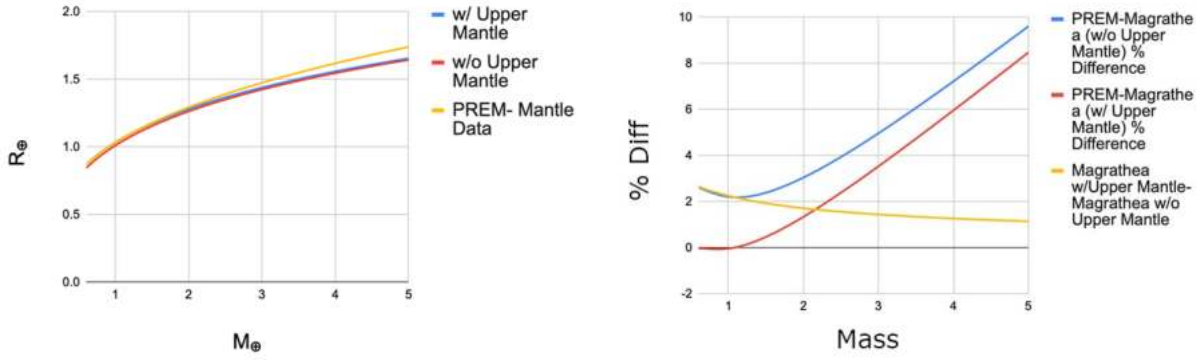


Figure 4.7: *Left*, a comparison of the output radius of the models based on given 100% mantle planetary masses. *Right*, the graph displays the percentage differences between two models given in legend.

chapters, I use this phase diagram as default in MAGRATHEA.

## 4.6 Summary and Future Work

This chapter demonstrates the flexibility of the MAGRATHEA code and tests the effect of equations of state choices and measurements on inferences of planet properties. Our code’s transparent structure allows us to add modern equations of state and improve the accuracy of the interior model in the hydrosphere, mantle, and core.

In Sec. 4.2, we work with high-pressure physicist to measure the elastic properties of Ice VII and Ice X and identify phase transitions and a transitional phase, Ice VII’. We show how this measurement compares with other hydrosphere parameters from previous works and how the uncertainty in planet radii is on the same order as our best exoplanet observations. I also show how K2-13b can be characterized with a new water-ice EoS. Planet characterizations such as this is the focus of Chapter 5.

In Sec. 4.3, I show how I determined the thermal parameters of hcp Iron from Smith et al.

(2018) and the measurements impact on planet properties. We improve our model with more phases of iron and silicates in Sec. 4.4 and Sec. 4.5. These improvements effect planet radii by 1% for certain planet masses and temperatures.

Here, I focus on the elastic and thermal properties affecting the density of a material and thus the bulk radius of a given mass planet. However, material properties also have important implications for other aspects of planet interiors. A planet’s materials determine heat transport and water storage. Both of these properties are essential to the evolution and habitability of small planets. Current studies make a number of simplifying assumptions for a planet’s materials (e.g. Dorn & Lichtenberg 2021; Zhang & Rogers 2023).

As new measurements are made, interior models will need to remain updated to modern measurements. There remains a number of materials and measurements to add to our model and test their effect. Future work includes updating the iron melt curve to Kraus et al. (2022) and major expansion of the library to include the water EoS compilation from Haldemann et al. (2020), supercritical water from Mazevet et al. (2019), and non-ideal gas from Chabrier et al. (2019).

A major update to our model will be including mixtures of materials as a function of depth. This will require additional functions for ideal mixing and user-interfaces to adjust phase diagrams and desired chemical abundances. A few studies simulate multi-component materials by adjusting the density of core or mantle materials while others use ideal mixing of a few components (Plotnykov & Valencia 2020; Unterborn et al. 2023).

This update will increase the accuracy of planet interiors. Essential to improving our mantle assumptions is the FeO abundance of the mantle. The Earth has about 8% weight FeO in the mantle and Mars is likely greater (McDonough 2003). While we assume pure magnesium silicates, iron silicates with the same structure generally have similar elastic properties but larger densities.

Furthermore, when the dominate phase transitions from  $\text{Mg}_2\text{SiO}_4$  to  $\text{MgSiO}_3$  the missing magnesium and oxygen becomes magnesiowustite making up about 20% of the lower mantle by mass. Additionally, there are aluminum and calcium minerals in the mantle that a majority of models ignore.

In the core, most exoplanets works assume pure iron, but the Earth has 5% nickel and 10% light elements by weight (McDonough 2003). These alloys may have different elastic properties (Brennan et al. 2021). In addition, these compositional differences affect melting conditions. Mars's liquid core is a result of sulfur decreasing the melting temperature (Stähler et al. 2021). In Fig. 4.8, I show P-T profiles of the core of planets from Fig. 4.6 for masses of  $1 M_\oplus$ ,  $3 M_\oplus$ , and  $5 M_\oplus$ . I add an Earth-like 1200 K increase in the temperature at the CMB, but all three planets remain in the solid phase if the core is pure iron for the melt curve from Dorogokupets et al. (2017). I also plot a melting curve for a mix of sulfur in the core, Fe-Fe<sub>2</sub>S (Mori et al. 2017). If planets were simulated with this mix, the  $1 M_\oplus$  would be entirely melted. The  $3 M_\oplus$  would have a significant liquid outer core and hence possibly a magnetic field (Lazio et al. 2019).

Yet further still, implementing a robust method for mixtures will empower the next generation of interior models. There are several works interested in mantle hydration affecting bulk planet properties and planet evolution such as Shah et al. (2021); Dorn & Lichtenberg (2021) and the inside of super-earths being even further mixed with hydrogen and water Vazan et al. (2022). Planets formed in water-rich environments with large primary atmospheres may evolve and have large difference in interiors from our Earth-based assumptions. These are exciting future directions for study.

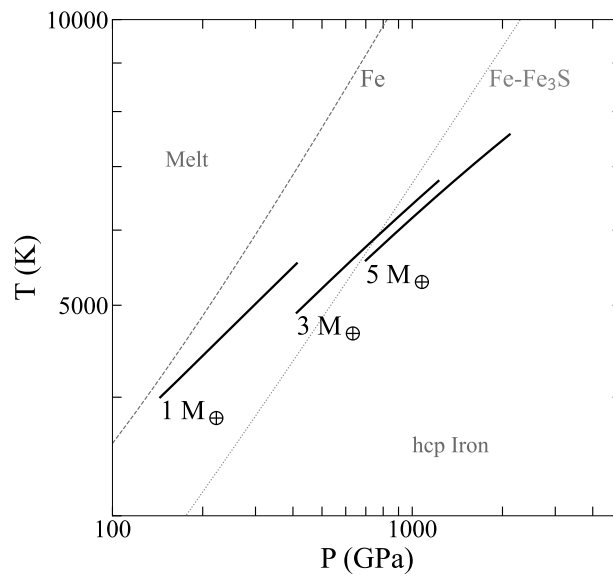


Figure 4.8: A phase diagram showing temperature-pressure profiles for the cores of planets from Fig. 4.6. Planets are simulated with a 1200 K increase in temperature at the CMB. All three cores are pure hcp Iron, but the melt curve for a iron sulfur mix is also plotted.

## Chapter 5

### Characterizing the Composition of Planets

#### 5.1 Background

While in Chapters 2, 3, and 4 I improved interior models for small planets, I use these models in the next two chapters to assess the composition of observed planets. Demographic studies of composition will improve our insights into the exoplanet population. In addition these studies communicate improved interior models to the wider exoplanet community. Studies are motivated by the increasing number of precise measurements. NASA’s TESS which has identified over 1000 candidate planets less than  $4 R_{\oplus}$ . Follow-up extreme precision radial velocity measurements, an ongoing initiative by NASA/NSF, will measure masses for these small planets. Furthermore, Tsai et al. (2021) shows measurements of the abundance of trace gasses by the James Webb Space Telescope can be used to constrain ocean depths and day-to-night side temperature contrast constrain atmospheric circulation and thus atmosphere masses (Koll et al. 2019).

Most observational studies which determine or refine the masses of small planets will include a section describing the planets’ possible compositions. If we just look at the most recent analyses, we see some are based solely on comparisons to mass-radius models: Winters et al. (2022); Serrano et al. (2022) use models of Zeng et al. (2016), Chaturvedi et al. (2022); Beard et al. (2022); Kemmer et al. (2022) use the updated Zeng et al. (2019), and Luque et al. (2022) uses Turbet et al. (2020). While others use interior models to give further constraints on possible compositions:

Barros et al. (2022) uses an improved model based on Dorn et al. (2017b), Cadieux et al. (2022) uses Plotnikov & Valencia (2020) with an added water layer, and Essack et al. (2023) use their own model.

Described in Sect. 3.2, I built a composition finder into MAGRATHEA which takes the mass and radius of a planet and finds the water mass fraction at a given refractory core-mass-fraction ( $r\text{-cmf}$ ).  $R\text{-cmf}$  is the ratio of the cmf to the total core and mantle mass and provides a uniform parameter space for characterizing. This method can be adapted to constrain the atmosphere mass fraction. I aim for these methods to become standards in observational studies.

In this chapter, I show how I characterize bulk composition of observed planets. In Sec. 5.2, I reference my collaborative work, MacDonald et al. (2022), in which I characterize the compositions of the planets in the K2-138 system. In Sec. 5.3, I analyze the compositions of planet's which may be water worlds from Luque & Pallé (2022). In Sec. 5.4, I describe a submitted collaborative work which constrains the possible compositions of the TRAPPIST-1 planetary system from their formation by tracking condensation in the disk and dynamical evolution. I model the planets interiors from compositional constraints from formation. I end with some summarizing remarks in Sec. 5.5.

## 5.2 K2-138 Planetary System

While most mass and radius constraints for planets come from observations such as stellar radial velocity (Mayor & Queloz 1995) and planetary transits (Struve 1952; Henry et al. 2000; Charbonneau et al. 2000), the masses found for planets in a multiple planet system may be further constrained from dynamics. In a multiple planet system, mutual perturbations from the planets

lead to instabilities which then lead to planetary collisions or ejections on timescales which may be shorter than the age of the system. I explore these timescales in multiple planet systems in my earlier work in Rice et al. (2018) and Rice & Steffen (2023). For closely-packed planetary systems, the planets often need to be in resonance in order to survive long timescales. Resonances are suggested to be present in Kepler-223 Mills et al. (2016), Kepler-80 MacDonald et al. (2016), and TRAPPIST-1 Luger et al. (2017). These resonances are sensitive to planetary parameters.

In MacDonald et al. (2022), collaborators (Dr. Mariah MacDonald, Leonard Feil, and Dr. Tyler Quinn) use N-body simulations to explore the probability that K2-138’s five planets are in resonance, and I (fourth author) constrain the planet’s compositions. Most simulations result in 3:2 resonances between the planets with 11% having all 5 planets in a resonance chain. Such resonant chains are sensitive to formation scenarios. However, we find the system can be formed through long-scale migration (Cossou et al. 2013) or in situ through short-scale migration or eccentricity damping (MacDonald & Dawson 2018).

The compositions of planets can also be used to constrain the formation and evolution of a system. As a first-order approximation of the compositions of K2-138’s planets, we first explore the planet’s bulk densities, comparing them to Earth-like and less dense compositions. We draw 1000 pairs of mass and radius estimates for the confirmed planets from normal distributions of the parameters in Lopez et al. (2019), while obeying the 99% credibility intervals of density. In Figure 4, we plot 200 of these samples with mass-radius curves for compositions of pure water, Earth-like, and 1% H/He envelopes. We see that K2-138b is consistent with a terrestrial composition while K2-138c, K2-138d, and K2-138e are less dense and require large volatile layers. K2-138f also has a low density, below  $2.068 \text{ g cm}^{-3}$ , and most likely requires the largest atmosphere envelope.

We model the interiors of the four inner planets using the planet structure code MAGRATHEA.

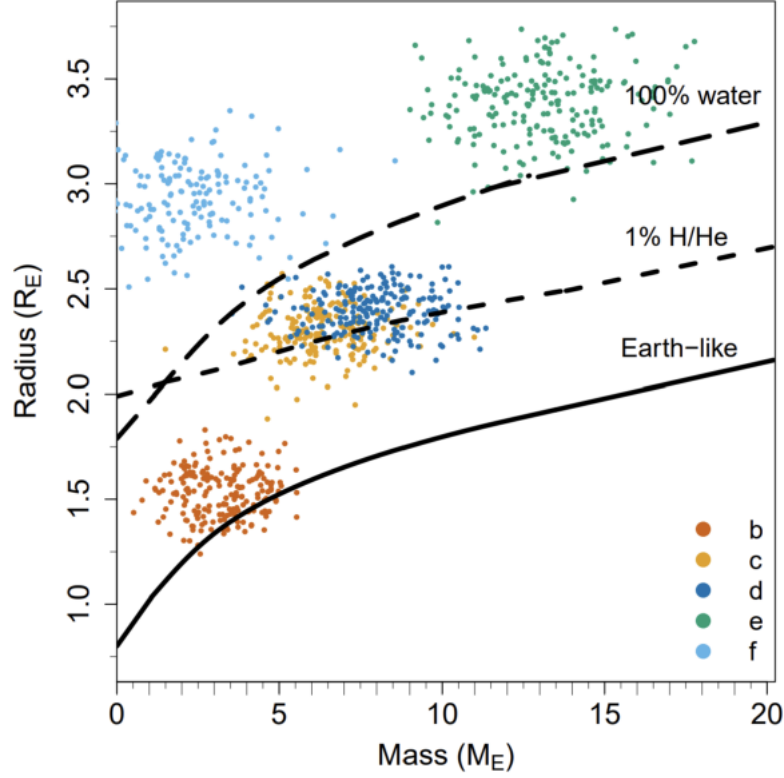


Figure 5.1: Mass-radius diagram with the radius and mass estimates of K2-138’s planets. These estimates were pulled from normal distributions centered on the values from Lopez et al. (2019), with standard deviations equal to the uncertainties. We overplot composition curves of Earth-like (solid), 1% H/He atmosphere (short dash), and 100% water (long dash). We find that K2-138b is consistent with an Earth-like and terrestrial compositions, but that planets c-f require at least 1% H/He envelopes to satisfy their densities.



The code takes as input the mass in each differentiated layer of a spherically symmetric planet and solves in 1-D the pressure, density, temperature, and radius at enclosed mass using a shooting method. We use MAGRATHEA’s default model and a surface pressure of 100 mbar. The default model uses equations of state for solid hcp and liquid iron in the core, bridgmanite and post-perovskite silicate in the mantle, and water, ice-VII, ice-VII’, and ice-X in the hydrosphere (Smith et al. 2018; Dorogokupets et al. 2017; Oganov & Ono 2004; Sakai et al. 2016; Grande et al. 2022). The atmosphere is ideal gas with a mean molecular weight of  $3 \text{ g cm}^{-3}$  similar to a hydrogen-helium mixture.

Models such as ours are inherently limited for large, hot planets with interior conditions beyond our experimentally-determined equations of state. Additionally, Neptune-like planets may have diffuse interfaces between layers and exotic mixtures of elements. To decrease degeneracies, we separate our water and atmosphere analyses. For our water analysis, we limit the hydrosphere to liquid and ice phases, although equilibrium temperatures for the planets would suggest a vapor layer. The planets are given an isentropic temperature profile with a surface temperature of 300 K. For the atmosphere analysis, we use an ideal gas and an isentropic temperature profile with surface temperatures set equal to the equilibrium temperatures: 1308, 1140, 992, and 861 K (Lopez et al. 2019). A real gas would require less atmosphere mass, while a less steep temperature profile would require more. Our models, although limited, are efficient and give us an understanding of the range of possible interior solutions.

We investigate the potential water mass fraction (wmf) in Figure 5.2 and the potential atmosphere mass fraction (amf) in Figure 5.3. For each of the 1000 samples of mass and radius, we vary the mass percentage in each layer until the radius matches the sample to 0.01%. A secant method is used to find the wmf or amf needed to match the radius. We find the wmf uniformly across core

mass fraction while keeping the core to mantle ratio constant. Explained graphically, in Figure 5.2 we find the wmf on diagonal lines such as the Earth-like 33% core to 67% mantle line. The AMF is found uniformly across wmf with the remaining mass divided 33% and 67% into the core and mantle respectfully.

Figure 5.2 shows that K2-138b most likely has a wmf from 9.0 to 47% depending on the core to mantle ratio. If K2-138b has an Earth-like core to mantle ratio our estimated water fraction is  $24.3^{+39.0}_{-22.0}\%$ . 32% of samples have hydrosphere-free solutions requiring only core and mantle. A small number of samples of K2-138c and K2-138d have hydrosphere solutions without an atmosphere. With Earth-like core to mantle, 18.3% of K2-138c and 25.5% of K2-138d samples have solutions with less than 90% wmf. For reference, models of Neptune suggest upwards of 80% mass in a water-dominated fluid layer (Scheibe et al. 2019).

Figure 5.3 shows the amf needed to match samples of the planets' masses and radii across wmf. Listed are the predicted amf of the isentropic model across all wmf: K2-138b  $17^{+93}_{-9.0} \times 10^{-4}\%$ , K2-138c  $5.3^{+7.9}_{-3.8} \times 10^{-4}\%$ , K2-138d  $7.0^{+13}_{-5.6} \times 10^{-4}\%$ , K2-138e  $220^{+160}_{-110} \times 10^{-4}\%$ . With zero wmf, K2-138c and d need an amf of over 0.001%. The pressure and temperature under the atmosphere of K2-138c with 50% wmf is around 10 bar and 4000 K which in our model creates a small layer of liquid water before transitioning to high-pressure ices. This temperature and pressure suggests the water should still be in a vapor phase, but a coupled atmosphere-interior model would need to be used to understand this boundary. K2-138e requires an amf around 15-30 times more than K2-138c and d at zero wmf. Additionally, K2-138b's mass and radius could be explained with a hot, inflated H/He atmosphere layer, but many solutions require atmosphere masses less than  $10^{-6} M_{\oplus}$ .

Besides K2-138c and d which have similar inferred compositions, the possible compositions

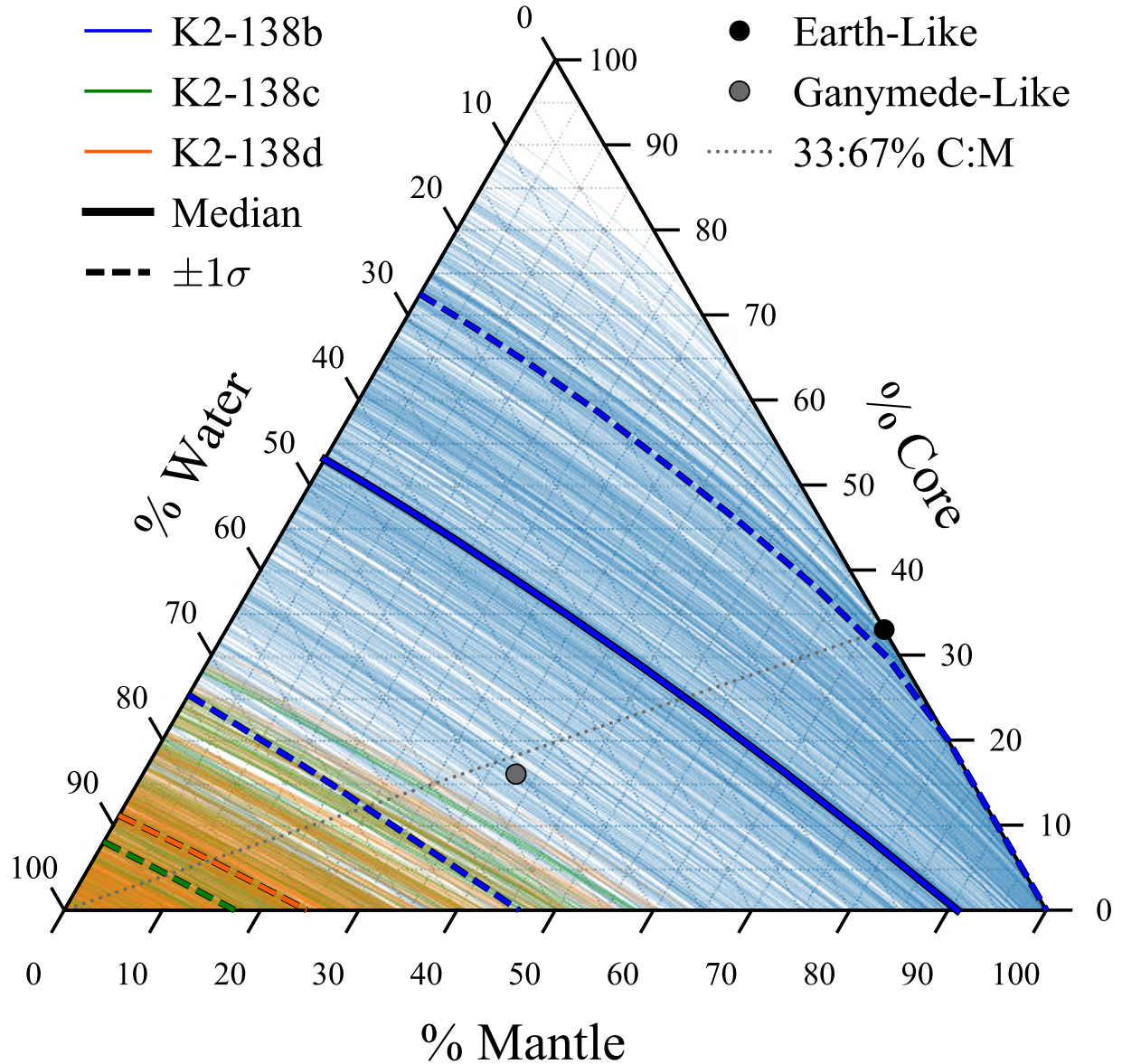


Figure 5.2: Ternary diagram where the axes are the percentage of mass in a core, mantle, and hydrosphere. Background thin lines are solutions from MAGRATHEA to 1000 samples of each planet’s observed mass and radius. The wmf needed to match the observed radius is found across core:mantle ratio. Large solid lines of the corresponding planet color is the median wmf while dashed lines are the  $1\sigma$  bounds. K2-138b (*blue*) is the only planet where all 1000 samples have non-atmosphere solutions. The median sample of K2-138c (*green*) and d (*orange*) require an atmosphere and only the  $-1\sigma$  bound of wmf is shown. Grey dashed line shows a constant Earth-like core to mantle ratio.

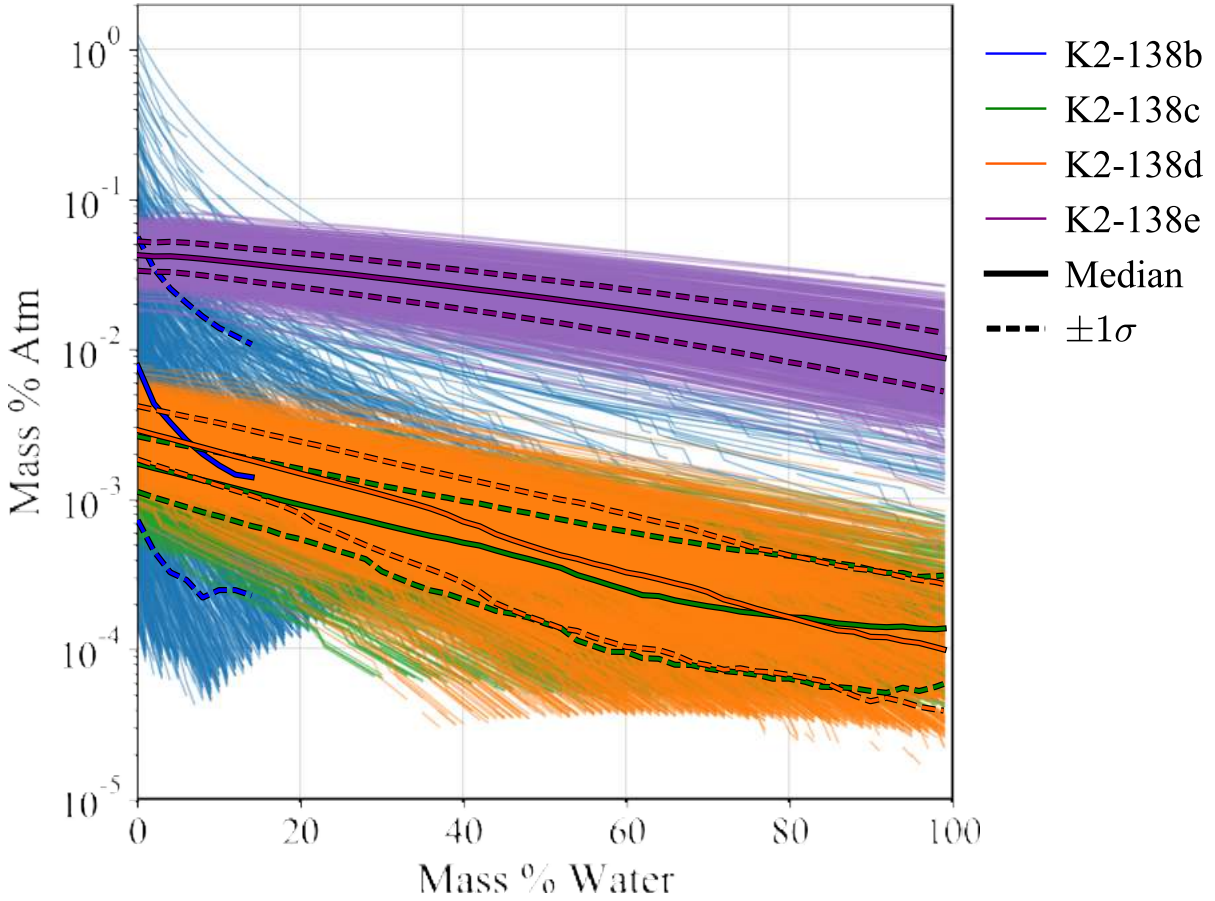


Figure 5.3: The water and atmosphere mass needed to match 100 and 1000 observed samples of mass and radius. The remaining mass is split 33:67 into the core and mantle. Thin background lines are solutions to each sample. Solid thick lines are the mean and  $1\sigma$  bounds of samples with solutions at the given water mass. An isentropic temperature profile is used with the surface temperature set to the equilibrium temperature from Lopez et al. (2019). The statistics for K2-138b are only calculated up to when half of the samples have solutions requiring more than  $10^{-4}\%$  atmosphere mass. 186 samples of K2-138b are too dense to require an atmosphere mass of more than  $10^{-4}\%$ .

of K2-138b through e have little overlap. Their densities decrease and inferred volatile content increases with increasing orbital distance. Other systems with resonances such as TRAPPIST-1, have planets with similar densities and inferred compositions (Agol et al. 2021).

In summary, using the planet structure code MAGRATHEA, we explore the potential compositions of the planets in K2-138 along the uncertainties in their masses and radii. We find that K2-138b is consistent with a terrestrial composition and that any atmosphere would be less than half the mass of Venus’s atmosphere. K2-138c and K2-138d have similar compositions; both planets require a minimum of  $\sim 80\%$  of their mass to be water, or an atmosphere, with over  $0.01\%$  of their mass as atmospheres. The bulk density of K2-138e is inconsistent with a non-atmospheric model; without a hydrosphere, we estimate an atmospheric mass fraction of  $0.5\%$ , or  $0.065 M_{\oplus}$ .

### 5.3 Water Worlds and Super Earths

An alternative explanation to the radius gap introduced in Sect. 1.1 argues that the radius gap between the two populations is from water worlds and rocky worlds (Zeng et al. 2019). Forward models of planet formation predict an abundance of planets that formed beyond the snowline with a large water mass fraction (wmf) and then migrated inward (Raymond et al. 2018; Emsenhuber et al. 2021). In the Solar System, the icy-moons of the giant planets have over  $50\%$  of their mass in a water-ice hydrosphere. Water-worlds or super-Ganymedes would be an exciting laboratory for habitability (Kite & Ford 2018). However, the abundance of observed “water worlds” is yet to be determined.

Luque & Pallé (2022) find a sample of small planets whose masses and radii can be explained by ones with Earth-like interiors and ones with  $50\%$  wmf. They compile a sample of 34 transiting

planets smaller than 4 Earth radii around M-dwarf stars with radius precision under 8% and mass precision under 25%. These planets are in fewer than 26 planetary systems. For 9 planets, they improved mass and/or radius measurements with new observations and joint analyses.

The evidence presented in Luque & Pallé (2022) for these planet’s compositions is a plot of mass and radius with lines of constant interior structure implying that the planets near them have similar interior structures (similar to Fig. 5.5). They find 21 planets match a Earth-like composition, 5 planets are matched by a 50% H<sub>2</sub>O line, and the remaining 7 are over 5 M<sub>⊕</sub> and require some atmosphere. However, lines of composition on a mass-radius diagram are not unique. The sample of water-rich worlds would be much more significant if all three-layer interior structures were found for the planets across uniform r-cmf.

I investigate the nine planets reanalyzed in Luque & Pallé (2022). I draw 200 samples of mass and radius from Gaussian fits to the median and  $\pm 1\sigma$  reported values in Luque & Pallé (2022)(supplementary materials) for LTT-3780b and c, TOI-1634b, TOI-1685b, L 98-59c and d, LHS-1815b, TOI-1235b, and GJ 1252b. I find the water mass fraction of each planet at r-cmf values from 0 to 1 (inclusive) at steps of 0.02. Further details on the finder in Sect. 3.2. Radii are matched to an error of 0.001%. I use a simple prescription of temperature here by treating all planets equally with surface temperatures of 300 K meaning all planets outer layers are water. I plan to improve this prescription in the future. For each planet there is up to 83,000 interior structures that match the 200 draws of observed masses and radii. For example, I show the solutions on a ternary diagram of GJ 1252b in Fig. 5.4.

From the 200 draws of mass and radius, I calculate the median and  $\pm 1\sigma$  bulk density. I summarize all the interior structures found by the composition finder into an “uncompressed density” which roughly estimates the planet’s density if the interior was not under compression. In other

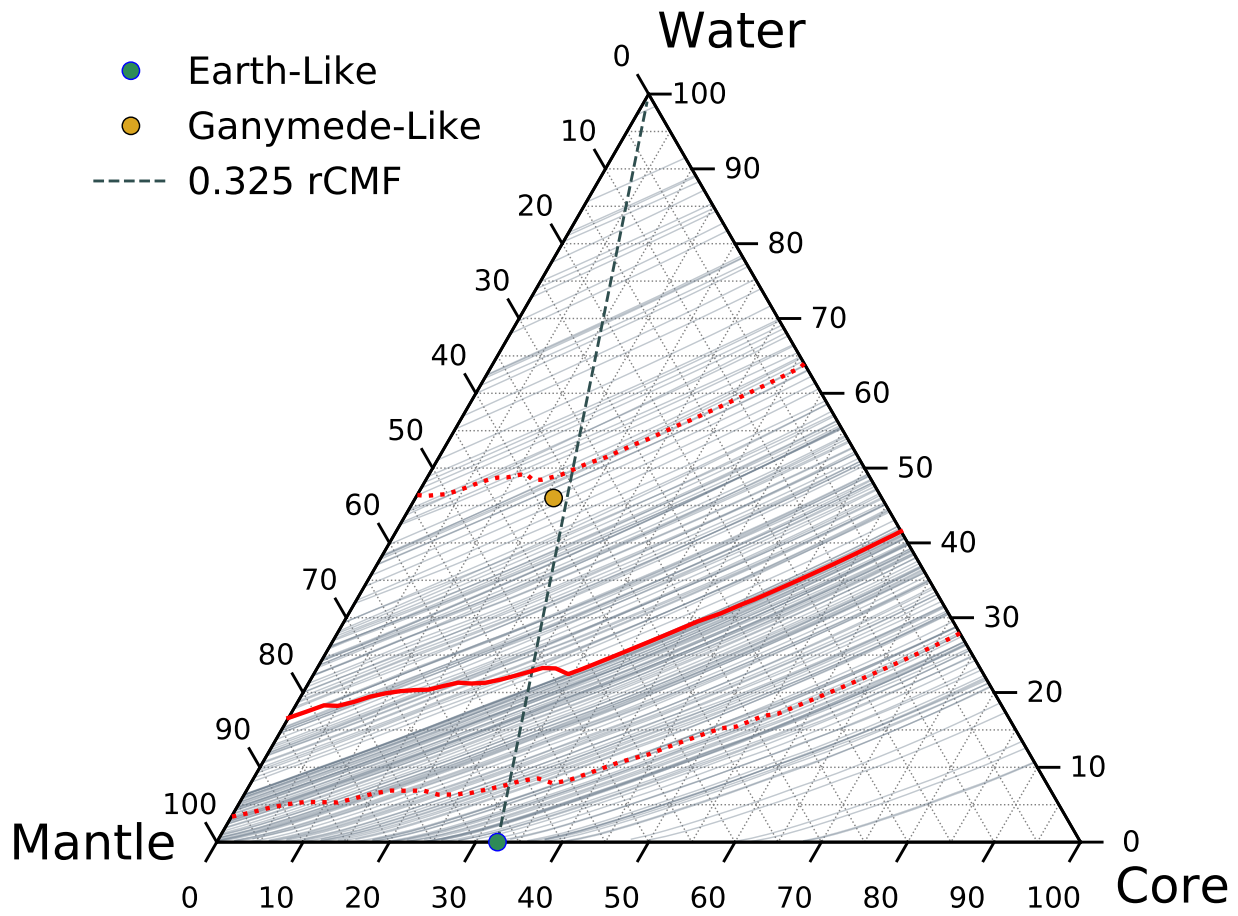


Figure 5.4: Water-Mantle-Core mass ternary diagram with interior solutions to GJ 1252b from mass and radius in Luque & Pallé (2022). *Red*, shows the median and 1- $\sigma$  bounds of valid solutions. The most-probable water mass fraction is below 50% for all r-cmf.

words if all of the material was at standard temperature and pressure. The uncompressed density,  $\rho_u$  is given by

$$\rho_u = \frac{\rho_c \rho_m \rho_w}{f_c \rho_m \rho_w + f_m \rho_c \rho_w + f_w \rho_c \rho_m} \quad (5.1)$$

where the mass fraction of each of the three layers is  $f_c$  for core,  $f_m$  for mantle, and  $f_w$  for hydrosphere and the each layers uncompressed density is defined as  $\rho_c = 7.8 \text{ g cm}^{-3}$ ,  $\rho_m = 3.2 \text{ g cm}^{-3}$ , and  $\rho_w = 1.0 \text{ g cm}^{-3}$ . To illustrate this quantity consider that the interior of Mercury is less compressed than Earth's since Mercury's mass is 5.5% that of Earth. Thus Mercury has a slightly lower density than Earth ( $\rho_{B,Mercury} = 0.98 \rho_{B,Earth}$ ), but its uncompressed density is much higher because of its large iron core ( $\rho_{u,Earth} = 3.96 \text{ g cm}^{-3}$ ,  $\rho_{u,Mercury} = 5.45 \text{ g cm}^{-3}$ ).

In Fig. 5.5, I show the 9 planets along with Trappist-1f and a few Solar System bodies on a mass-radius diagram and their uncompressed density versus bulk density. While the planets only appear slightly above the Earth-like line of mass-radius, the median values uncompressed density for all 9 planets, besides LHS-1815b, fall below that of pure rock.

Luque & Pallé (2022) claim a significant separation in bulk density in their full set of planets. However, we find no significant bi-modality in the bulk density of these 9 planets. We perform a Hartigan Dip-test of Unimodality on the one dimensional uncompressed density data for all 9 planets (Maurus & Plant 2016). We pick up a peak in uncompressed density for Earth-like planets separated from water worlds with a significance level of 0.3%.

Critical to the separation is GJ 1252b which was first discovered by Shporer et al. (2020). Luque & Pallé (2022) analyzes additional HARPS radial velocity data (Mayor et al. 2003) for the planet and found a  $1\sigma$  lower mass from  $2.09 \pm 0.56$  (Shporer et al. 2020) to  $1.32 \pm 0.28 M_{\oplus}$ . This new mass is in agreement with Crossfield et al. (2022) who also found a slightly lower radius



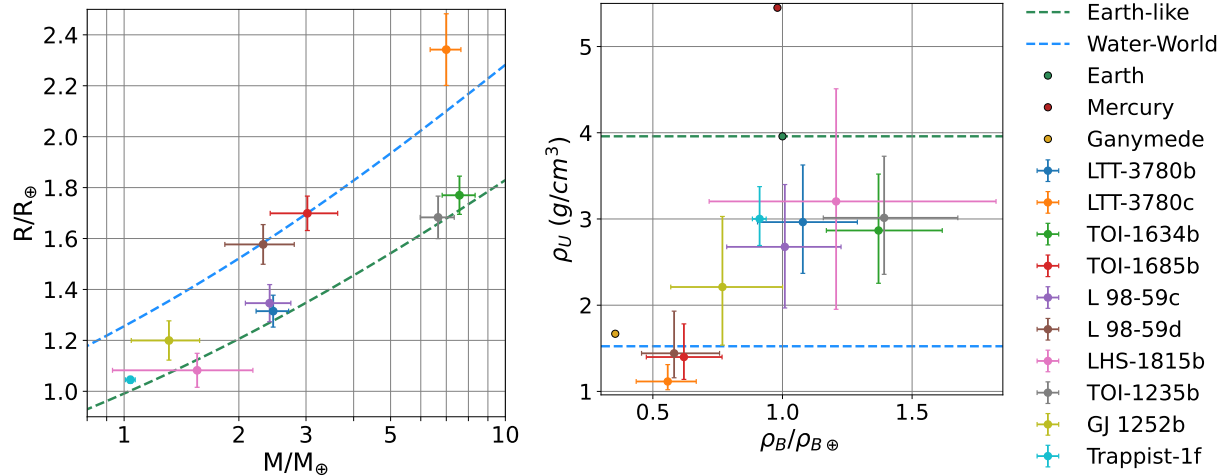


Figure 5.5: *Left*, nine planets reanalyzed by Luque & Pallé (2022) on a mass-radius diagram. Curves for Earth-Like (32.5% mantle, 67.5% core) and Water-World (50% water, 50% mantle) interiors shown. *Right*, plot of bulk density normalized to Earth and uncompressed density. The planets are modeled with MAGRATHEA to find the uncompressed density with uncertainty. Trappist-1f and Solar System bodies also shown.

( $1.18 \pm 0.078 R_{\oplus}$ ) and found the secondary eclipse is consistent with the planet not having an atmosphere. These new measurements take the planet from an Earth-like interior to an interior that's possibly between the Earth-like and 50% water interiors. Fig. 5.4 shows most solutions are below the 50% water mass fractions. GJ 1252b sits right between the two hypothesised groups and in such a small sample may suggest the radius gap is not as clean as shown in other works. However, GJ 1252b should be treated more carefully than this analysis as it has a 0.5 day orbit and an null-albedo equilibrium temperature of 1100 K.

To fully simulate each planet requires 660 hours of cpu time or 4.5 days across 12 cores. Filling in this plot provides a test for the abundance of water-worlds.

## 5.4 TRAPPIST-1 Planets from Formation Models

The properties of the seven TRAPPIST-1 (T1) planets are the most accurately determined for planets under  $5 M_{\oplus}$ . In Chapter 6, I will model the planets extensively and use them to test interior models. They also present a laboratory for planet formation scenarios which may be quite different from the Solar System. The masses of the Solar System planets, their water content, and their core mass fractions are used to constrain likely formation scenarios such as the Grand Tack, Nice Model, and instabilities in the giant planets (Gomes et al. 2005; Clement et al. 2018; 2023a;b).

Ormel et al. (2017) proposed that the formation of the T1 system first took place at the ice line where planetesimals formed by the streaming instability. The streaming instability is when solid particles concentrate into dense filaments and undergo gravitational collapse into numerous bound objects. Planetesimals up to  $\sim 100$  km may form in this way (Johansen et al. 2015; Simon et al. 2016; Schäfer et al. 2017; Li et al. 2019). After the initial planetesimals form, they continue to grow by pebble accretion (Johansen & Lambrechts 2017). Each planet then undergoes inward type-I migration and accretes silicate pebbles once it is inside the ice line. The inner most planets stall near the inner edge of the gas disc, which is set by the star’s magnetosphere. This formation has been tested in Huang & Ormel (2021), Schoonenberg et al. (2019), and Ogihara et al. (2022).

While previous  $n$ -body studies have reproduced the broader features of the T1 system, it has proven difficult to reproduce the planet densities and masses, and the orbital architecture of the system when starting from an early stage in planet formation. In a submitted publication led by Dr. Anna Childs, collaborators and I use a collection of numerical tools to model the T1 formation starting just after embryo formation and until gas disc dissipation while reproducing the observed planet densities. In the rest of this section, we use my collaborators’ final constraints on

Table 5.1: Core mass fraction (cmf), mantle mass fraction (mmf), water mass fraction (wmf) and resulting radius for the T1 planets using the average bulk compositions from the simulated planets. We report these properties for starting bodies with a wmf of 0.20 and 0.50.

Starting wmf	Planet	cmf	mmf	wmf	$R_p/R_\oplus$
0.20	b	0.25	0.64	0.11	1.16
	c	0.26	0.65	0.09	1.13
	d	0.27	0.65	0.08	0.79
	e	0.27	0.65	0.08	0.93
	f	0.28	0.65	0.07	1.04
	g	0.28	0.65	0.07	1.12
	h	0.29	0.57	0.14	0.76
0.50	b	0.20	0.52	0.28	1.25
	c	0.22	0.56	0.23	1.21
	d	0.22	0.55	0.22	0.84
	e	0.24	0.57	0.19	0.99
	f	0.24	0.58	0.18	1.10
	g	0.24	0.58	0.18	1.19
	h	0.21	0.44	0.34	0.84

composition to calculate the planet radius and density using the planetary interior structure code MAGRATHEA. We discuss the WMFs along with the elemental compositions of the T1 analogs found in our planet formation models.

We model planets with our average binned values for elemental compositions of T1 analogs found from our formation models. MAGRATHEA assumes a spherically symmetric planet with an iron core, silicate mantle, water hydrosphere, and atmosphere made of an ideal gas. We feed MAGRATHEA the seven average binned values for the iron mass fraction for the core layer, the average binned value of the WMF for the hydrosphere, place all remaining elements into the mantle, and assume a small, Earth-like atmosphere. We use the observed masses of the T1 planets from Agol et al. (2021), the default equations of states and phase diagrams in MAGRATHEA, and a surface temperature of 300 K, slightly higher than the equilibrium temperatures easily reached by an insulating small atmosphere.

To understand how the final bulk compositions and radius are sensitive to the initial water mass fraction we track the composition evolution for bodies that start with either 20% wmf or a 50% wmf. Table 5.1 shows the average binned values for the core mass fraction (cmf), mantle mass fraction (mmf), wmf, and planet radius as determined by MAGRATHEA for each starting wmf. We find that bodies that begin with a 50% wmf result in planets with radii that are larger than the T1 planets. Using the same cmf and mmf, the wmf's need to be reduced down to about 6%, 5%, 10%, 6%, 7%, 9% and 10% for planets b-h, respectively, to obtain the same radii of the T1 planets. These reductions imply that the planets that begin with planetesimals with a 50% wmf must lose up to 75% of their water throughout the formation process in order to match the observed planet densities.

The planets that begin with a 20% wmf result in planets with radii and densities similar to observations of the T1 planets. Our simulated planets b, c and g are slightly larger than the observed T1 planets and so these planets would need to undergo slight volatile loss to reproduce the observed radii. Simulated planets b, c and g are the largest planets in the system and they do experience collisions throughout the formation process which may be a source of volatile loss. Because a 20% wmf reproduces planets with similar radii to the T1 planets without requiring appreciable volatile loss, the starting bodies that formed the T1 planets likely had no less than a 20% wmf on average if they have an Earth-like atmosphere. However, T1-b and T1-c may have water vapor atmospheres which would require an even lower water mass fraction (Acuña et al. 2021).

Volatile loss can take place prior to the planet formation process in the nebulae as the result of chemical interactions between gas and dust, and the formation of chondrules (Cassen 1996; Hirschmann et al. 2021). Later, small planetesimals can lose volatiles as they accrete smaller bodies, which heats the body and leads to differentiation (Norris & Wood 2017; Young et al. 2019).

As the bodies grow into larger embryos which exceed the PIM, planetary growth proceeds via core accretion. The larger bodies collide with one another in giant impacts, which leads to even further volatile loss (Genda & Abe 2005; Schlichting & Mukhopadhyay 2018). Lastly, after the final terrestrial planets have formed, the planets may lose their atmospheres through photoevaporation from the host star (Lammer et al. 2003) or, core-powered mass-loss where heat from the planet’s core is thermally transferred to the planet surface and evaporates the atmosphere (Ginzburg et al. 2018).

## 5.5 Summary

In this chapter, I discuss the use of interior models for small planets to assess the composition of observed planets. Most observational studies that determine or refine the masses of small planets include a section describing the planets’ possible compositions. In the three studies detailed here I use the composition finder in MAGRATHEA, which takes the mass and radius of a planet and finds the water mass fraction at a given refractory core-mass-fraction (r-cmf).

In Sect. 5.2, I discuss the K2-138 planetary system and its diverse compositions. My collaborators and I explore the stability of the system with the observed masses of the planets in MacDonald et al. (2022) and use the compositions to compare formation pathways. I model the interiors of the four inner planets with both water and atmosphere. I find that K2-138b is consistent with a terrestrial composition while K2-138c, K2-138d, and K2-138e require large volatile layers. K2-138f also has a low density, below  $2.068 \text{ g cm}^{-3}$ , and most likely requires the largest atmosphere envelope.

In Sect. 5.3, I discuss the Fulton radius gap and the possible explanation of prevalent water

worlds. I investigate the nine planets reanalyzed in (Luque & Pallé 2022). I draw 200 samples of mass and radius from Gaussian fits to the median and  $\pm 1\sigma$  reported values in for each planet and find the water mass fraction of each planet at r-cmf values from 0 to 1 (inclusive) at steps of 0.02. I summarize all the interior structures found by the composition finder into an "uncompressed density" which roughly estimates the planet's density if the interior was not under compression. The separation of the water-worlds and terrestrial planets is less significant in uncompressed density.

My last investigation in Sect. 5.4 is from a submitted publication with collaborators where I model the TRAPPIST-1 planets from the elemental abundances predicted from formation simulations. I use my collaborators' final constraints on composition to calculate the planet radius and density. We show the planets need to lose 75% of the wmf through their early evolution or form with only 20% wmf to match present day properties if they were formed beyond the ice line.

Our open-source MAGRATHEA is a powerful tool to characterize planet composition and interiors. In this chapter, I showed its use to give insights in the composition of multiplanet systems, in planet demographics, and in formation studies. In the future, I look forward to building collaborations to characterize planets with observational teams such as the KESPRINT consortium Sanchis-Ojeda et al. (2015) and the NEID science team Gupta et al. (2021).

## Chapter 6

### Uncertainties in Inferences of Internal Structure

#### 6.1 Background

In this work, I develop a flexible interior model (Ch. 2) with updated functionality (Ch. 3) and up-to-date material properties (Ch. 4). In Ch. 5, I showed how the compositions of small exoplanets less than  $10 M_{\oplus}$ , can be characterized with my model. These characterizations were completed with a chosen planet model. However, underlying those models are many model choices and experimental material properties.

Previous works are primarily concerned with how degeneracy in interior models and model parameters affect the mass-radius relationship for a given type of planet (Zeng et al. 2016; Unterborn et al. 2018; Hakim et al. 2018; Noack & Lasbleis 2020; Shah et al. 2021). With our flexible and computationally cheap model, I now turn to carrying through observational, model, and experimental uncertainties to inferences of planet composition for planets with both mass and radius constraints. Works often build upon basic characterizations to study mantle convection, atmosphere evolution, and habitability. Accurately representing the uncertainty in interior measurements is important to carry through to these studies.

To quantify uncertainties, I turn to the TRAPPIST-1 (T1) system as a model observation. Gillon et al. (2016) first report the transits of the inner three planets observed with the TRansiting Planets and PlanetIsimals Small Telescope. Gillon et al. (2017) then measure the masses and radii of all

seven currently known planets with transits observed by Spitzer Space Telescope. Grimm et al. (2018) reanalyze the transit-timing variations confirming that the seven planets ranged from just 0.33 to 1.56 Earth-masses. This makes the T1 planets in a class of their own for planets similar to Earth with measured bulk densities (see Fig. 1.1). Planets of Earth-mass are hard to measure; T1 is unique in being a nearby M8 star which has a radius only 16% larger than Jupiter. The transit depth of the T1 planets is comparable to a  $8.4 R_{\oplus}$  around the Sun. In addition, the outermost planet orbits in just 18.8 days leading to many transits and strong perturbations in transit times from the close packed nature of the system. M-stars make up 76% of the main-sequence stars (Ledrew 2001) and are the focus of many current transit searches.

The literature on the T1 system is extensive and growing, and I list the briefest review of relevant literature here. With such a small, cool star, several of the T1 planets are in the "habitable zone" and could have the right temperature for liquid water or ice on the surface. While the planets are bombarded by their active M-star Vida & Roettenbacher (2018), if the planets formed with significant wms (see Sec. 5.4), they could hold onto significant hydrospheres (Bolmont et al. 2017; Dong et al. 2018). Transmission spectroscopy is achievable on the T1 planets. A primordial, hydrogen-dominated, cloud-free atmosphere is ruled out for all planets de Wit et al. (2018). In the near future, detection of  $\text{CO}_2$ ,  $\text{H}_2\text{O}$  and  $\text{CH}_4$  is feasible with JWST for T1 e and f (Fauchez et al. 2019; Mikal-Evans 2022; Lustig-Yaeger et al. 2019). It is not clear how weak atmospheric detection without abundances will affect our understanding of the interior of these planets. But limits on water and out-gassing, would give some bounds to if the planets host significant water mass fractions.

Situated in most estimates of the habitable zone with a null-albedo surface equilibrium temperature of 218 K is T1 f. Median values of T1f from Agol et al. (2021) put it at just over  $1 M_{\oplus}$  and 1



$R_{\oplus}$ , but a bulk density which is 9% lower than Earth. With its larger size (compared to T1 d and e) and being in the middle of the system, T1f has the lowest uncertainties with 3.0% uncertainty in mass and 1.2% uncertainty in radius.

T1f presents a model observation at the edge of our current observing capabilities in order to compare and quantify the effect of model parameters on the inferences of a planet composition. We use T1f as a model observation without considerations of formation, stellar compositions, and evolution. This study also seeks to elucidate the precision needed by future observations to understand planet composition and elucidate the limitations from laboratory studies which will be first reached.

In Sect. 6.2, I set up my standards for data representation and describe how they agree and differ with previous literature. In Sect. 6.3, I find the likely interior structures of all 5 outer T1 planets with my composition finder and the default MAGRATHEA model and detail my findings for T1f (Sect. 6.3.1). Then I examine our uncertainties and their effect on wmf—observational uncertainty in Sect. 6.4.1, model uncertainty in Sect. 6.4.2, and experimental uncertainty in Sect. 6.4.3. I conclude this chapter in Sect. 6.5.

## 6.2 Graphical Representations

Visualizations are important to understanding the many solutions to a planet’s interior for a single observation of mass and radius. I briefly explained ternary diagrams in Sect. 2.5.4 and showed a few examples of planet radius shown on a water-mantle-core mass fraction ternary diagram for a given radius. Here, I go into further details on data visualizations that I use in previous chapters and will use extensively in this chapter.

A ternary plot represents the parameter space defined by three variables which sum to a constant. Each point on the equilateral triangle represents a unique combination of the three components. Each vertex of the equilateral triangle represents 100% of one component and 0% of the other two components. On the opposite edge from a vertex the component that is 100% at that vertex is not-present (0%). The percent of the component increases perpendicular to that edge. At a point the percentage of a component is given by the ratio of the length of a line perpendicular from an edge to the point to the height of the triangle. Ternary diagrams can also take stranger forms by adding a fourth component to make a pyramid, bounding one axes to make a trapezoid, or cutting off the bottom two corners and re-normalizing to make a QAPF (Quartz, Alkali feldspar, Plagioclase, Feldspathoid) diagram.

Ternary diagrams are a common tool used in geology to plot the composition of rocks in terms of mineral content. Common diagrams in geology are soil texture describing the percentage of clay-silt-sand (Foth et al. 1972) and mafic and ultramafic rock diagrams (Maitre et al. 2005). Other uses include the de Finetti diagram which shows the frequency of aa, Aa, and AA genotypes (DeFinetti 1926) and the flammability diagram showing which regions of fuel-oxygen-gas are flammable (Mashuga & Crowl 1998). Recent works from diverse disciplines which use the PYTHON-TERNARY package (Harper et al. 2015) include Harris et al. (2023), Chen et al. (2022), Ravel et al. (2022), and Stemplinger et al. (2021).

The plot is useful in describing a planet with three main compositional components where the axis are given by the fraction of the total mass in that component. In this work, I extensively use water-mantle-core mass fraction ternary diagrams where the axis are read counterclockwise from the apex. The position of a point gives a unique percentage of mass in each fully-differentiated layer of a planet. However, the axis of a ternary may be rotated which makes comparing ternaries

more difficult. In addition, the axis values have a valid clockwise and counterclockwise orientations for their labels.

In this work, I primarily use the orientation shown in Fig. 6.1 *left* (Sect. 5.2 uses an older rotation that I no longer prefer). Unphysical, 100 per cent water planets plot on the top vertex. This makes the dependent mass ratio of core to mantle vary across the bottom edge while the independent water mass percentage varies perpendicular to the bottom edge. Rocky planets with no significant water, like the Earth with 33% core, plot on the bottom edge. Planets with no core plot on the left edge.

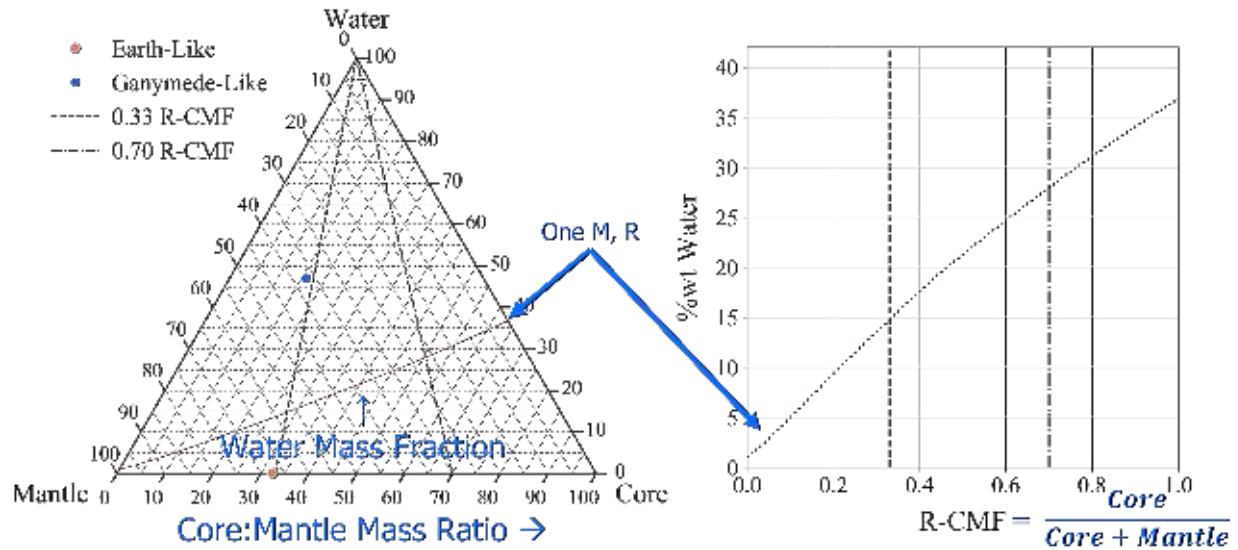


Figure 6.1: The two primary representations of planet composition in this chapter. *Left*, a water-mantle-core mass ternary diagram. *Right*, a water mass fraction with r-cmf (refractory core mass fraction) plot. Helpful definitions are supplied on the plot for the axes. A line of solutions for three-layer internal structure for a planet of given mass and radius at 0.01 steps in r-cmf is shown on both plots. Planets consistent with the r-cmf of Mercury and Earth shown with dashed-dotted and dotted lines. Earth and Ganymede shown on the ternary diagram.

The orientation described here is the same as in Zeng & Seager (2008), although they place labels along the edges. Labels along the edges are common in the exoplanetary literature, but are difficult to read because percentages do not increase along lines orthogonal to the axis as in a typical two dimensional plot. Labels at the corner indicate that that a quantity increases perpendicularly from the opposite edge toward that corner. Seager et al. (2007) and Acuña et al. (2021) also use labels along the edge and use a mantle-water-core orientation. Brugger et al. (2016) and Valencia et al. (2007a) use corner labels but also use the mantle-water-core orientation. This orientation is flipped horizontally and rotated counter-clockwise 120 degrees from my orientation. Other exoplanet works which use ternaries include Rogers & Seager (2010); Madhusudhan et al. (2012); Neil & Rogers (2020).

Planet's which have the same ratio of two layers plot on a line going from a vertex to the opposite edge. On Fig. 6.1 *left*, Ganymede and Earth plot close to one of these lines from the apex to the mantle:core axes. This is because the moon of Saturn from gravitational measurements is consistent with a similar mantle to core ratio as the Earth McKinnon et al. (2004). In Eq. 3.1, we define  $r\text{-cmf}$  which is equal along these lines going from 0 on the left edge to 1 on the right edge. I show a 0.33  $r\text{-cmf}$  line and a Mercury-like 0.7  $r\text{-cmf}$  line.

If we take the  $r\text{-cmf}$  as the dependent variable, we can transform the ternary into a more typical two dimensional plot with  $r\text{-cmf}$  on the x-axis and water mass fraction ( $wmf$ ) on the y-axis. This plot, not used in previous works, is shown in Fig. 6.1 *right*. There is no forbidden regions on the plot unlike a  $wmf$  versus  $cmf$  plot.  $R\text{-cmf}$  here can be equated to  $Fe/(Si+Fe)$ .

In Sec. 2.5.4, we showed the radii of a given mass planet at each position on the plot. But we can also plot the mass percentages for planets of different masses and radii. A planet of any mass with Ganymede's interior structure will plot at the Ganymede-like point. However, there is not

a unique interior structure for a given mass and radius. For three layers, an increase in the core mass will lower the radius, but that radius can stay the same if more of the mantle's mass is also converted to hydrosphere. Thus a mass and radius gives a curve on both plots. One example curve is shown in Fig. 6.1. Planets along this curve of a given mass will have the same radius.

### 6.3 TRAPPIST-1 System Default Compositions

I first show likely interiors for the five planets T1d, e, f, g, and h. The equilibrium temperature of the inner two planets of the T1 system are near the the boiling point of water, so here we focus on the 5 outer planets with temperatures below 300 K (although JWST preliminary results released during the final week of this work has found that the day-to-night side temperature of T1b shows no atmosphere). An analysis of the inner planets with outer planets is a focus of Acuña et al. (2021).

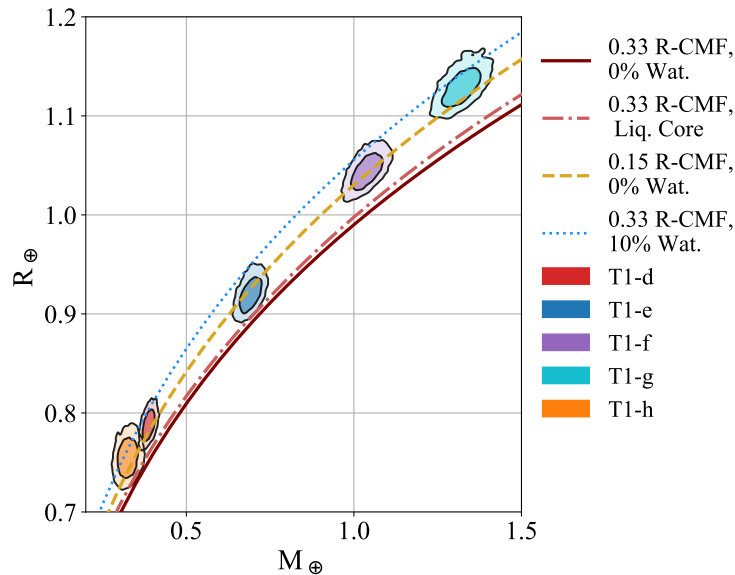


Figure 6.2: 1- and 2- $\sigma$  mass and radius for Trappist-1 d-h from Agol et al. (2021). Four lines of constant interior structure are shown.

I draw 5,000 mass and radius measurements directly found by the Agol et al. (2021) joint analysis. Each draw is a point on their corner plot so represent the actual distribution of the planets' masses and radii<sup>1</sup>. The masses and radii are shown on Fig. 6.2. The planets fall remarkably close to a line of constant composition. The 1-sigma bounds are consistent with a low r-cmf or an Earth-like r-cmf with a small hydrosphere.

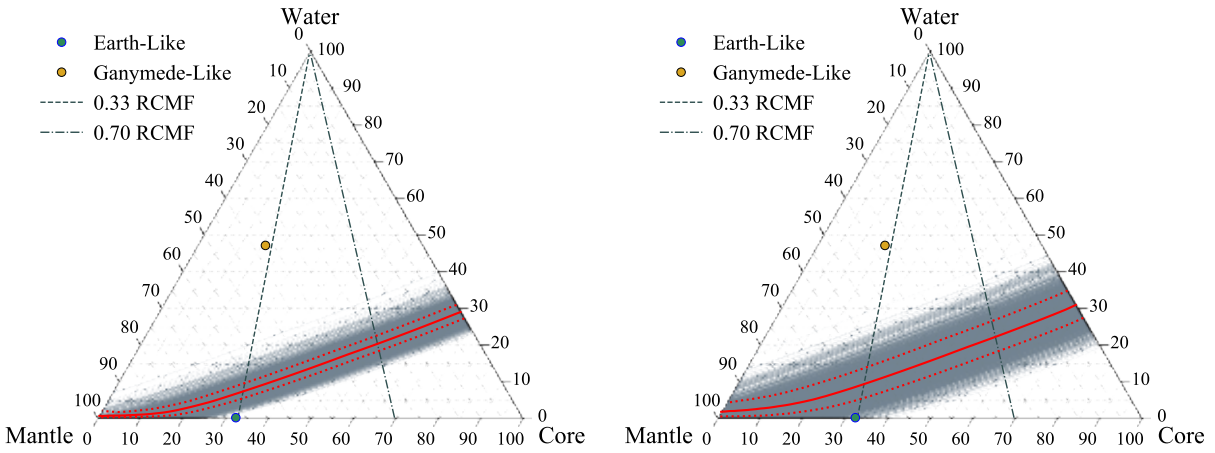


Figure 6.3: *Left*, interior structures which match 5000 draws of mass and radius for T1d. *Right*, interior structures for T1h. *Red lines* show the median and  $\pm 1\sigma$  bounds of wmf across uniform r-cmf.

I use our default MAGRATHEA model and the composition finder with steps of 0.01 r-cmf (Sec. 3.2) to run these mass and radii to find their likely interior. Fig. 6.3 shows on a water-mantle-core mass ternary diagram the likely interiors for T1d and T1h. Median and  $\pm 1\sigma$  bounds are determined from the 15.87, 50, 84.13 percentile in all cases in this work. These plots are

<sup>1</sup>Mass and radius accessed from [https://github.com/ericagol/TRAPPIST1\\_Spitzer](https://github.com/ericagol/TRAPPIST1_Spitzer)

created with approximately 450,000 solutions for the wmf and require around 1.5 million runs of MAGRATHEA. Both T1d and T1h have similar masses— $M_d = 0.388 \pm 0.012$  and  $M_h = 0.326 \pm 0.02$ —but T1h’s lower density predicts a lower wmf.

I show the likely wmf of the five outer planets of T1 with varying r-cmf from the observed parameters in Fig. 6.4. The T1 planets have similar likely interiors, although if the planets have R-cmf above 0.22, Trappist-1 e and g cannot have the same wmf to  $1\sigma$ .

### 6.3.1 T1f Default Model

I now turn to focus on the likely interior of T1f. T1f was measured by Grimm et al. (2018) to have a mass of  $0.934 \pm 0.079 M_{\oplus}$  and radius of  $1.046 \pm 0.03 R_{\oplus}$ . Agol et al. (2021) shifted the density lower ( $0.911^{+0.025}_{-0.029} \rho_{\oplus}$ ) with mass of  $1.039 \pm 0.031 M_{\oplus}$  and radius of  $1.044 \pm 0.013 R_{\oplus}$ . The uncertainty in both mass and radius was cut in half. Fig. 6.5 shows the interiors inferred from both of these observations.

I find that T1f with our default model and a 218 K surface temperature with no discontinuities in temperature needs a  $6.5^{+2}_{-1.5}\%$  wmf at Earth-like r-cmf. If the planet has no hydrosphere it needs a cmf half that of the Earth. I find the likely cmf to be  $14^{+3}_{-2}\%$  at zero wmf. These values are higher than found in Agol et al. (2021) as a result of their older water EoS. The wmf found here matches well with that of Acuña et al. (2021), but they only report  $\pm 1\sigma$  bounds of three-layer composition while I show the entire distribution. My uncertainty is also lower from using the correlated mass radius measurements rather than fitting a gaussian to the reported mass and radius. Three structures are visualized with Blender (see Sec. 3.3) and shown in Fig. 6.6.

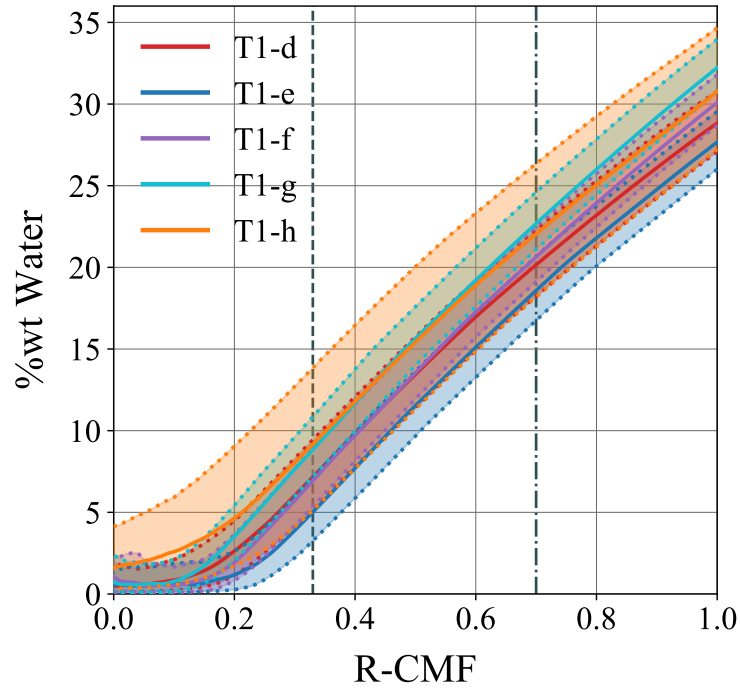
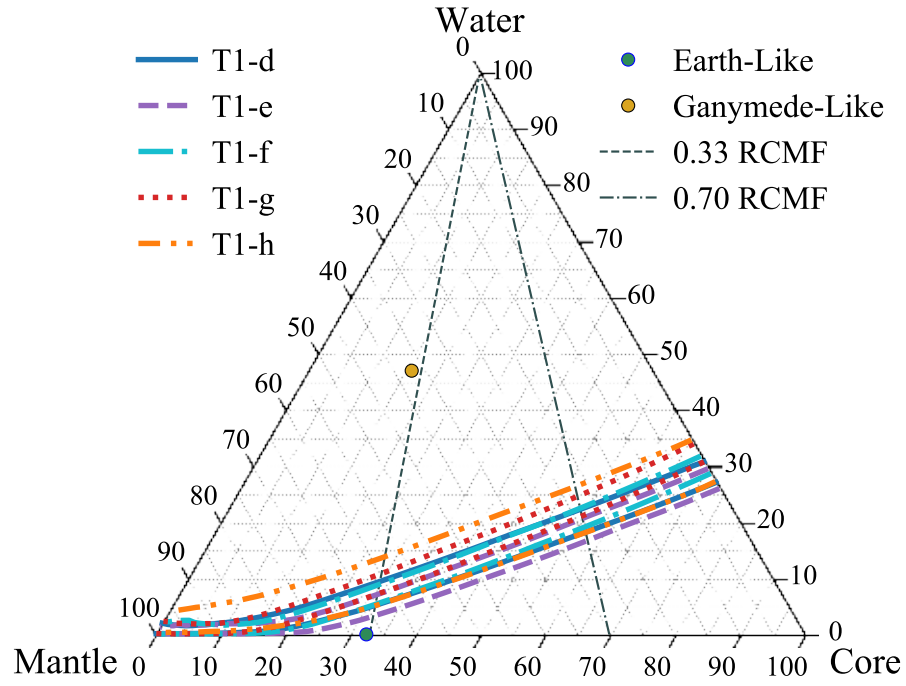


Figure 6.4: *Top*, the  $1\sigma$  wmf of all 5 planets across r-cmf on a ternary. *Bottom*, same as top on a wmf vs r-cmf plot with  $1\sigma$  shaded.



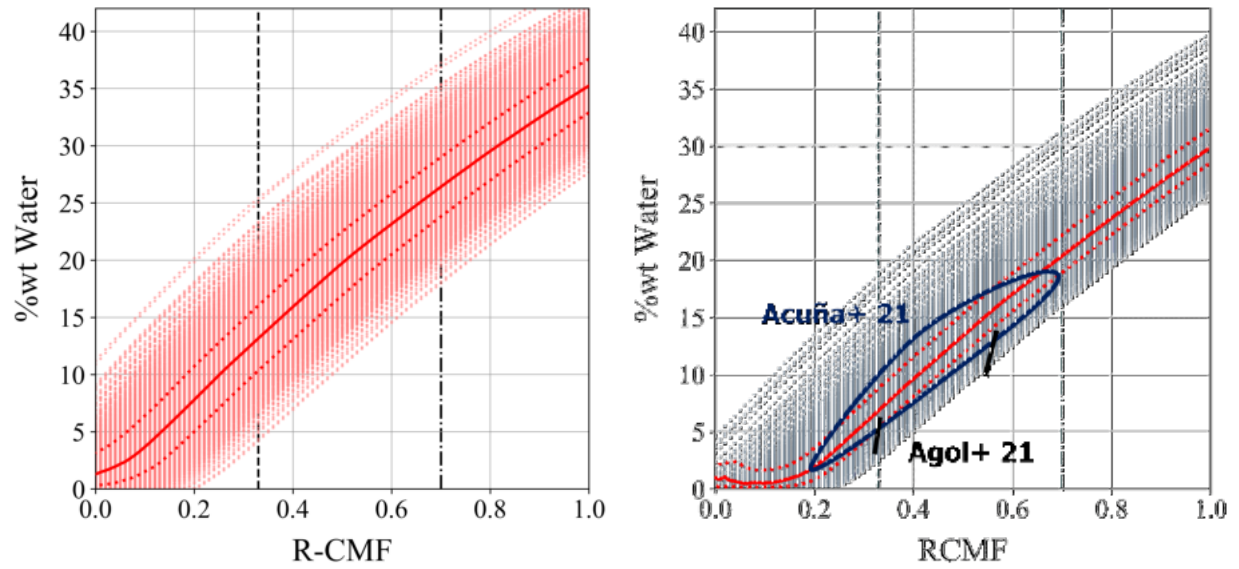


Figure 6.5: *Left*, the wmf at uniform r-cmf which match the observations of Grimm et al. (2018). *Right*, the wmf at uniform r-cmf which match the observations of Agol et al. (2021). *Red lines* show the median and  $\pm 1\sigma$  bounds of wmf across uniform r-cmf. *Right*, the wmf of Agol et al. (2021) at a given cmf and the  $\pm 1\sigma$  compositions from Acuña et al. (2021).

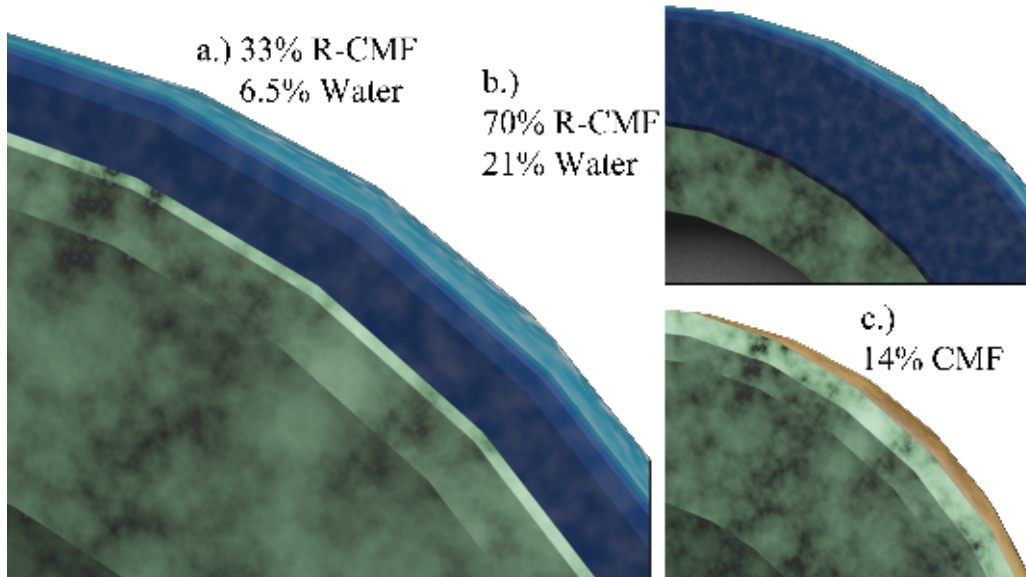


Figure 6.6: Three likely structures of T1f visualized in Blender. In a.) the best-fit wmf for an Earth-like R-CMF with a Ice Ih surface (lightest blue). The planet still has layer of olivine (lightest green) and rwd (under olivine). In b.) the best-fit wmf for a Mercury-like R-CMF with ice X (darkest blue) layer above bridgmanite (medium green). In c.) the best-fit for no water with 14% cmf showing many mantle materials. Post-perovskite is shown in the darkest green.

Table 6.1: 2,500 samples of mass and radius were generated for each row of properties and with median values of Trappist-1f. Uncertainty in wmf shown at 0.33 and 0.60 r-cmf. Final column is uncertainty in cmf at 0% wmf.

Mass Unc %	Radius Unc %	Density Unc %	$r_{m,r}$	Earth-wmf Unc %	Mercury-wmf Unc %	cmf Unc %
3.2	1.0	1.0	0.95	9.1	2.75	10.7
3.2	1.0	4.5	0.00	39	12	43
4.2	0.98	3.0	0.71	24	7.3	25
4.2	0.99	5.1	0.00	44	13	46
10.0	1.0	9.6	0.30	71	23	59
10.3	0.97	10.7	0.00	78	27	61

## 6.4 T1f Uncertainties

### 6.4.1 Observational

Before quantifying model uncertainties, I show the affect of observational uncertainties on composition inferences. We can then compare these uncertainties. To do so, we first fix the radius uncertainty near 1%. Radius measurements are often limited by stellar radii measurements. I create samples of mass and radii based on the median reported values of T1f but with various distributions. I investigate increasing the mass uncertainty from near 3.2% to 4.2% to 10% of the median value. I draw 2500 samples of mass and radius from gaussian distributions with the median of T1f and given uncertainty.

Results are tabulated in Table 6.1 and shown in Fig. 6.7. In the table, the gaussian samples are that with a correlation coefficient between mass and radius of 0. In the table, I also show the results for generated samples that change the density uncertainty from approximately 1% to 3% to 10% which gives nearly the same uncertainty in mass, but makes mass and radius correlated. The correlation coefficient is shown. The correlation of mass and radius is  $r=0.57$  in Agol et al. (2021). I show the inferred uncertainty in wmf at an Earth-like r-cmf and a Mercury-like r-cmf. I

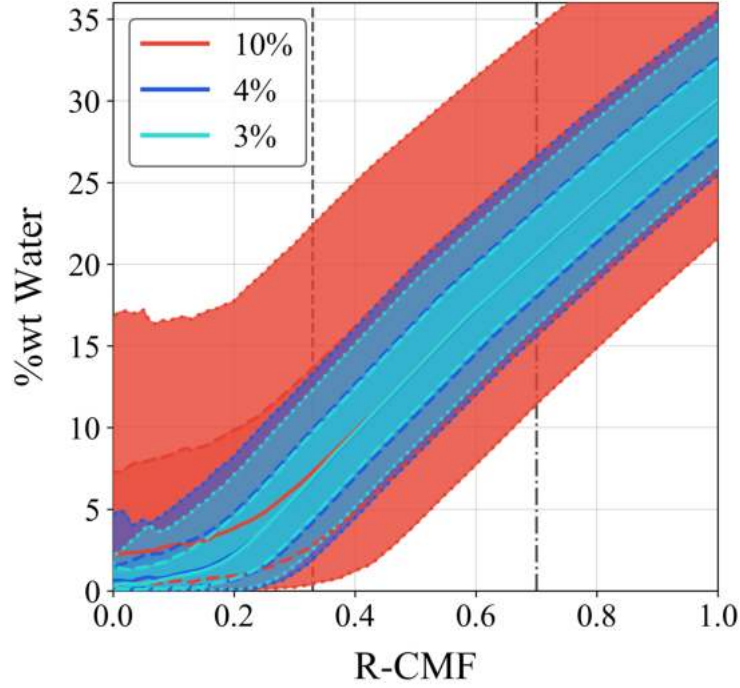


Figure 6.7: The  $1\sigma$  (*darker dashed*) and  $2\sigma$  (*light dotted*) bounds and median in solid line of wmf with r-cmf for samples of gaussian mass and radius similar to that of T1f with varying mass uncertainty represented by the three colors.

also show the uncertainty in the cmf if there is no water.

To further investigate the mass and radius correlation, I create a sample with extreme correlation between mass and radius. Fig. 6.8 shows the sample drawn from gaussian, the Agol et al. (2021) sample, and a mass and radius sample with a correlation coefficient of 0.95. These three samples all have the same distribution of mass and radius distributions. The uncertainty of wmf at an Earth-like r-cmf is  $6.5 \pm 2.6\%$  for the uncorrelated data, Agol et al. (2021) uncertainty is  $\pm 1.8\%$ , and the ideal data with a 0.95 correlation coefficient the uncertainty is as low as  $\pm 0.6\%$ . At a 0.33 r-cmf T1f needs a hydrosphere to  $4\sigma$ , but if the data was more correlated we could know it must have a hydrosphere to  $10\sigma$ . Its essential that observational works report the correlation in mass and radius.

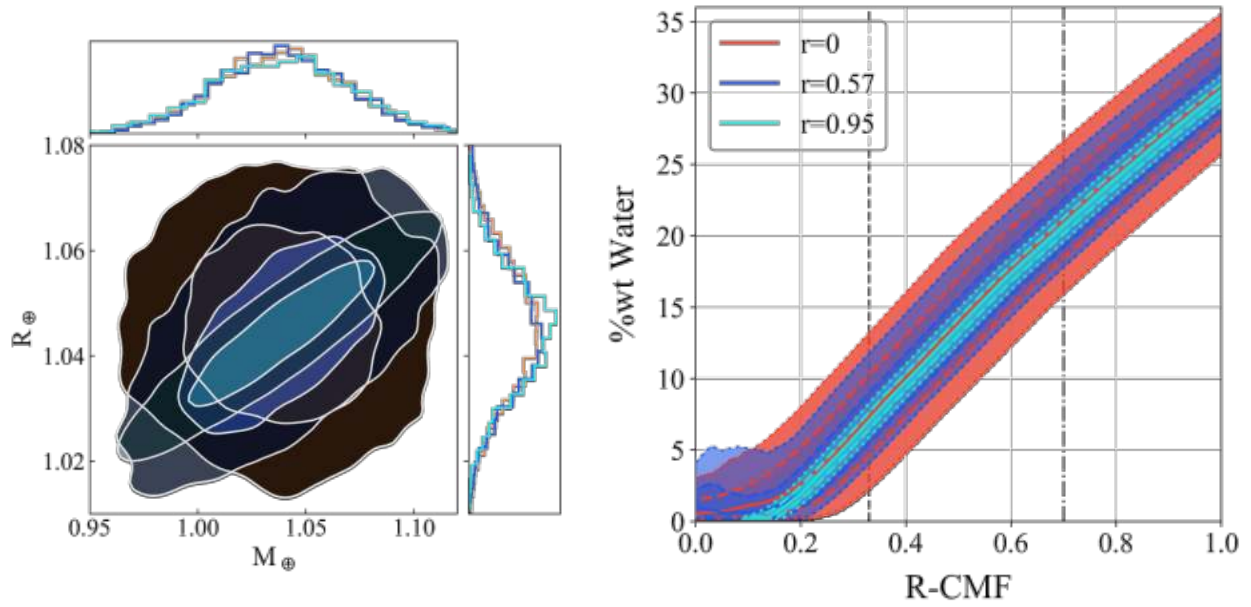


Figure 6.8: *Left*,  $1\sigma$  and  $2\sigma$  ellipses of mass and radius for uncorrelated data (*red*), Agol et al. (2021) (*blue*), and highly correlated data (*cyan*). All distributions have the same median and standard deviation. *Right*, inferred wmf at given r-cmf for the three distributions from *left* with the shown correlation-coefficient.

Table 6.2: 2,500 samples of radius were generated from skewed distributions and paired with with masses drawn from a Gaussian with  $1.039 \pm 0.31 M_{\oplus}$ . *Skew* is the Fisher-Pearson coefficient of skewness. *Earth W%* is the wmf % at a given 0.33 RCM.

Rad.	+1σ %	skew	Dens.	+1σ %	skew	Earth	+1σ %	skew	cmf	+1σ %	skew
$R_{\oplus}$	−1σ %		$\rho_{\oplus}$	−1σ %		W%	−1σ %		%	−1σ %	
1.045	1.1	−1.2	0.91	5.9	0.2	6.9	44	0.1	14	57	0.9
	1.7			4.8			45			50	
1.045	1.3	0.0	0.91	5.0	1.0	6.9	43	0.3	13	54	0.1
	1.3			4.6			39			46	
1.045	1.7	0.9	0.91	4.9	−0.3	6.7	55	1.0	14	42	0.0
	1.2			5.8			40			50	
1.044	2.3	1.7	0.91	4.6	−1.0	6.5	71	1.8	15	33	−0.2
	1.2			6.8			38			47	
1.045	3.4	2.5	0.90	5.3	−1.5	7.0	96	3.0	15	33	−0.2
	1.2			9.4			40			47	

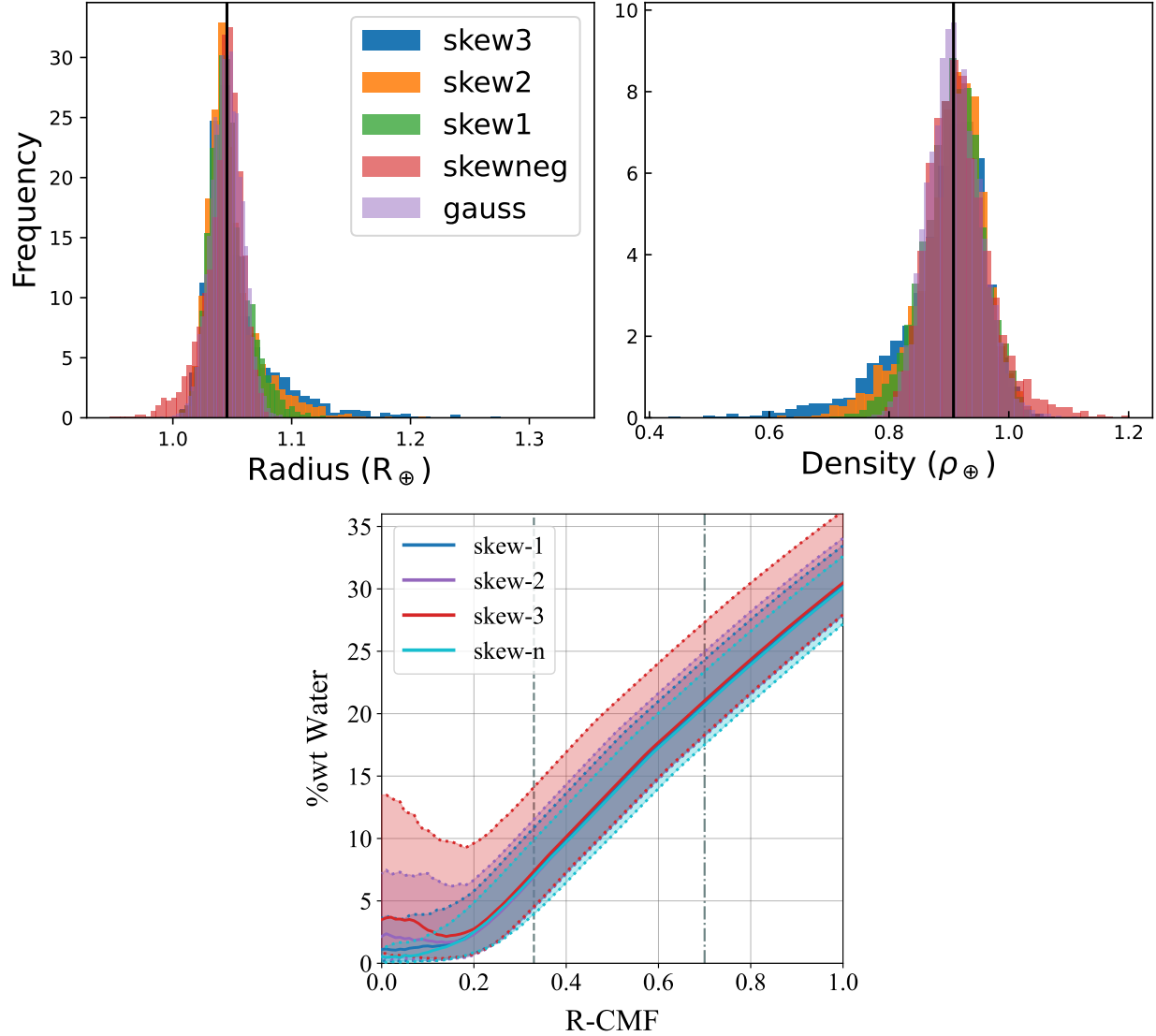


Figure 6.9: *Top*, distributions of radius and density for my injected skewed distributions. *Bottom*, likely wmf of the model data with various skewness. Skew-1, Skew-2, and Skew-3 correspond to the third, fourth, and fifth data set (row) in Table 6.2, and Skew-n is the negative skewed first sample.

Lastly, I detail in Table 6.2 and in Fig. 6.9 an investigation of the skewness in the radius distribution. Radius distributions are often skewed reflecting uncertainty in stellar radii. I create four samples of skewed radii. For each radius in a normal distribution I increase the radius by a percentage of how far it is away from the median value to positively skew the data, and decrease the radii to negatively skew. I iterate this trying different amounts of inflation/deflation until a desired Fisher-Pearson coefficient of skewness is reached. I report the properties of the distributions and the wmf and CMF in the table. The skew in the wmf at a given r-cmf is larger than the skew in the radius or density. I do not explore the kurtosis of the distribution in this work.

#### 6.4.2 Model Choices

When characterizing planet interiors and compositions, choices of best planet model must be taken. Above we assume that T1f's surface is at the null-albedo equilibrium temperature of 218 K. We assume that the planet is fully differentiated and that excess interior heat from formation or radiogenic material has been radiated away over the old age of the system. We assume the mantle is pure magnesium silicates and that the core is pure iron. Here we examine three of these model assumptions that have been suggested in previous literature to affect mass-radius relationships. The results of the three models are shown in Fig. 6.10.

First, I test the need for other magnesium silicate phases than bridgmanite and post perovskite to model T1f. We find for wmf under 15% a there is a layer of ringwoodite under the hydrosphere. However, it's impact on the inferred wmf is negligible at below a tenth of a percent. Upper mantle materials do have different thermal properties and water storage capacities than bridgmanite so may be of importance to future studies.

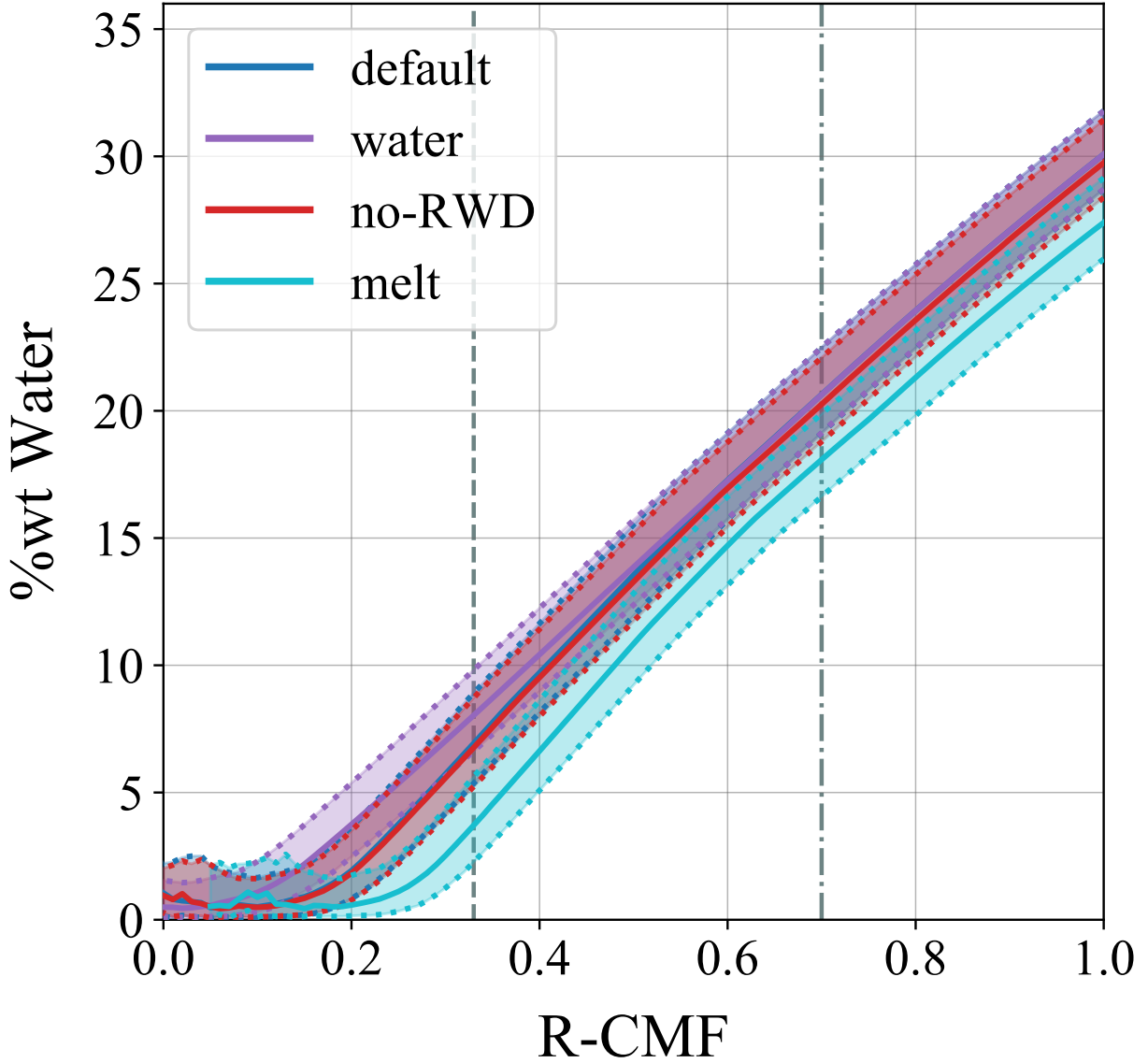


Figure 6.10: Wmf with four large model differences. “Default” is our default model shown in Fig. 6.5. “water” raises the surface temperature to 300 K melting the layer of ice ih. “No-RWD” ignores upper-mantle materials removing the small layer of RWD. “Melt” has a 1500 K discontinuity at the mantle-hydrosphere boundary and core-mantle boundary which creates a liquid core layer.

Second, I increase the surface temperature to 300 K above the 273 K melting temperature of pure water. Any small atmosphere layer will increase the surface temperature of a body. Even Mars with a surface pressure 150 times less than Earth has a average surface temperature 5 K warmer than the equilibrium temperature (Catling & Kasting 2017). This temperature means the surface of T1f’s hydrosphere is water rather than ice ih. At wmf above 1% T1f has a 90 km deep ocean before transitioning to Ice VII. Since water is more compressible than ice ih, to match the observed properties T1f needs more water at low r-cmf in this model.

Lastly, we create temperature discontinuities in the planet from thermal conductive layers at layer boundaries. Similar to the Earth under the core, we start the mantle at 1500 K hotter than the hydrosphere’s innermost temperature. We then start the core another 1500 K hotter than the mantle’s innermost temperature. This reaches the melting temperature of iron. For a planet with 50% cmf that matches T1f’s observed properties, I find this model melts nearly 50% of the core’s mass. Liquid iron is only approximately 3% less dense than solid iron, but with a significant layer of this lack of density the planet needs less water to match observed properties.

If we treat the above models as equally likely, we find the uncertainty in wmf at a given r-cmf increases by 10%. At an Earth-like r-cmf the wmf is better characterized as  $6.5 \pm 2.2\%$ . Other parameters to be investigated is using a non-pure core EoS and decreasing the melting temperature of the core, adding water to the mantle, and adding lighter pyroxenes to the mantle.

### 6.4.3 Experimental

In our planet solver, MAGRATHEA, we often choose to default to the most well determined experimental results. Our iron determined from Smith et al. (2018) (see Sect. 4.3), post-perovskite



(Sakai et al. 2016), Ice VI, and Ice VII (Bezacier et al. 2014) all have experimental uncertainties. The rest of our planet materials are determined in theoretical results which although they do not report uncertainty match their data to experimental results.

I now treat T1f as having a known mass and radius at the median value determined by Agol et al. (2021) and treat our model as the true planet structure. I draw 5000 times from the reported experimental uncertainties in the molar volume, bulk modulus, and first derivative of the bulk modulus for iron, post-perovskite, ice VI and ice VI along with the Grüneisen parameters of post perovskite and the thermal expansivity of the ices. For these 5000 draws, I find the inferred wmf across r-cmf at steps of 0.02 shown in Fig. 6.11. While larger at low r-cmf with high uncertainty in the post-perovskite, the experimental uncertainties are an order of magnitude better than observational uncertainties.

However, in Fig. 6.11 *bottom* I show the uncertainty in inferred wmf if you use the experimental uncertainty in thermal conductivity of ice VII from Fei et al. (1993). Several legacy planet models still use this result, Acuña et al. (2021). Now experimental uncertainties dominate at high water mass fractions with  $1\sigma$  uncertainties only 3 times smaller than observational uncertainties. A future release of SEAFREEZE plans to have a new measurement of high-pressure ice thermal properties from Gibbs Local Basis Functions parametrization (Journaux et al. 2020), and will present a much needed update to the properties of high pressure ices.

An essential note to this finding that experimental uncertainties are small is that interior models of even Earth-size planets extrapolate EoS beyond the range of pressure and temperature they were determined in. Often EoS from different sources will exclude one another to several sigma when extrapolated to high pressure (See Sec. 4.2).

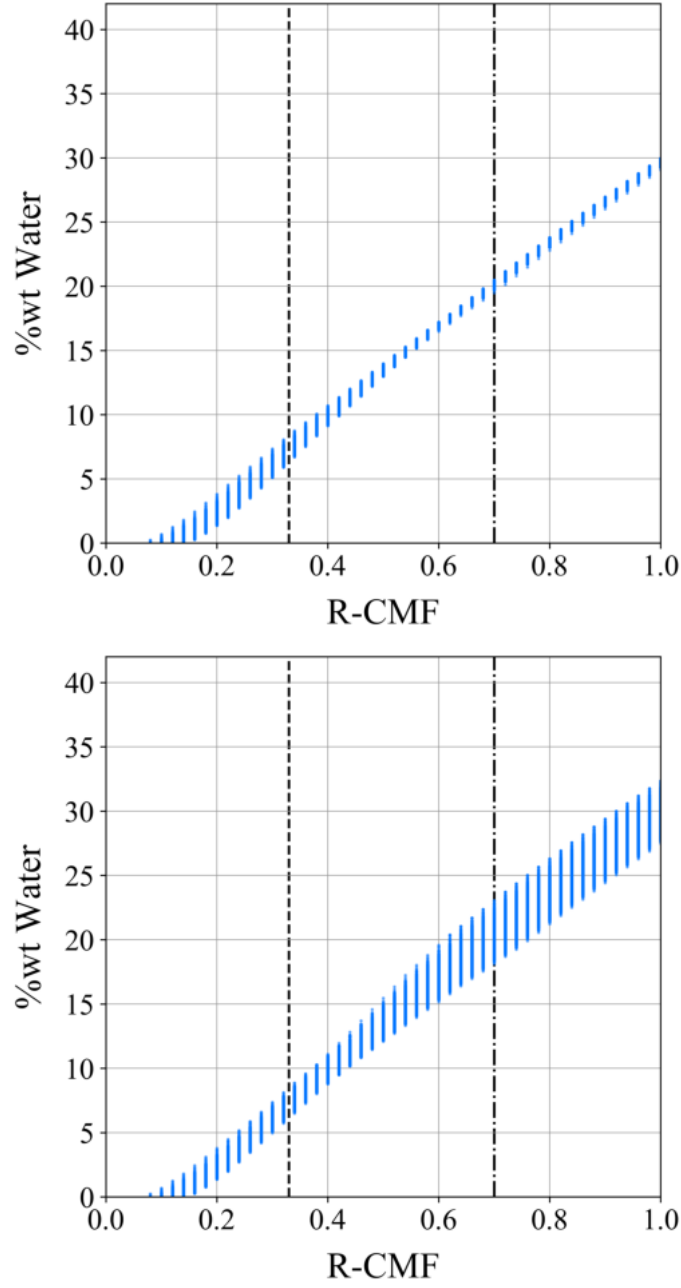


Figure 6.11: Wmf for the median values of mass and radius for T1f, but with varying values for experimentally determined EoSs. We vary parameters such as the bulk modulus but the uncertainty reported in the literature in 5000 draws. *Top*, uncertainty in our default EoSs. *Bottom*, uncertainty including uncertainty in the thermal conductivity of ice VII from Fei et al. (1993).

## 6.5 Summary

In this chapter, I use the Trappist-1 system as a model observation of Earth-like planets. The density of these planets being 1-10% less than the Earth may have significant hydrospheres. I explore the uncertainty in inferences of water mass fraction from just observed mass and radius.

In Sect. 6.2, I describe the water-mantle-core ternary diagram and the wmf versus r-cmf plot used throughout this work. In Sec. 6.3, I show my characterizations of the 5 outer planets with MAGRATHEA and give further details on our characterization of the Earth-like T1f which resides in the habitable zone. In Sec. 6.4.1, I create samples of mass and radius based off of T1f to explore our current and future observational capabilities to constrain planet composition. I emphasize the importance of considering the correlation between mass and radius. In Sec. 6.4.2, I begin a study of model parameters adjusting some of the largest model choices and describing their effect on wmf and find model parameters can affect wmf inferences at given r-cmf by 2-3%. Finally, in Sec. 6.4.3 I show the uncertainty in our model from purely experimental equations of state which are an order of magnitude better than our observational uncertainties.

The results of this chapter are still in progress. In the simplest model of a three layer planet there is at least 40 independent parameters from the input mass in each layer to the material properties of each planet building material. The findings of this work will carry through uncertainty in inferred planet composition from observations, model parameters, and laboratory uncertainty.

## Chapter 7

### Conclusion

The bulk density of the around 100 confirmed “small” exoplanets with accurate radii and accurate masses less than 10 Earth-masses indicate that exoplanets have more diverse compositions than the terrestrial planets in the Solar System. However with many solutions to the possible compositions of multi-layer differentiated planets, these planets’ inferred compositions and interior structures from mass and radius alone needs to be carefully modeled and characterized. Although there are many open questions in planetary science, we can apply our knowledge of planetary cores, mantles, and hydrosphere in the Solar System to exoplanets. Interior structure models are a useful tool in applying Solar System results to exoplanet studies. Constraining the interior of exoplanets with these models is important to constraining essential aspect of habitability like volatile abundance and the presence of a magnetic field.

In this work, I employ and build collaborations around my interior structure model with the intention of creating reproducible planet characterizations across the field. The two projects that will continue to be my scientific objectives are to:

1. Improve and add complexity to interior models (Ch. 2, 3, 4).
2. Characterize the composition of exoplanets in demographic studies (Ch. 5, 6).

These two thematic projects are key in linking material science and geology with the next generation of planet observations.

In Chapter 2, I detail the development and functionality of MAGRATHEA, the only open-source planet interior structure code with transparent and flexible model parameters. The code integrates the hydrostatic equation in order to shoot for the correct planet radius given the mass in each layer. The code returns the pressure, temperature, density, phase, and radius at steps of enclosed mass. The code support 4 layers: core, mantle, hydrosphere, and atmosphere. Each layer has a phase diagram with equations of state chosen for each phase, so while the input mass determines layer boundaries the pressure and temperature within a layer determine the material. The code features transparent storage structures for materials accepting and integrating between various formulations of the EoS. I developed the code with Dr. Chenliang Huang and Dr. Jason Steffen and published this chapter in Huang et al. (2022).

In Chapter 3, I add functionality and an addition to MAGRATHEA. I first detail a composition finder which I added to characterize the solutions to a planet's internal structure which match a given mass and radius. I solve these compositions at uniform steps across the refractory core-mass-fraction ( $r\text{-cmf}$ ). I use this finder extensively in Ch. 5 and Ch. 6. Second, I show how our one dimensional results can be represented in three dimensions with the animator BLENDER. This is useful for visualizing the volume of different layers and their impact on the planet's properties. I discuss current and future development opportunities for the code and related codes.

In Chapter 4, I present my efforts to expand the EoS library of MAGRATHEA and include the most up-to-date experimental results. I show how these EoS affect the bulk properties of planets throughout. I include a new water-ice EoS determined by high-pressure physics collaborators which refined the transition pressures and bulk modulus of high-pressure ice and discovered a transitional tetragonal phase between Ice VII and Ice X. Collaborators and I published the ice EoS impact on planets in Huang et al. (2021). Second, I determine the thermal properties of a

hcp iron EoS from Smith et al. (2018) to be MAGRATHEA’s default core EoS. I then work with two undergraduate mentees to expand the core and mantle phase diagram with low pressure EoSs and show their impact on planets. I summarize future efforts to expand the EoS library and stay up-to-date with material properties.

In Chapter 5, I turn to characterizing planets in a number of studies. I show how characterizing planet composition can be used in studies of dynamics, observational demographics, and formation models. The dynamics work explores formation pathways of the resonant chain in K2-138 led by Dr. Mariah MacDonald and published in MacDonald et al. (2022). I constrain the water mass fraction (wmf) and atmosphere mass fraction of four planets in K2-138 with well determined mass and radii and discuss their possible diverse compositions. The observational work tests the hypothesis that the two populations of M-dwarf planets in Luque & Pallé (2022) are made up of water worlds and rocky worlds. I find less separation in the planets’ uncompressed density. Finally, in the formation work I inform our interior model with compositions from dust condensation and planet evolution in the TRAPPIST-1 (T1) system this work led by Dr. Anna Childs is currently submitted for publication. We find the planets must form with only 20% wmf or lose large amounts of water if formed through pebble accretion beyond the ice line. For collaborative works in both Ch. 4 and Ch. 5, I reproduce fully only sections of which I am the primary author.

In Chapter 6, I combine our flexible interior model and the characterization of planet interiors to test how uncertainties propagate to our inferences of planet composition. I characterize the outer 5 planets of the T1 system with our default MAGRATHEA model. I then focus on T1f as a model observation of an Earth-sized and Earth-mass exoplanet. I show the inferred wmf at varying r-cmf and the cmf at 0% wmf for the planet with different observational uncertainties, model choices, and experimental uncertainty in EoS. While experimental EoS uncertainties are small compared to

observational uncertainties, our model choices are a first order effect on the inferred wmf at given r-cmf.

The population of small planets with accurately determined masses and radii is growing enabling the demographic study of composition. Several lines of future inquiring are presented in this work. Of promise is including mixtures into planetary interior models (Sec. 4.6), filling in the uncompressed density plot to test for water worlds (Sec. 5.3), constraining the uniformity of the TRAPPIST-1f system (Sec. 6.3), and testing how more model parameters affect our inferences of composition (Sec. 6.4.2). Throughout my future research, I will continually look for relationships and categories for small planets with state-of-the-art interior models to understand the diversity of planet interiors.

## References

- Acuña, L., Deleuil, M., Mousis, O., Marcq, E., Levesque, M., & Aguichine, A. 2021, *A&A*, 647, A53
- Adams, D. 1995-2001, *The Hitchhiker's Guide to the Galaxy* (New York: Harmony Books)
- Agol, E., Dorn, C., Grimm, S. L., Turbet, M., Ducrot, E., Delrez, L., Gillon, M., Demory, B.-O., Burdanov, A., Barkaoui, K., Benkhaldoun, Z., Bolmont, E., Burgasser, A., Carey, S., de Wit, J., Fabrycky, D., Foreman-Mackey, D., Haldemann, J., Hernandez, D. M., Ingalls, J., Jehin, E., Langford, Z., Leconte, J., Lederer, S. M., Luger, R., Malhotra, R., Meadows, V. S., Morris, B. M., Pozuelos, F. J., Queloz, D., Raymond, S. N., Selsis, F., Sestovic, M., Triaud, A. H. M. J., & Van Grootel, V. 2021, *PSJ*, 2, 1
- Al'Tshuler, L. V., Brusnikin, S. E., & Kuz'menkov, E. A. 1987, *Journal of Applied Mechanics and Technical Physics*, 28, 129
- Anderson, O. L., Isaak, D. L., & Oda, H. 1991, *J. Geophys. Res.*, 96, 18,037
- Anderson, W. W. & Ahrens, T. J. 1994, *Journal of Geophysical Research*, 99, 4273
- Anglada-Escudé, G., Amado, P. J., Barnes, J., Berdiñas, Z. M., Butler, R. P., Coleman, G. A. L., de La Cueva, I., Dreizler, S., Endl, M., Giesers, B., Jeffers, S. V., Jenkins, J. S., Jones, H. R. A., Kiraga, M., Kürster, M., López-González, M. J., Marvin, C. J., Morales, N., Morin, J., Nelson, R. P., Ortiz, J. L., Ofir, A., Paardekooper, S.-J., Reiners, A., Rodríguez, E., Rodríguez-López, C., Sarmiento, L. F., Strachan, J. P., Tsapras, Y., Tuomi, M., & Zechmeister, M. 2016, *Nature*, 536, 437
- Anzellini, S., Dewaele, A., Mezouar, M., Loubeyre, P., & Morard, G. 2013, *Science*, 340, 464
- Apai, D., Banzatti, A., Ballering, N. P., Bergin, E. A., Bixel, A., Birnstiel, T., Bose, M., Brittain, S., Cadillo-Quiroz, H., Carrera, D., Ciesla, F., Close, L., Desch, S. J., Dong, C., Dressing, C. D., Fernandes, R. B., France, K., Gharib-Nezhad, E., Haghighipour, N., Hartnett, H. E., Hasegawa, Y., Jang-Condell, H., Kalas, P., Kane, S. R., Kim, J. S., Krijt, S., Lisse, C., López-Morales, M., Malhotra, R., Morrison, S., Mulders, G. D., Pontoppidan, K. M., Scharf, C., Schwarz, K. R., Schwieterman, E. W., Stassun, K. G., Turner, N., Wagner, K., & Young, P. 2019, *BAAS*, 51, 475
- Armstrong, D. J., Lopez, T. A., Adibekyan, V., Booth, R. A., Bryant, E. M., Collins, K. A., Deleuil, M., Emsenhuber, A., Huang, C. X., King, G. W., Lillo-Box, J., Lissauer, J. J., Matthews, E., Mousis, O., Nielsen, L. D., Osborn, H., Otegi, J., Santos, N. C., Sousa, S. G., Stassun, K. G., Veras, D., Ziegler, C., Acton, J. S., Almenara, J. M., Anderson, D. R., Barrado, D., Barros, S. C. C., Bayliss, D., Belardi, C., Bouchy, F., Briceño, C., Brogi, M., Brown, D. J. A., Burleigh, M. R., Casewell, S. L., Chaushev, A. e., Ciardi, D. R., Collins, K. I., Colón, K. D., Cooke, B. F., Crossfield, I. J. M., Díaz, R. F., Mena, E. D., Demangeon, O. D. S., Dorn, C., Dumusque, X., Eig Müller, P., Fausnaugh, M., Figueira, P., Gan, T., Gandhi, S., Gill, S., Gonzales, E. J., Goad, M. R., Günther, M. N., Helled, R., Hoggatpanah, S., Howell, S. B., Jackman, J., Jenkins, J. S., Jenkins, J. M., Jensen, E. L. N., Kennedy, G. M., Latham, D. W., Law, N., Lendl, M., Lozovsky, M., Mann, A. W., Moyano, M., McCormac, J., Meru, F., Mordasini, C., Osborn, A., Pollacco, D., Queloz, D., Raynard, L., Ricker, G. R., Rowden, P., Santerne, A., Schlieder, J. E., Seager,



- S., Sha, L., Tan, T.-G., Tilbrook, R. H., Ting, E., Udry, S., Vanderspek, R., Watson, C. A., West, R. G., Wilson, P. A., Winn, J. N., Wheatley, P., Villaseñor, J. N., Vines, J. I., & Zhan, Z. 2020, *Nature*, 583, 39
- Báez, L. A. & Clancy, P. 1995, *J. Chem. Phys.*, 103, 9744
- Barnes, R., Luger, R., Deitrick, R., Driscoll, P., Quinn, T. R., Fleming, D. P., Smotherman, H., McDonald, D. V., Wilhelm, C., Garcia, R., Barth, P., Guyer, B., Meadows, V. S., Bitz, C. M., Gupta, P., Domagal-Goldman, S. D., & Armstrong, J. 2020, *PASP*, 132, 024502
- Barros, S. C. C., Demangeon, O. D. S., Alibert, Y., Leleu, A., Adibekyan, V., Lovis, C., Bossini, D., Sousa, S. G., Hara, N., Bouchy, F., Lavie, B., Rodrigues, J., Gomes da Silva, J., Lillo-Box, J., Pepe, F. A., Tabernero, H. M., Zapatero Osorio, M. R., Sozzetti, A., Suárez Mascareño, A., Micela, G., Allende Prieto, C., Cristiani, S., Damasso, M., Di Marcantonio, P., Ehrenreich, D., Faria, J., Figueira, P., González Hernández, J. I., Jenkins, J., Lo Curto, G., Martins, C. J. A. P., Micela, G., Nunes, N. J., Pallé, E., Santos, N. C., Rebolo, R., Seager, S., Twicken, J. D., Udry, S., Vanderspek, R., & Winn, J. N. 2022, *A&A*, 665, A154
- Batalha, N. M., Borucki, W. J., Bryson, S. T., Buchhave, L. A., Caldwell, D. A., Christensen-Dalsgaard, J., Ciardi, D., Dunham, E. W., Fressin, F., Gautier, Thomas N., I., Gilliland, R. L., Haas, M. R., Howell, S. B., Jenkins, J. M., Kjeldsen, H., Koch, D. G., Latham, D. W., Lissauer, J. J., Marcy, G. W., Rowe, J. F., Sasselov, D. D., Seager, S., Steffen, J. H., Torres, G., Basri, G. S., Brown, T. M., Charbonneau, D., Christiansen, J., Clarke, B., Cochran, W. D., Dupree, A., Fabrycky, D. C., Fischer, D., Ford, E. B., Fortney, J., Girouard, F. R., Holman, M. J., Johnson, J., Isaacson, H., Klaus, T. C., Machalek, P., Moorehead, A. V., Morehead, R. C., Ragozzine, D., Tenenbaum, P., Twicken, J., Quinn, S., VanCleve, J., Walkowicz, L. M., Welsh, W. F., Devore, E., & Gould, A. 2011, *ApJ*, 729, 27
- Batalha, N. M., Rowe, J. F., Bryson, S. T., Barclay, T., Burke, C. J., Caldwell, D. A., Christiansen, J. L., Mullally, F., Thompson, S. E., Brown, T. M., Dupree, A. K., Fabrycky, D. C., Ford, E. B., Fortney, J. J., Gilliland, R. L., Isaacson, H., Latham, D. W., Marcy, G. W., Quinn, S. N., Ragozzine, D., Shporer, A., Borucki, W. J., Ciardi, D. R., Gautier, Thomas N., I., Haas, M. R., Jenkins, J. M., Koch, D. G., Lissauer, J. J., Rapin, W., Basri, G. S., Boss, A. P., Buchhave, L. A., Carter, J. A., Charbonneau, D., Christensen-Dalsgaard, J., Clarke, B. D., Cochran, W. D., Demory, B.-O., Desert, J.-M., Devore, E., Doyle, L. R., Esquerdo, G. A., Everett, M., Fressin, F., Geary, J. C., Girouard, F. R., Gould, A., Hall, J. R., Holman, M. J., Howard, A. W., Howell, S. B., Ibrahim, K. A., Kinemuchi, K., Kjeldsen, H., Klaus, T. C., Li, J., Lucas, P. W., Meibom, S., Morris, R. L., Prša, A., Quintana, E., Sanderfer, D. T., Sasselov, D., Seader, S. E., Smith, J. C., Steffen, J. H., Still, M., Stumpe, M. C., Tarter, J. C., Tenenbaum, P., Torres, G., Twicken, J. D., Uddin, K., Van Cleve, J., Walkowicz, L., & Welsh, W. F. 2013, *ApJS*, 204, 24
- Baumeister, P., Padovan, S., Tosi, N., Montavon, G., Nettelmann, N., MacKenzie, J., & Godolt, M. 2020, *ApJ*, 889, 42
- Beard, C., Robertson, P., Kanodia, S., Lubin, J., Cañas, C. I., Gupta, A. F., Holcomb, R., Jones, S., Libby-Roberts, J. E., Lin, A. S. J., Mahadevan, S., Stefánsson, G., Bender, C. F., Blake, C. H., Cochran, W. D., Endl, M., Everett, M., Ford, E. B., Fredrick, C., Halverson, S., Hebb, L., Li, D., Logsdon, S. E., Luhn, J., McElwain, M. W., Metcalf, A. J., Ninan, J. P., Rajagopal, J., Roy, A., Schutte, M., Schwab, C., Terrien, R. C., Wisniewski, J., & Wright, J. T. 2022, *ApJ*, 936, 55
- Belonoshko, A. B., Dorogokupets, P. I., Johansson, B., Saxena, S. K., & Koči, L. 2008, *Physical Review B*, 78, 104107
- Belonoshko, A. B., Skorodumova, N. V., Rosengren, A., Ahuja, R., Johansson, B., Burakovsky,

- L., & Preston, D. L. 2005a, *Phys. Rev. Lett.*, 94, 195701
- . 2005b, *Phys. Rev. Lett.*, 94, 195701
- Benedix, G. K., McCoy, T. J., Keil, K., & Love, S. G. 2000, *Meteoritics & Planetary Science*, 35, 1127
- Benneke, B., Wong, I., Piaulet, C., Knutson, H. A., Lothringer, J., Morley, C. V., Crossfield, I. J. M., Gao, P., Greene, T. P., Dressing, C., Dragomir, D., Howard, A. W., McCullough, P. R., Kempton, E. M. R., Fortney, J. J., & Fraine, J. 2019, *ApJ*, 887, L14
- Bennett, D. P., Bond, I. A., Udalski, A., Sumi, T., Abe, F., Fukui, A., Furusawa, K., Hearnshaw, J. B., Holderness, S., Itow, Y., Kamiya, K., Korpela, A. V., Kilmartin, P. M., Lin, W., Ling, C. H., Masuda, K., Matsubara, Y., Miyake, N., Muraki, Y., Nagaya, M., Okumura, T., Ohnishi, K., Perrott, Y. C., Rattenbury, N. J., Sako, T., Saito, T., Sato, S., Skuljan, L., Sullivan, D. J., Sweatman, W. L., Tristram, P. J., Yock, P. C. M., Kubiak, M., Szymański, M. K., Pietrzyński, G., Soszyński, I., Szewczyk, O., Wyrzykowski, Ł., Ulaczyk, K., Batista, V., Beaulieu, J. P., Brilliant, S., Cassan, A., Fouqué, P., Kervella, P., Kubas, D., & Marquette, J. B. 2008, *ApJ*, 684, 663
- Bezacier, L., Journaux, B., Perrillat, J.-P., Cardon, H., Hanfland, M., & Daniel, I. 2014, *The Journal of Chemical Physics*, 141, 104505
- Bolmont, E., Selsis, F., Owen, J. E., Ribas, I., Raymond, S. N., Leconte, J., & Gillon, M. 2017, *MNRAS*, 464, 3728
- Bonfils, X., Astudillo-Defru, N., Díaz, R., Almenara, J. M., Forveille, T., Bouchy, F., Delfosse, X., Lovis, C., Mayor, M., Murgas, F., Pepe, F., Santos, N. C., Ségransan, D., Udry, S., & Wünsche, A. 2018, *A&A*, 613, A25
- Bonnarel, F., Fernique, P., Bienaymé, O., Egret, D., Genova, F., Louys, M., Ochsenbein, F., Wenger, M., & Bartlett, J. G. 2000, *A&AS*, 143, 33
- Bonsor, A., Jofré, P., Shorttle, O., Rogers, L. K., Xu, S., & Melis, C. 2021, *MNRAS*, 503, 1877
- Bouchet, J., Mazevet, S., Morard, G., Guyot, F., & Musella, R. 2013, *Physical Review B*, 87, 094102
- Bouhifd, M. A., Andraut, D., Fiquet, G., & Richet, P. 1996, *Geophys. Res. Lett.*, 23, 1143
- Brennan, M. C., Fischer, R. A., Couper, S., Miyagi, L., Antonangeli, D., & Morard, G. 2021, *Journal of Geophysical Research (Solid Earth)*, 126, e2020JB021077
- Brown, J. M. 2018, *Fluid Phase Equilibria*, 463, 18
- Brugger, B., Mousis, O., Deleuil, M., & Deschamps, F. 2017, *ApJ*, 850, 93
- Brugger, B., Mousis, O., Deleuil, M., & Lunine, J. I. 2016, *ApJ*, 831, L16
- Buchan, A. M., Bonsor, A., Shorttle, O., Wade, J., Harrison, J., Noack, L., & Koester, D. 2022, *MNRAS*, 510, 3512
- Butler, R. P., Wright, J. T., Marcy, G. W., Fischer, D. A., Vogt, S. S., Tinney, C. G., Jones, H. R. A., Carter, B. D., Johnson, J. A., McCarthy, C., & Penny, A. J. 2006, *ApJ*, 646, 505
- Cadieux, C., Doyon, R., Plotnykov, M., Hébrard, G., Jahandar, F., Artigau, É., Valencia, D., Cook, N. J., Martioli, E., Vandal, T., Donati, J.-F., Cloutier, R., Narita, N., Fukui, A., Hirano, T., Bouchy, F., Cowan, N. B., Gonzales, E. J., Ciardi, D. R., Stassun, K. G., Arnold, L., Benneke, B., Boisse, I., Bonfils, X., Carmona, A., Cortés-Zuleta, P., Delfosse, X., Forveille, T., Fouqué, P., Gomes da Silva, J., Jenkins, J. M., Kiefer, F., Kóspál, Á., Lafrenière, D., Martins, J. H. C., Moutou, C., do Nascimento, J. D., Ould-Elhkim, M., Pelletier, S., Twicken, J. D., Bouma, L. G., Cartwright, S., Darveau-Bernier, A., Grankin, K., Ikoma, M., Kagitani, T., Kawauchi, K., Kodama, T., Kotani, T., Latham, D. W., Menou, K., Ricker, G., Seager, S., Tamura, M.,

- Vanderspek, R., & Watanabe, N. 2022, *AJ*, 164, 96
- Cassen, P. 1996, *Meteoritics & Planetary Science*, 31, 793
- Catling, D. C. & Kasting, J. F. 2017, *Atmospheric Evolution on Inhabited and Lifeless Worlds* (Cambridge University Press)
- Chabrier, G., Mazevet, S., & Soubiran, F. 2019, *ApJ*, 872, 51
- Chandra, R., Dagum, L., Kohr, D., Menon, R., Maydan, D., & McDonald, J. 2001, *Parallel programming in OpenMP* (Morgan kaufmann)
- Chandrasekhar, S. 1938, *ApJ*, 87, 535
- Charbonneau, D., Brown, T. M., Latham, D. W., & Mayor, M. 2000, *ApJ*, 529, L45
- Chaturvedi, P., Bluhm, P., Nagel, E., Hatzes, A. P., Morello, G., Brady, M., Korth, J., Molaverdikhani, K., Kossakowski, D., Caballero, J. A., Guenther, E. W., Pallé, E., Espinoza, N., Seifahrt, A., Lodieu, N., Cifuentes, C., Furlan, E., Amado, P. J., Barclay, T., Bean, J., Béjar, V. J. S., Bergond, G., Boyle, A. W., Ciardi, D., Collins, K. A., Collins, K. I., Esparza-Borges, E., Fukui, A., Gnilka, C. L., Goeke, R., Guerra, P., Henning, T., Herrero, E., Howell, S. B., Jeffers, S. V., Jenkins, J. M., Jensen, E. L. N., Kasper, D., Kodama, T., Latham, D. W., López-González, M. J., Luque, R., Montes, D., Morales, J. C., Mori, M., Murgas, F., Narita, N., Nowak, G., Parviainen, H., Passegger, V. M., Quirrenbach, A., Reffert, S., Reiners, A., Ribas, I., Ricker, G. R., Rodriguez, E., Rodríguez-López, C., Schlecker, M., Schwarz, R. P., Schweitzer, A., Seager, S., Stefánsson, G., Stockdale, C., Tal-Or, L., Twicken, J. D., Vanaverbeke, S., Wang, G., Watanabe, D., Winn, J. N., & Zechmeister, M. 2022, *A&A*, 666, A155
- Chauvin, G., Lagrange, A. M., Dumas, C., Zuckerman, B., Mouillet, D., Song, I., Beuzit, J. L., & Lowrance, P. 2004, *A&A*, 425, L29
- Chen, H. & Rogers, L. A. 2016, *ApJ*, 831, 180
- Chen, W.-C., Vohra, Y. K., & Chen, C.-C. 2022, *ACS omega*, 7, 21035
- Choukroun, M. & Grasset, O. 2007, *Journal of Chemical Physics*, 127, 124506
- Clement, M. S., Chambers, J. E., Kaib, N. A., Raymond, S. N., & Jackson, A. P. 2023a, *Icarus*, 394, 115445
- Clement, M. S., Deienno, R., & Izidoro, A. 2023b, *Icarus*, 389, 115260
- Clement, M. S., Kaib, N. A., Raymond, S. N., & Walsh, K. J. 2018, *Icarus*, 311, 340
- Cloutier, R., Astudillo-Defru, N., Doyon, R., Bonfils, X., Almenara, J. M., Bouchy, F., Delfosse, X., Forveille, T., Lovis, C., Mayor, M., Menou, K., Murgas, F., Pepe, F., Santos, N. C., Udry, S., & Wünsche, A. 2018, *ArXiv e-prints*, arXiv:1810.04731
- Connolly, J. A. D. 2009, *Geochemistry, Geophysics, Geosystems*, 10, Q10014
- Cossou, C., Raymond, S. N., & Pierens, A. 2013, *A&A*, 553, L2
- Crossfield, I. J. M., Malik, M., Hill, M. L., Kane, S. R., Foley, B., Polanski, A. S., Coria, D., Brande, J., Zhang, Y., Wienke, K., Kreidberg, L., Cowan, N. B., Dragomir, D., Gorjian, V., Mikal-Evans, T., Benneke, B., Christiansen, J. L., Deming, D., & Morales, F. Y. 2022, *ApJ*, 937, L17
- de Wit, J., Wakeford, H. R., Lewis, N. K., Delrez, L., Gillon, M., Selsis, F., Leconte, J., Demory, B.-O., Bolmont, E., Bourrier, V., Burgasser, A. J., Grimm, S., Jehin, E., Lederer, S. M., Owen, J. E., Stamenković, V., & Triaud, A. H. M. J. 2018, *Nature Astronomy*, 2, 214
- DeFinetti, B. 1926, *Mathematical considerations on Mendelian inheritance* (University of Padua. Statistical Institute)
- Dewaele, A., Loubeyre, P., Occelli, F., Mezouar, M., Dorogokupets, P. I., & Torrent, M. 2006, *Phys. Rev. Lett.*, 97, 215504

- Dittmann, J. A., Irwin, J. M., Charbonneau, D., Bonfils, X., Astudillo-Defru, N., Haywood, R. D., Berta-Thompson, Z. K., Newton, E. R., Rodriguez, J. E., Winters, J. G., Tan, T.-G., Almenara, J.-M., Bouchy, F., Delfosse, X., Forveille, T., Lovis, C., Murgas, F., Pepe, F., Santos, N. C., Udry, S., Wünsche, A., Esquerdo, G. A., Latham, D. W., & Dressing, C. D. 2017, *Nature*, 544, 333
- Dong, C., Jin, M., Lingam, M., Airapetian, V. S., Ma, Y., & van der Holst, B. 2018, *Proceedings of the National Academy of Science*, 115, 260
- Dorn, C., Hinkel, N. R., & Venturini, J. 2017a, *A&A*, 597, A38
- Dorn, C., Khan, A., Heng, K., Connolly, J. A. D., Alibert, Y., Benz, W., & Tackley, P. 2015, *A&A*, 577, A83
- Dorn, C. & Lichtenberg, T. 2021, *ApJ*, 922, L4
- Dorn, C., Venturini, J., Khan, A., Heng, K., Alibert, Y., Helled, R., Rivoldini, A., & Benz, W. 2017b, *A&A*, 597, A37
- Dorogokupets, P. I., Dymshits, A. M., Litasov, K. D., & Sokolova, T. S. 2017, *Scientific Reports*, 7, 41863
- Dorogokupets, P. I., Dymshits, A. M., Sokolova, T. S., Danilov, B. S., & Litasov, K. D. 2015, *Russian Geology and Geophysics*, 56, 172
- Duffy, T., Madhusudhan, N., & Lee, K. 2015, in *Treatise on Geophysics* (Oxford: Elsevier), 149–178
- Duffy, T. S., Zha, C.-S., Downs, R. T., Mao, H.-K., & Hemley, R. J. 1995, *Nature*, 378, 170
- Dunaeva, A. N., Antsyshkin, D. V., & Kuskov, O. L. 2010, *Solar System Research*, 44, 202
- Emsenhuber, A., Mordasini, C., Burn, R., Alibert, Y., Benz, W., & Asphaug, E. 2021, *A&A*, 656, A69
- Essack, Z., Shporer, A., Burt, J. A., Seager, S., Cambioni, S., Lin, Z., Collins, K. A., Mamajek, E. E., Stassun, K. G., Ricker, G. R., Vanderspek, R., Latham, D. W., Winn, J. N., Jenkins, J. M., Butler, R. P., Charbonneau, D., Collins, K. I., Crane, J. D., Gan, T., Hellier, C., Howell, S. B., Irwin, J., Mann, A. W., Ramadhan, A., Shectman, S. A., Teske, J. K., Yee, S. W., Mireles, I., Quintana, E. V., Tenenbaum, P., Torres, G., & Furlan, E. 2023, *AJ*, 165, 47
- Faik, S., Tauschwitz, A., & Iosilevskiy, I. 2018, *Computer Physics Communications*, 227, 117
- Faucher, T. J., Turbet, M., Villanueva, G. L., Wolf, E. T., Arney, G., Kopparapu, R. K., Lincowski, A., Mandell, A., de Wit, J., Pidhorodetska, D., Domagal-Goldman, S. D., & Stevenson, K. B. 2019, *ApJ*, 887, 194
- Fei, Y., Mao, H.-K., & Hemley, R. J. 1993, *J. Chem. Phys.*, 99, 5369
- Feistel, R. & Wagner, W. 2006, *Journal of Physical and Chemical Reference Data*, 35, 1021
- Foreman-Mackey, D., Hogg, D. W., Lang, D., & Goodman, J. 2013, *PASP*, 125, 306
- Fortney, J. J., Marley, M. S., & Barnes, J. W. 2007, *ApJ*, 659, 1661
- Foth, H., Foth, H., & Turk, L. 1972, *Fundamentals of Soil Science*, Wiley international ed (Wiley)
- Frank, M. R., Fei, Y., & Hu, J. 2004, *Geochimica et Cosmochimica Acta*, 68, 2781
- French, M., Mattsson, T. R., Nettelmann, N., & Redmer, R. 2009, *Physical Review B*, 79, 054107
- French, M. & Redmer, R. 2015, *Phys. Rev. B*, 91, 014308
- Fressin, F., Torres, G., Charbonneau, D., Bryson, S. T., Christiansen, J., Dressing, C. D., Jenkins, J. M., Walkowicz, L. M., & Batalha, N. M. 2013, *ApJ*, 766, 81
- Fulton, B. J., Petigura, E. A., Howard, A. W., Isaacson, H., Marcy, G. W., Cargile, P. A., Hebb, L., Weiss, L. M., Johnson, J. A., Morton, T. D., Sinukoff, E., Crossfield, I. J. M., & Hirsch, L. A. 2017, *AJ*, 154, 109

- Galassi, M., Davies, J., Theiler, J., Gough, B., Jungman, G., Alken, P., Booth, M., Rossi, F., & Ulerich, R. 2009, GNU Scientific Library Reference Manual (3rd Ed.) (Network Theory Limited Godalming)
- Genda, H. & Abe, Y. 2005, *Nature*, 433, 842
- Giesting, P. A., Hofmeister, A. M., Wopenka, B., Gwanmesia, G. D., & Jolliff, B. L. 2004, *Earth and Planetary Science Letters*, 218, 45
- Gillon, M., Jehin, E., Lederer, S. M., Delrez, L., de Wit, J., Burdanov, A., Van Grootel, V., Burgasser, A. J., Triaud, A. H. M. J., Opitom, C., Demory, B.-O., Sahu, D. K., Bardalez Gagliuffi, D., Magain, P., & Queloz, D. 2016, *Nature*, 533, 221
- Gillon, M., Triaud, A. H. M. J., Demory, B.-O., Jehin, E., Agol, E., Deck, K. M., Lederer, S. M., de Wit, J., Burdanov, A., Ingalls, J. G., Bolmont, E., Leconte, J., Raymond, S. N., Selsis, F., Turbet, M., Barkaoui, K., Burgasser, A., Burleigh, M. R., Carey, S. J., Chaushev, A., Copperwheat, C. M., Delrez, L., Fernandes, C. S., Holdsworth, D. L., Kotze, E. J., Van Grootel, V., Almléay, Y., Benkhaldoun, Z., Magain, P., & Queloz, D. 2017, *Nature*, 542, 456
- Ginzburg, S., Schlichting, H. E., & Sari, R. 2016, *ApJ*, 825, 29
- . 2018, *MNRAS*, 476, 759
- Gomes, R., Levison, H. F., Tsiganis, K., & Morbidelli, A. 2005, *Nature*, 435, 466
- Gordon, S. & McBride, B. J. 1994, Computer program for calculation of complex chemical equilibrium compositions and applications. Part 1: Analysis (NASA Reference Publication)
- Grande, Z. M., Pham, C. H., Smith, D., Boisvert, J. H., Huang, C., Smith, J. S., Goldman, N., Belof, J. L., Tschauner, O., Steffen, J. H., & Salamat, A. 2022, *Phys. Rev. B*, 105, 104109
- Grasset, O., Schneider, J., & Sotin, C. 2009, *ApJ*, 693, 722
- Grimm, S. L., Demory, B.-O., Gillon, M., Dorn, C., Agol, E., Burdanov, A., Delrez, L., Sestovic, M., Triaud, A. H. M. J., Turbet, M., Bolmont, É., Caldas, A., Wit, J. d., Jehin, E., Leconte, J., Raymond, S. N., Grootel, V. V., Burgasser, A. J., Carey, S., Fabrycky, D., Heng, K., Hernandez, D. M., Ingalls, J. G., Lederer, S., Selsis, F., & Queloz, D. 2018, *A&A*, 613, A68
- Gupta, A. & Schlichting, H. E. 2019, *MNRAS*, 487, 24
- . 2020, *MNRAS*, 493, 792
- Gupta, A. F., Wright, J. T., Robertson, P., Halverson, S., Luhn, J., Roy, A., Mahadevan, S., Ford, E. B., Bender, C. F., Blake, C. H., Hearty, F., Kanodia, S., Logsdon, S. E., McElwain, M. W., Monson, A., Ninan, J. P., Schwab, C., Stefánsson, G., & Terrien, R. C. 2021, *AJ*, 161, 130
- Guthrie, M., Boehler, R., Molaison, J., Haberl, B., dos Santos, A., & Tulk, C. 2019, *Physical Review B*, 99, 184112
- Hakim, K., Rivoldini, A., Van Hoolst, T., Cottenier, S., Jaeken, J., Chust, T., & Steinle-Neumann, G. 2018, *Icarus*, 313, 61
- Haldemann, J., Alibert, Y., Mordasini, C., & Benz, W. 2020, *A&A*, 643, A105
- Hansen, T. C. 2021, *Nature Communications*, 12, 3161
- Harper, M., Weinstein, B., & Simon, C. 2015, Zenodo 10.5281/zenodo.594435
- Harris, C. R., Millman, K. J., van der Walt, S. J., Gommers, R., Virtanen, P., Cournapeau, D., Wieser, E., Taylor, J., Berg, S., Smith, N. J., Kern, R., Picus, M., Hoyer, S., van Kerkwijk, M. H., Brett, M., Haldane, A., del Río, J. F., Wiebe, M., Peterson, P., Gérard-Marchant, P., Sheppard, K., Reddy, T., Weckesser, W., Abbasi, H., Gohlke, C., & Oliphant, T. E. 2020, *Nature*, 585, 357
- Harris, E. K., Montagna, P. A., Douglas, A. R., Vitale, L., & Buzan, D. 2023, *Environmental Monitoring and Assessment*, 195, 40
- Hauck, S. A., Margot, J.-L., Solomon, S. C., Phillips, R. J., Johnson, C. L., Lemoine, F. G.,

- Mazarico, E., McCoy, T. J., Padovan, S., Peale, S. J., Perry, M. E., Smith, D. E., & Zuber, M. T. 2013, *Journal of Geophysical Research (Planets)*, 118, 1204
- Helled, R. & Fortney, J. J. 2020, *Philosophical Transactions of the Royal Society of London Series A*, 378, 20190474
- Heller, R., Harre, J.-V., & Samadi, R. 2022, *A&A*, 665, A11
- Henry, G. W., Marcy, G. W., Butler, R. P., & Vogt, S. S. 2000, *ApJ*, 529, L41
- Heney, L. G., Forbes, J. E., & Gould, N. L. 1964, *ApJ*, 139, 306
- Hermann, A. & Schwerdtfeger, P. 2011, *Phys. Rev. Lett.*, 106, 187403
- Hirose, K., Labrosse, S., & Hernlund, J. 2013, *Annual Review of Earth and Planetary Sciences*, 41, 657
- Hirose, K., Wood, B., & Vočadlo, L. 2021, *Nature Reviews Earth & Environment*, 2, 645
- Hirsch, K. R. & Holzapfel, W. B. 1986, *J. Chem. Phys.*, 84, 2771
- Hirschmann, M. M., Bergin, E. A., Blake, G. A., Ciesla, F. J., & Li, J. 2021, *Proceedings of the National Academy of Science*, 118, e2026779118
- Howe, A. R. & Burrows, A. 2015, *ApJ*, 808, 150
- Hu, R., Friedson, A. J., Sotin, C., Damiano, M., Swain, M., Mischna, M., Turner, N., Chen, P., Kidd, R., West, R., Zellem, R., Kataria, T., Hasagawa, Y., Beichman, C. A., Howard, A., Knutson, H., Yung, Y., Reinhard, C., Brain, D., Kite, E., Rogers, L., Schlichting, H., Planavsky, N., Dawson, R., Johnson, R., Seager, S., & Lyra, W. 2019, *BAAS*, 51, 559
- Huang, C., Rice, D. R., Grande, Z. M., Smith, D., Smith, J. S., Boisvert, J. H., Tschauner, O., Salamat, A., & Steffen, J. H. 2021, *MNRAS*, 503, 2825
- Huang, C., Rice, D. R., & Steffen, J. H. 2022, *MNRAS*, 513, 5256
- Huang, C. X., Shporer, A., Dragomir, D., Fausnaugh, M., Levine, A. M., Morgan, E. H., Nguyen, T., Ricker, G. R., Wall, M., Woods, D. F., & Vanderspek, R. K. 2018, *arXiv e-prints*, arXiv:1807.11129
- Huang, S. & Ormel, C. W. 2021, *arXiv e-prints*, arXiv:2109.10984
- Hunter, J. D. 2007, *Computing in Science & Engineering*, 9, 90
- Iben, Icko, J. & Ehrman, J. R. 1962, *ApJ*, 135, 770
- Ichikawa, H. & Tsuchiya, T. 2020, *Minerals*, 10, 59
- Johansen, A. & Dorn, C. 2022, *A&A*, 662, A19
- Johansen, A. & Lambrechts, M. 2017, *Annual Review of Earth and Planetary Sciences*, 45, 359
- Johansen, A., Mac Low, M.-M., Lacerda, P., & Bizzarro, M. 2015, *Science Advances*, 1, 1500109
- Journaux, B., Kalousová, K., Sotin, C., Tobie, G., Vance, S., Saur, J., Bollengier, O., Noack, L., Rückriemen-Bez, T., Van Hoolst, T., Soderlund, K. M., & Brown, J. M. 2020, *Space Sci. Rev.*, 216, 7
- Kaminsky, F. 2012, *Earth-Science Reviews*, 110, 127
- Kemmer, J., Dreizler, S., Kossakowski, D., Stock, S., Quirrenbach, A., Caballero, J. A., Amado, P. J., Collins, K. A., Espinoza, N., Herrero, E., Jenkins, J. M., Latham, D. W., Lillo-Box, J., Narita, N., Pallé, E., Reiners, A., Ribas, I., Ricker, G., Rodríguez, E., Seager, S., Vanderspek, R., Wells, R., Winn, J., Aceituno, F. J., Béjar, V. J. S., Barclay, T., Bluhm, P., Chaturvedi, P., Cifuentes, C., Collins, K. I., Cortés-Contreras, M., Demory, B. O., Fausnaugh, M. M., Fukui, A., Gómez Maqueo Chew, Y., Galadí-Enríquez, D., Gan, T., Gillon, M., Golovin, A., Hatzes, A. P., Henning, T., Huang, C., Jeffers, S. V., Kaminski, A., Kunimoto, M., Kürster, M., López-González, M. J., Lafarga, M., Luque, R., McCormac, J., Molaverdikhani, K., Montes, D., Morales, J. C., Passegger, V. M., Reffert, S., Sabin, L., Schöfer, P., Schanche, N., Schlecker,

- M., Schroffenegger, U., Schwarz, R. P., Schweitzer, A., Sota, A., Tenenbaum, P., Trifonov, T., Vanaverbeke, S., & Zechmeister, M. 2022, *A&A*, 659, A17
- Kent, B. R. 2013, *PASP*, 125, 731
- Khan, A., Ceylan, S., van Driel, M., Giardini, D., Lognonné, P., Samuel, H., Schmerr, N. C., Stähler, S. C., Duran, A. C., Huang, Q., Kim, D., Broquet, A., Charalambous, C., Clinton, J. F., Davis, P. M., Drilleau, M., Karakostas, F., Lekic, V., McLennan, S. M., Maguire, R. R., Michaut, C., Panning, M. P., Pike, W. T., Pinot, B., Plasman, M., Scholz, J.-R., Widmer-Schnidrig, R., Spohn, T., Smrekar, S. E., & Banerdt, W. B. 2021, *Science*, 373, 434
- Kite, E. S. & Ford, E. B. 2018, *ApJ*, 864, 75
- Knapmeyer-Endrun, B., Panning, M. P., Bissig, F., Joshi, R., Khan, A., Kim, D., Lekić, V., Tauzin, B., Tharimena, S., Plasman, M., Compaire, N., Garcia, R. F., Margerin, L., Schimmel, M., Stutzmann, É., Schmerr, N., Bozdağ, E., Plesa, A.-C., Wiczorek, M. A., Broquet, A., Antonangeli, D., McLennan, S. M., Samuel, H., Michaut, C., Pan, L., Smrekar, S. E., Johnson, C. L., Brinkman, N., Mittelholz, A., Rivoldini, A., Davis, P. M., Lognonné, P., Pinot, B., Scholz, J.-R., Stähler, S., Knapmeyer, M., van Driel, M., Giardini, D., & Banerdt, W. B. 2021, *Science*, 373, 438
- Koll, D. D. B., Malik, M., Mansfield, M., Kempton, E. M. R., Kite, E., Abbot, D., & Bean, J. L. 2019, *ApJ*, 886, 140
- Konacki, M. & Wolszczan, A. 2003, *ApJ*, 591, L147
- Kozlovsky, Y. A. 1982, *Episodes Journal of International Geoscience*, 5, 9
- Kraus, R. G., Hemley, R. J., Ali, S. J., Belof, J. L., Benedict, L. X., Bernier, J., Braun, D., Cohen, R. E., Collins, G. W., Coppari, F., Desjarlais, M. P., Fratanduono, D., Hamel, S., Krygier, A., Lazicki, A., Mcnaney, J., Millot, M., Myint, P. C., Newman, M. G., Rygg, J. R., Sterbentz, D. M., Stewart, S. T., Stixrude, L., Swift, D. C., Wehrenberg, C., & Eggert, J. H. 2022, *Science*, 375, 202
- Kuchner, M. J. & Seager, S. 2005, *arXiv e-prints*, astro
- Kuskov, O. L. & Kronrod, V. A. 2005, *Icarus*, 177, 550
- Kuwayama, Y., Morard, G., Nakajima, Y., Hirose, K., Baron, A. Q. R., Kawaguchi, S. I., Tsuchiya, T., Ishikawa, D., Hirao, N., & Ohishi, Y. 2020, *Phys. Rev. Lett.*, 124, 165701
- Lammer, H., Selsis, F., Ribas, I., Guinan, E. F., Bauer, S. J., & Weiss, W. W. 2003, *ApJ*, 598, L121
- Lay, T., Hernlund, J., & Buffett, B. A. 2008, *Nature Geoscience*, 1, 25
- Lazio, J., Hallinan, G., Airapetian, A., Brain, D. A., Clarke, T. E., Dolch, T., Dong, C. F., Driscoll, P. E., Fares, R., Griessmeier, J. M., Farrell, W. M., Kasper, J. C., Murphy, T., Rogers, L. A., Shkolnik, E., Stanley, S., Strugarek, A., Turner, N. J., Wolszczan, A., Zarka, P., Knapp, M., Lynch, C. R., & Turner, J. D. 2019, *BAAS*, 51, 135
- Lebreton, Y., Montalbán, J., Christensen-Dalsgaard, J., Roxburgh, I. W., & Weiss, A. 2008, *Ap&SS*, 316, 187
- Ledrew, G. 2001, *JRASC*, 95, 32
- Léger, A., Selsis, F., Sotin, C., Guillot, T., Despois, D., Mawet, D., Ollivier, M., Labèque, A., Valette, C., Brachet, F., Chazelas, B., & Lammer, H. 2004, *Icarus*, 169, 499
- Li, R., Youdin, A. N., & Simon, J. B. 2019, *ApJ*, 885, 69
- Lide, D. R. 2002, *Handbook of Chemistry and Physics*, eighty
- Lock, S. J. & Stewart, S. T. 2017, *Journal of Geophysical Research (Planets)*, 122, 950
- Lopez, E. D. & Fortney, J. J. 2013, *ApJ*, 776, 2
- Lopez, T. A., Barros, S. C. C., Santerne, A., Deleuil, M., Adibekyan, V., Almenara, J. M., Arm-

- strong, D. J., Brugger, B., Barrado, D., Bayliss, D., Boisse, I., Bonomo, A. S., Bouchy, F., Brown, D. J. A., Carli, E., Demangeon, O., Dumusque, X., Díaz, R. F., Faria, J. P., Figueira, P., Foxell, E., Giles, H., Hébrard, G., Hojjatpanah, S., Kirk, J., Lillo-Box, J., Lovis, C., Mousis, O., da Nóbrega, H. J., Nielsen, L. D., Neal, J. J., Osborn, H. P., Pepe, F., Pollacco, D., Santos, N. C., Sousa, S. G., Udry, S., Vigan, A., & Wheatley, P. J. 2019, *A&A*, 631, A90
- Luger, R., Sestovic, M., Kruse, E., Grimm, S. L., Demory, B.-O., Agol, E., Bolmont, E., Fabrycky, D., Fernandes, C. S., Van Grootel, V., Burgasser, A., Gillon, M., Ingalls, J. G., Jehin, E., Raymond, S. N., Selsis, F., Triaud, A. H. M. J., Barclay, T., Barentsen, G., Howell, S. B., Delrez, L., de Wit, J., Foreman-Mackey, D., Holdsworth, D. L., Leconte, J., Lederer, S., Turbet, M., Almléaky, Y., Benkhaldoun, Z., Magain, P., Morris, B. M., Heng, K., & Queloz, D. 2017, *Nature Astronomy*, 1, 0129
- Luque, R., Fulton, B. J., Kunimoto, M., Amado, P. J., Gorrini, P., Dreizler, S., Hellier, C., Henry, G. W., Molaverdikhani, K., Morello, G., Peña-Moñino, L., Pérez-Torres, M., Pozuelos, F. J., Shan, Y., Anglada-Escudé, G., Béjar, V. J. S., Bergond, G., Boyle, A. W., Caballero, J. A., Charbonneau, D., Ciardi, D. R., Dufoer, S., Espinoza, N., Everett, M., Fischer, D., Hatzes, A. P., Henning, T., Hesse, K., Howard, A. W., Howell, S. B., Isaacson, H., Jeffers, S. V., Jenkins, J. M., Kane, S. R., Kemmer, J., Khalafinejad, S., Kidwell, R. C., Kossakowski, D., Latham, D. W., Lillo-Box, J., Lissauer, J. J., Montes, D., Orell-Miquel, J., Pallé, E., Pollacco, D., Quirrenbach, A., Reffert, S., Reiners, A., Ribas, I., Ricker, G. R., Rogers, L. A., Sanz-Forcada, J., Schlecker, M., Schweitzer, A., Seager, S., Shporer, A., Stassun, K. G., Stock, S., Tal-Or, L., Ting, E. B., Trifonov, T., Vanaverbeke, S., Vanderspek, R., Villaseñor, J., Winn, J. N., Winters, J. G., & Zapatero Osorio, M. R. 2022, *A&A*, 664, A199
- Luque, R. & Pallé, E. 2022, *Science*, 377, 1211
- Lustig-Yaeger, J., Meadows, V. S., & Lincowski, A. P. 2019, *AJ*, 158, 27
- MacDonald, M. G. & Dawson, R. I. 2018, *AJ*, 156, 228
- MacDonald, M. G., Feil, L., Quinn, T., & Rice, D. 2022, *AJ*, 163, 162
- MacDonald, M. G., Ragozzine, D., Fabrycky, D. C., Ford, E. B., Holman, M. J., Isaacson, H. T., Lissauer, J. J., Lopez, E. D., Mazeh, T., Rogers, L., Rowe, J. F., Steffen, J. H., & Torres, G. 2016, *AJ*, 152, 105
- Madhusudhan, N., Lee, K. K. M., & Mousis, O. 2012, *ApJ*, 759, L40
- Madhusudhan, N., Nixon, M. C., Welbanks, L., Piette, A. A. A., & Booth, R. A. 2020, *ApJ*, 891, L7
- Madhusudhan, N., Piette, A. A. A., & Constantinou, S. 2021, *ApJ*, 918, 1
- Maitre, R., Streckeisen, A., Zanettin, B., Bas, M., Bonin, B., & Bateman, P. 2005, *Igneous Rocks: A Classification and Glossary of Terms: Recommendations of the International Union of Geological Sciences Subcommittee on the Systematics of Igneous Rocks* (Cambridge University Press)
- Marcus, R. A., Sasselov, D., Stewart, S. T., & Hernquist, L. 2010, *ApJ*, 719, L45
- Marcus, R. A., Stewart, S. T., Sasselov, D., & Hernquist, L. 2009, *ApJ*, 700, L118
- Mashuga, C. V. & Crawl, D. A. 1998, *Process Safety Progress*, 17, 176
- Matsui, M. 2010, in *Journal of Physics Conference Series*, Vol. 215, *Journal of Physics Conference Series*, 012197
- Matsui, M., Ito, E., Katsura, T., Yamazaki, D., Yoshino, T., Yokoyama, A., & Funakoshi, K.-i. 2009, *Journal of Applied Physics*, 105, 013505
- Maurus, S. & Plant, C. 2016, in *Proceedings of the 22nd ACM SIGKDD international conference*



- on Knowledge discovery and data mining, 1055–1064
- Mayor, M., Pepe, F., Queloz, D., Bouchy, F., Rupprecht, G., Lo Curto, G., Avila, G., Benz, W., Bertaux, J. L., Bonfils, X., Dall, T., Dekker, H., Delabre, B., Eckert, W., Fleury, M., Gilliotte, A., Gojak, D., Guzman, J. C., Kohler, D., Lizon, J. L., Longinotti, A., Lovis, C., Megevand, D., Pasquini, L., Reyes, J., Sivan, J. P., Sosnowska, D., Soto, R., Udry, S., van Kesteren, A., Weber, L., & Weilenmann, U. 2003, *The Messenger*, 114, 20
- Mayor, M. & Queloz, D. 1995, *Nature*, 378, 355
- Mazevet, S., Licari, A., Chabrier, G., & Potekhin, A. Y. 2019, *A&A*, 621, A128
- McBride, B. J. & Gordon, S. 1996, *Computer Program for Calculation of Complex Chemical Equilibrium Compositions and Applications: Users Manual and Program Description. II* (National Aeronautics and Space Administration, Office of Management ...)
- McDonough, W. F. 2003, *Treatise on Geochemistry*, 2, 568
- McKinnon, W. B., Bagenal, F., & Dowling, T. E. 2004, *Jupiter: The planet, satellites, and Magnetosphere* (Cambridge University Press)
- McSween Jr, H. & Huss, G. 2022, *Cosmochemistry* (Cambridge University Press)
- McSween Jr, H. Y., Binzel, R. P., De Sanctis, M. C., Ammannito, E., Prettyman, T. H., Beck, A. W., Reddy, V., Le Corre, L., Gaffey, M. J., McCord, T. B., et al. 2013, *Meteoritics & Planetary Science*, 48, 2090
- Meier, T. G., Bower, D. J., Lichtenberg, T., Tackley, P. J., & Demory, B.-O. 2021, *ApJ*, 908, L48
- Melosh, H. J. 2007, *Meteoritics & Planetary Science*, 42, 2079
- Michel, A., Haldemann, J., Mordasini, C., & Alibert, Y. 2020, *A&A*, 639, A66
- Mikal-Evans, T. 2022, *MNRAS*, 510, 980
- Mills, S. M., Fabrycky, D. C., Migaszewski, C., Ford, E. B., Petigura, E., & Isaacson, H. 2016, *Nature*, 533, 509
- Miozzi, F., Matas, J., Guignot, N., Badro, J., Siebert, J., & Fiquet, G. 2020, *Minerals*, 10, 100
- More, R. M., Warren, K. H., Young, D. A., & Zimmerman, G. B. 1988, *Physics of Fluids*, 31, 3059
- Mori, Y., Ozawa, H., Hirose, K., Sinmyo, R., Tateno, S., Morard, G., & Ohishi, Y. 2017, *Earth and Planetary Science Letters*, 464, 135
- Mosenfelder, J. L., Asimow, P. D., Frost, D. J., Rubie, D. C., & Ahrens, T. J. 2009, *Journal of Geophysical Research (Solid Earth)*, 114, B01203
- Mousis, O., Deleuil, M., Aguichine, A., Marcq, E., Naar, J., Aguirre, L. A., Brugger, B., & Gonçalves, T. 2020, *ApJ*, 896, L22
- Murphy, C. A., Jackson, J. M., Sturhahn, W., & Chen, B. 2011, *Geophys. Res. Lett.*, 38, L24306
- Myint, P. C., Benedict, L. X., & Belof, J. L. 2017, *J. Chem. Phys.*, 147, 084505
- Neil, A. R. & Rogers, L. A. 2020, *ApJ*, 891, 12
- Nixon, M. C. & Madhusudhan, N. 2021, *MNRAS*, 505, 3414
- Noack, L. & Lasbleis, M. 2020, *A&A*, 638, A129
- Nomura, R., Hirose, K., Uesugi, K., Ohishi, Y., Tsuchiyama, A., Miyake, A., & Ueno, Y. 2014, *Science*, 343, 522
- Norris, C. A. & Wood, B. J. 2017, *Nature*, 549, 507
- Oganov, A. R. & Ono, S. 2004, *Nature*, 430, 445
- Ogihara, M., Kokubo, E., Nakano, R., & Suzuki, T. K. 2022, *arXiv e-prints*, arXiv:2201.08840
- O'Neill, C. & Lenardic, A. 2007, *Geophys. Res. Lett.*, 34, L19204
- Ono, S. & Oganov, A. R. 2005, *Earth and Planetary Science Letters*, 236, 914
- Ormel, C. W., Liu, B., & Schoonenberg, D. 2017, *A&A*, 604, A1

- Owen, J. E. & Wu, Y. 2013, *ApJ*, 775, 105
- Papakonstantinou, J. M. & Tapia, R. A. 2013, *The American Mathematical Monthly*, 120, pp. 500
- Paxton, B., Bildsten, L., Dotter, A., Herwig, F., Lesaffre, P., & Timmes, F. 2011, *ApJS*, 192, 3
- Petigura, E. A., Marcy, G. W., & Howard, A. W. 2013, *ApJ*, 770, 69
- Plotnykov, M. & Valencia, D. 2020, *MNRAS*, 499, 932
- Poirier, J.-P. 2000, *Introduction to the Physics of the Earth's Interior* (Cambridge University Press)
- Pontoppidan, K., Banzatti, A., Bergin, E., Blake, G. A., Brittain, S., Gerin, M., Goldsmith, P., Kral, Q., Leisawitz, D., Lis, D., McClure, M., Milam, S., Melnick, G., Najita, J., Oberg, K., Richter, M., Salyk, C., Wiedner, M., & Zhang, K. 2019, *BAAS*, 51, 229
- Press, W. H., Teukolsky, S. A., Vetterling, W. T., & Flannery, B. P. 2007, *Numerical Recipes 3rd Edition: The Art of Scientific Computing*, 3rd edn. (Cambridge University Press)
- Price, E. M. & Rogers, L. A. 2020, *ApJ*, 894, 8
- Putirka, K. D. & Xu, S. 2021, *Nature Communications*, 12, 6168
- Ravel, G., Bergmann, M., Trubuil, A., Deschamps, J., Briandet, R., & Labarthe, S. 2022, *arXiv e-prints*, arXiv:2201.04371
- Raymond, S. N., Boulet, T., Izidoro, A., Esteves, L., & Bitsch, B. 2018, *MNRAS*, 479, L81
- Rice, D. R., Rasio, F. A., & Steffen, J. H. 2018, *MNRAS*, 481, 2205
- Rice, D. R. & Steffen, J. H. 2023, *MNRAS*
- Rodríguez Martínez, R., Gaudi, B. S., Schulze, J. G., Acuña, L., Kolecki, J., Johnson, J. A., Asnodkar, A. P., Boley, K. M., Deleuil, M., Mousis, O., Panero, W. R., & Wang, J. 2023, *AJ*, 165, 97
- Rogers, J. G., Gupta, A., Owen, J. E., & Schlichting, H. E. 2021, *MNRAS*, 508, 5886
- Rogers, L. A. 2015, *ApJ*, 801, 41
- Rogers, L. A. & Seager, S. 2010, *ApJ*, 712, 974
- Romanowicz, B. 2008, *Nature*, 451, 266
- Sahlmann, J., Lazorenko, P. F., Ségransan, D., Martín, E. L., Queloz, D., Mayor, M., & Udry, S. 2013, *A&A*, 556, A133
- Sakai, T., Dekura, H., & Hirao, N. 2016, *Scientific Reports*, 6, 22652
- Salamat, A., Briggs, R., Bouvier, P., Petitgirard, S., Dewaele, A., Cutler, M. E., Corà, F., Daisenberger, D., Garbarino, G., & McMillan, P. F. 2013, *Physical Review B*, 88, 104104
- Sanchis-Ojeda, R., Rappaport, S., Pallè, E., Delrez, L., DeVore, J., Gandolfi, D., Fukui, A., Ribas, I., Stassun, K. G., Albrecht, S., Dai, F., Gaidos, E., Gillon, M., Hirano, T., Holman, M., Howard, A. W., Isaacson, H., Jehin, E., Kuzuhara, M., Mann, A. W., Marcy, G. W., Miles-Páez, P. A., Montañés-Rodríguez, P., Murgas, F., Narita, N., Nowak, G., Onitsuka, M., Paegert, M., Van Eylen, V., Winn, J. N., & Yu, L. 2015, *ApJ*, 812, 112
- Santerne, A., Brugger, B., Armstrong, D. J., Adibekyan, V., Lillo-Box, J., Gosselin, H., Aguichine, A., Almenara, J.-M., Barrado, D., Barros, S. C. C., Bayliss, D., Boisse, I., Bonomo, A. S., Bouchy, F., Brown, D. J. A., Deleuil, M., Delgado Mena, E., Demangeon, O., Díaz, R. F., Doyle, A., Dumusque, X., Faedi, F., Faria, J. P., Figueira, P., Foxell, E., Giles, H., Hébrard, G., Hojjatpanah, S., Hobson, M., Jackman, J., King, G., Kirk, J., Lam, K. W. F., Ligi, R., Lovis, C., Loudon, T., McCormac, J., Mousis, O., Neal, J. J., Osborn, H. P., Pepe, F., Pollacco, D., Santos, N. C., Sousa, S. G., Udry, S., & Vigan, A. 2018, *Nature Astronomy*, 2, 393
- Santos, N. C., Adibekyan, V., Mordasini, C., Benz, W., Delgado-Mena, E., Dorn, C., Buchhave, L., Figueira, P., Mortier, A., Pepe, F., Santerne, A., Sousa, S. G., & Udry, S. 2015, *A&A*, 580, L13

- Saumon, D., Chabrier, G., & van Horn, H. M. 1995, *ApJS*, 99, 713
- Schäfer, U., Yang, C.-C., & Johansen, A. 2017, *A&A*, 597, A69
- Scheibe, L., Nettelmann, N., & Redmer, R. 2019, *A&A*, 632, A70
- Schlichting, H. E. & Mukhopadhyay, S. 2018, *Space Science Reviews*, 214, 34
- Schoonenberg, D., Liu, B., Ormel, C. W., & Dorn, C. 2019, *Astronomy & Astrophysics*, 627, A149
- Schulze, J. G., Wang, J., Johnson, J. A., Gaudi, B. S., Unterborn, C. T., & Panero, W. R. 2021a, *The Planetary Science Journal*, 2, 113
- . 2021b, *The Planetary Science Journal*, 2, 113
- Schwarzschild, M. 1958, *Structure and evolution of the stars.*, Vol. 2379 (Princeton University Press)
- Scora, J., Valencia, D., Morbidelli, A., & Jacobson, S. 2020, *MNRAS*, 493, 4910
- Seager, S., Kuchner, M., Hier-Majumder, C. A., & Militzer, B. 2007, *ApJ*, 669, 1279
- Serrano, L. M., Gandolfi, D., Mustill, A. J., Barragán, O., Korth, J., Dai, F., Redfield, S., Fridlund, M., Lam, K. W. F., Díaz, M. R., Grziwa, S., Collins, K. A., Livingston, J. H., Cochran, W. D., Hellier, C., Bellomo, S. E., Trifonov, T., Rodler, F., Alarcon, J., Jenkins, J. M., Latham, D. W., Ricker, G., Seager, S., Vanderspeck, R., Winn, J. N., Albrecht, S., Collins, K. I., Csizmadia, S., Daylan, T., Deeg, H. J., Esposito, M., Fausnaugh, M., Georgieva, I., Goffo, E., Guenther, E., Hatzes, A. P., Howell, S. B., Jensen, E. L. N., Luque, R., Mann, A. W., Murgas, F., Osborne, H. L. M., Palle, E., Persson, C. M., Rowden, P., Rudat, A., Smith, A. M. S., Twicken, J. D., Van Eylen, V., & Ziegler, C. 2022, *Nature Astronomy*, 6, 736
- Shah, O., Alibert, Y., Helled, R., & Mezger, K. 2021, *A&A*, 646, A162
- Shaw, G. H. 1986, *J. Chem. Phys.*, 84, 5862
- Shim, S.-H. & Duffy, T. S. 2000, *American Mineralogist*, 85, 354
- Shporer, A., Collins, K. A., Astudillo-Defru, N., Irwin, J., Bonfils, X., Collins, K. I., Matthews, E., Winters, J. G., Anderson, D. R., Armstrong, J. D., Charbonneau, D., Cloutier, R., Daylan, T., Gan, T., Günther, M. N., Hellier, C., Horne, K., Huang, C. X., Jensen, E. L. N., Kielkopf, J., Palle, E., Sefako, R., Stassun, K. G., Tan, T.-G., Vanderburg, A., Ricker, G. R., Latham, D. W., Vanderspek, R., Seager, S., Winn, J. N., Jenkins, J. M., Colon, K., Dressing, C. D., Léepine, S., Muirhead, P. S., Rose, M. E., Twicken, J. D., & Villaseñor, J. N. 2020, *ApJ*, 890, L7
- Simon, J. B., Armitage, P. J., Li, R., & Youdin, A. N. 2016, *ApJ*, 822, 55
- Smith, R. F., Fratanduono, D. E., Braun, D. G., Duffy, T. S., Wicks, J. K., Celliers, P. M., Ali, S. J., Fernandez-Pañella, A., Kraus, R. G., Swift, D. C., Collins, G. W., & Eggert, J. H. 2018, *Nature Astronomy*, 2, 452
- Sotin, C., Grasset, O., & Mocquet, A. 2007, *Icarus*, 191, 337
- Stacey, F. D. & Davis, P. M. 2008, *Physics of the Earth* (Cambridge University Press)
- Stähler, S. C., Khan, A., Banerdt, W. B., Lognonné, P., Giardini, D., Ceylan, S., Drilleau, M., Duran, A. C., Garcia, R. F., Huang, Q., Kim, D., Lekic, V., Samuel, H., Schimmel, M., Schmerr, N., Sollberger, D., Stutzmann, É., Xu, Z., Antonangeli, D., Charalambous, C., Davis, P. M., Irving, J. C. E., Kawamura, T., Knapmeyer, M., Maguire, R., Marusiak, A. G., Panning, M. P., Perrin, C., Plesa, A.-C., Rivoldini, A., Schmelzbach, C., Zenhäusern, G., Beucler, É., Clinton, J., Dahmen, N., van Driel, M., Gudkova, T., Horleston, A., Pike, W. T., Plasman, M., & Smrekar, S. E. 2021, *Science*, 373, 443
- Steffen, M. 1990, *A&A*, 239, 443
- Stemplinger, S., Prévost, S., Zemb, T., Horinek, D., & Dufrêche, J.-F. 2021, *The Journal of Physi-*

- cal Chemistry B, 125, 12054
- Stewart, S., Davies, E., Duncan, M., Lock, S., Root, S., Townsend, J., Kraus, R., Caracas, R., & Jacobsen, S. 2020, in American Institute of Physics Conference Series, Vol. 2272, American Institute of Physics Conference Series, 080003
- Stixrude, L. 2012, Phys. Rev. Lett., 108, 055505
- . 2014, Philosophical Transactions of the Royal Society of London Series A, 372, 20130076
- Stixrude, L. & Lithgow-Bertelloni, C. 2005, Geophysical Journal International, 162, 610
- Struve, O. 1952, The Observatory, 72, 199
- Suissa, G., Chen, J., & Kipping, D. 2018, MNRAS, 476, 2613
- Tchijov, V. 2004, Journal of Physics and Chemistry of Solids, 65, 851
- Thomas, S. W. & Madhusudhan, N. 2016, MNRAS, 458, 1330
- Tody, D. 1986, in Society of Photo-Optical Instrumentation Engineers (SPIE) Conference Series, Vol. 627, Instrumentation in astronomy VI, ed. D. L. Crawford, 733
- Tsai, S.-M., Innes, H., Lichtenberg, T., Taylor, J., Malik, M., Chubb, K., & Pierrehumbert, R. 2021, ApJ, 922, L27
- Tschauner, O., Ma, C., Beckett, J. R., Prescher, C., Prakapenka, V. B., & Rossman, G. R. 2014, Science, 346, 1100
- Tsuchiya, T., Tsuchiya, J., Umemoto, K., & Wentzcovitch, R. M. 2004, Earth and Planetary Science Letters, 224, 241
- Tulk, C. A., Gagnon, R. E., Kiefte, H., & Clouter, M. J. 1997, J. Chem. Phys., 107, 10684
- Turbet, M., Bolmont, E., Ehrenreich, D., Gratier, P., Leconte, J., Selsis, F., Hara, N., & Lovis, C. 2020, A&A, 638, A41
- Uchida, T., Wang, Y., Rivers, M. L., & Sutton, S. R. 2001, J. Geophys. Res., 106, 21,799
- Udry, S., Lovis, C., Bouchy, F., Collier Cameron, A., Henning, T., Mayor, M., Pepe, F., Piskunov, N., Pollacco, D., Queloz, D., Quirrenbach, A., Rauer, H., Rebolo, R., Santos, N. C., Snellen, I., & Zerbi, F. 2014, arXiv e-prints, arXiv:1412.1048
- Unterborn, C. T., Desch, S. J., Haldemann, J., Lorenzo, A., Schulze, J. G., Hinkel, N. R., & Panero, W. R. 2023, ApJ, 944, 42
- Unterborn, C. T., Desch, S. J., Hinkel, N. R., & Lorenzo, A. 2018, Nature Astronomy, 2, 297
- Unterborn, C. T., Kabbes, J. E., Pigott, J. S., Reaman, D. M., & Panero, W. R. 2014, ApJ, 793, 124
- Unterborn, C. T. & Panero, W. R. 2019, Journal of Geophysical Research (Planets), 124, 1704
- Vacher, P., Mocquet, A., & Sotin, C. 1998, Physics of the Earth and Planetary Interiors, 106, 275
- Valencia, D., O’Connell, R. J., & Sasselov, D. 2006, Icarus, 181, 545
- Valencia, D., Sasselov, D. D., & O’Connell, R. J. 2007a, ApJ, 665, 1413
- . 2007b, ApJ, 656, 545
- Van der Velden, E. 2020, The Journal of Open Source Software, 5, 2004
- Vazan, A., Sari, R., & Kessel, R. 2022, ApJ, 926, 150
- Vida, K. & Roettenbacher, R. M. 2018, A&A, 616, A163
- Vinet, P., Ferrante, J., Rose, J. H., & Smith, J. R. 1987, J. Geophys. Res., 92, 9319
- Wagner, W. & Pruß, A. 2002, Journal of Physical and Chemical Reference Data, 31, 387
- Wang, H. S., Liu, F., Ireland, T. R., Brasser, R., Yong, D., & Lineweaver, C. H. 2019, MNRAS, 482, 2222
- Weiss, L. M. & Marcy, G. W. 2014, ApJ, 783, L6
- Wicks, J. K., Smith, R. F., Fratanduono, D. E., Coppari, F., Kraus, R. G., Newman, M. G., Rygg, J. R., Eggert, J. H., & Duffy, T. S. 2018, Science Advances, 4, eaao5864

- Williams, Q. & Knittle, E. 1997, *Physics of the Earth and Planetary Interiors*, 100, 49
- Winters, J. G., Cloutier, R., Medina, A. A., Irwin, J. M., Charbonneau, D., Astudillo-Defru, N., Bonfils, X., Howard, A. W., Isaacson, H., Bean, J. L., Seifahrt, A., Teske, J. K., Eastman, J. D., Twicken, J. D., Collins, K. A., Jensen, E. L. N., Quinn, S. N., Payne, M. J., Kristiansen, M. H., Spencer, A., Vanderburg, A., Zechmeister, M., Weiss, L. M., Wang, S. X., Wang, G., Udry, S., Terentev, I. A., Stürmer, J., Stefánsson, G., Shporer, A., Shectman, S., Sefako, R., Schwengeler, H. M., Schwarz, R. P., Scarsdale, N., Rubenzahl, R. A., Roy, A., Rosenthal, L. J., Robertson, P., Petigura, E. A., Pepe, F., Omohundro, M., Murphy, J. M. A., Murgas, F., Močnik, T., Montet, B. T., Mennickent, R., Mayo, A. W., Massey, B., Lubin, J., Lovis, C., Lewin, P., Kasper, D., Kane, S. R., Jenkins, J. M., Huber, D., Horne, K., Hill, M. L., Gorrini, P., Giacalone, S., Fulton, B., Forveille, T., Figueira, P., Fetherolf, T., Dressing, C., Díaz, R. F., Delfosse, X., Dalba, P. A., Dai, F., Cortés, C. C., Crossfield, I. J. M., Crane, J. D., Conti, D. M., Collins, K. I., Chontos, A., Butler, R. P., Brown, P., Brady, M., Behrmard, A., Beard, C., Batalha, N. M., & Almenara, J.-M. 2022, *AJ*, 163, 168
- Wolf, A. S. & Bower, D. J. 2018, *Physics of the Earth and Planetary Interiors*, 278, 59
- Wu, C. J., Young, D. A., Sterne, P. A., & Myint, P. C. 2019, *J. Chem. Phys.*, 151, 224505
- Young, E. D., Shahr, A., Nimmo, F., Schlichting, H. E., Schauble, E. A., Tang, H., & Labidi, J. 2019, *Icarus*, 323, 1
- Zeng, L., Jacobsen, S. B., Hyung, E., Levi, A., Nava, C., Kirk, J., Piaulet, C., Lacedelli, G., Sasselov, D. D., Petaev, M. I., Stewart, S. T., Alam, M. K., López-Morales, M., Damasso, M., & Latham, D. W. 2021, *ApJ*, 923, 247
- Zeng, L., Jacobsen, S. B., Sasselov, D. D., Petaev, M. I., Vanderburg, A., Lopez-Morales, M., Perez-Mercader, J., Mattsson, T. R., Li, G., Heising, M. Z., Bonomo, A. S., Damasso, M., Berger, T. A., Cao, H., Levi, A., & Wordsworth, R. D. 2019, *Proceedings of the National Academy of Science*, 116, 9723
- Zeng, L. & Sasselov, D. 2013, *Publications of the Astronomical Society of the Pacific*, 125, 227
- Zeng, L., Sasselov, D. D., & Jacobsen, S. B. 2016, *ApJ*, 819, 127
- Zeng, L. & Seager, S. 2008, *PASP*, 120, 983
- Zhang, J. & Rogers, L. 2022, arXiv e-prints, arXiv:2208.06523
- Zhang, J. & Rogers, L. 2023, in *American Astronomical Society Meeting Abstracts*, Vol. 55, *American Astronomical Society Meeting Abstracts*, 368.13

## Curriculum Vitae

### David R. Rice

Planet Interiors and Dynamics; Computational Techniques; Interdisciplinary Collaborations

#### CONTACT INFORMATION

Department of Physics and Astronomy  
University of Nevada, Las Vegas  
Las Vegas, NV 89154, USA

Email: drice986@gmail.com  
Website: davidrrice.github.io  
ORCID: 0000-0001-6009-8685

#### EDUCATION

---

**Ph.D. Astronomy**, University of Nevada, Las Vegas **May 2023**  
**M.S. Astronomy**, University of Nevada, Las Vegas **Dec. 2019**

Dissertation Advisor: Prof. Jason H. Steffen

Dissertation Title: *Inferences of small planets' compositions and interior structures*

M.S. Thesis Title: *The timing of dynamical interactions between planets*

**B.A. Integrated Science with Honors, Physics & Astronomy, and Earth & Planetary Sciences**, Northwestern University, Evanston, IL **Jun. 2016**

Senior Thesis Advisor: Prof. Fred Rasio

#### RESEARCH EXPERIENCE

---

##### **Star & Planet Formation Group**

Nevada Center for Astrophysics, Las Vegas, NV

*Characterizing Planet Interiors* **Aug. 2017–Present**

Developed MAGRATHEA, an open-source interior structure model featuring enhanced flexibility and extensibility. Collaborated with high-pressure physicists and geologists to implement the newest equation of state measurements.

*Timescales of Instabilities in Planetary Systems* **Aug. 2017–Present**

Simulated tens of thousands of planetary systems on Cherry-Creek, UNLV's computer cluster. Determined an inclination criteria for the long-term survival of tightly-packed systems.

##### **Center for Interdisciplinary Exploration & Research in Astrophysics**

Northwestern University, Evanston, IL

*Survival of Closely Packed Planetary Systems* **Jan. 2013–Aug. 2016**

##### **Laboratory for Atmospheric and Space Physics NSF REU**

Southwest Research Institute, Boulder, CO, advised by Dr. Craig DeForest

*Turbulence in the Solar Wind* **Jun. 2014–Aug. 2014**

## AWARDS & CERTIFICATIONS

---

<b>President's Foundation Graduate Research Fellowship, UNLV</b>	<b>2022</b>
<b>Graduate Mentorship Certificate, UNLV</b>	<b>2022</b>
<b>1st Place, GPSA Research Forum Podium Session, UNLV</b>	<b>2021, 2022</b>
<b>Community Engagement Student Service Honorable Mention, UNLV</b>	<b>2021</b>
<b>Donna Weistrop &amp; David B. Shaffer Scholarship, UNLV</b>	<b>2018, 2019</b>
<b>Nevada Space Grant Graduate Fellowship, NASA</b>	<b>2018</b>
<b>Dean's List, Northwestern University</b>	<b>Fall 2013, Fall 2014, Spring 2016</b>
<b>Illinois Undergraduate Space Grant, NASA</b>	<b>2015</b>

## TEACHING EXPERIENCE

---

### **Lab Instructor, University of Nevada, Las Vegas**

Phys. 180L, Mechanics Lab	<b>9 Sections, 5 Terms</b>
Phys. 181L, Electromagnetism Lab	<b>2 Sections, 1 Term</b>
Phys. 151L, General Physics I Lab	<b>6 Sections, 3 Terms</b>
Phys. 152L, General Physics II Lab	<b>5 Sections, 4 Terms</b>

### **SAGA Education Math Teacher, Chicago, IL**

**Aug. 2016–Jun. 2017**

Delivered a daily, individualized, small-group class in algebra and geometry at Phillips Academy High School with 96% low-income students.

## MENTORING

---

### **Undergraduate students**

Tristan Benally	<b>Fall 2021–Present</b>
Rosalie Chaleunsouk	<b>Fall 2021–Fall 2022</b>

## PROFESSIONAL ACTIVITIES, OUTREACH, AND SERVICE

---

### **Workshop/Seminar organizer**

Let's Build a Planet: Improving Interior Models, Rocky Worlds II Conference, 50 break-out session participants	<b>Jul. 2022</b>
Journal Club and Astro Coffee, UNLV	<b>Fall 2018–Spring 2019</b>

### **Journal referee**

The Astrophysical Journal, Monthly Notices of the Royal Astronomical Society, and Publications of the Astronomical Society of Japan.

### **Outreach**

Astronomy on Tap, Las Vegas	<b>Jun. 2018–Present</b>
Founder, Lead Organizer, and Emcee	
Led quarterly events with over 50 attendees per event	

Skype a Scientist	
Invited video Q&A, 5th grade project	<b>Feb. 2022</b>
Invited video lecture, 5th grade class: “Are Exoplanets Habitable?”	<b>Feb. 2021</b>
Invited video lecture, high school astronomy club	<b>Feb. 2021</b>
Invited video lecture, 11th grade physics class	<b>Apr. 2020</b>
STEM Nova Award Scouts Day Camp	<b>Jan. 2022</b>
Science Advisor and Station Organizer	
Dallas Center-Grimes High School	<b>Jan. 2022</b>
Invited lecture, AP Physics class	
Camp Hippocampus Employee Astronomy Night	<b>Sep. 2021</b>
Invited lecture: “Our Cosmic Address”	
Las Vegas Astronomical Society monthly meeting	<b>Jun. 2020</b>
Invited lecture: “Exoplanets”	
The CSN Planetarium Astronomy Q&A livestream	<b>Apr. 2020</b>
Invited lecture: “The Pluto Controversy”	

### Volunteer Service

Judge for AAS Chambliss Student Achievement Awards	<b>Jan. 2023</b>
Judge for Southern NV Regional Science & Engineering Fair	<b>Mar. 2022</b>
Volunteer Observer with Project RECON	<b>Oct. 2021</b>

### COMPUTER SKILLS

---

#### Expert/Proficient

Programming: Python, C++, shell script, Matplotlib, and LaTeX  
Software: Mercury6 and REBOUND (n-body integrators)  
Supercomputing with Cherry Creek, UNLV and QUEST, Northwestern

#### Familiarity

MESA (stellar evolution), IDL, Perl, Perl Data Language, HTML, and ArcGIS

### PUBLICATIONS

---

7. Childs, A. C., Yang, C., Shakespeare, C., **Rice, D.R.**, Steffen, J. H., (2023) *Composition constraints of the TRAPPIST-1 planets from their formation*, Submitted to MNRAS.
6. **Rice, D. R.**, Steffen, J. H., (2023) *Stable lifetime of compact, evenly-spaced planetary systems with non-equal masses*, MNRAS, 10.1093/mnras/stad393
5. Huang, C. H., **Rice, D. R.**, Steffen, J. H., (2022) *MAGRATHEA: An open-source spherical symmetric planet interior structure code*, MNRAS, 513, 5256
4. MacDonald, M. G., Feil, L., Quinn T., **Rice, D. R.**, (2022) *Confirming the 3:2 Resonant Chain of K2-138*, AJ, 163, 162
3. Huang, C., **Rice, D. R.**, Grande, Z. M., Smith, D., Smith, J. S., Boisvert, J. H., Tschauner, O., Salamat, A., Steffen, J. H., (2021) *Implications of an improved water equation of state for water-rich planets*, MNRAS, 503, 2825



2. **Rice, D. R.**, Rasio, F. A., Steffen, J. H., (2018) *Survival of non-coplanar, closely packed planetary systems after a close encounter*, MNRAS, 481, 2205
1. DeForest, C. E., Matthaeus, W. H., Howard, T. A., **Rice, D. R.**, (2015) *Turbulence in the solar wind measured with comet tail test particles*, ApJ, 812, 108

#### INVITED TALKS

---

- |  |                  |
|--|------------------|
| 4. The Ohio State Univeristy, Exoplanet Talk Series                  | <b>Oct. 2022</b> |
| 3. The University of Chicago, Exoplanet Journal Club                 | <b>Oct. 2022</b> |
| 2. Northwestern University, Astro Theory Group                       | <b>Sep. 2022</b> |
| 1. PennState, The Center for Exoplanets and Habitable Worlds Seminar | <b>Sep. 2022</b> |

#### CONTRIBUTED TALKS

---

- |   |                  |
|---|------------------|
| 8. NASA's Exoplanet Modeling and Analysis Center Workshop, Virtual<br>"Solving and visualizing planet interiors with MAGRATHEA"     | <b>Feb. 2023</b> |
| 7. 241st American Astronomical Society Meeting, Seattle, WA<br>"Interior models of small planets"                                   | <b>Jan. 2023</b> |
| 6. Exoplanets IV, Las Vegas, NV<br>"Investigating systematic uncertainties in terrestrial interior models with MAGRATHEA"           | <b>May 2022</b>  |
| 5. Graduate & Professional Student Research Forum, UNLV<br>"Systematic uncertainties in terrestrial interior models with MAGRATHEA" | <b>Apr. 2022</b> |
| 4. Graduate & Professional Student Research Forum, UNLV<br>"Characterizing the composition of small exoplanets"                     | <b>Apr. 2021</b> |
| 3. Habitable Worlds 2 Conference, Online<br>"MAGRATHEA: Terrestrial planet interior solver and the degeneracy of interiors"         | <b>Feb. 2021</b> |
| 2. Chicago Exoplanet Meeting, The University of Chicago, IL<br>"Dynamical instability in exoplanetary systems"                      | <b>Jun. 2015</b> |
| 1. LASP REU, Boulder, CO<br>"Analysis of comet tails for turbulence in the solar wind",   | <b>Jul. 2014</b> |

#### CONTRIBUTED POSTERS

---

- |   |                  |
|---|------------------|
| 5. Rocky Worlds II, Oxford, UK<br>"Investigating systematic uncertainties in terrestrial interior models with MAGRATHEA"                              | <b>Jul. 2022</b> |
| 4. Exoplanets III, Online<br>"MAGRATHEA: Terrestrial planet interior solver and the degeneracy of interiors"  | <b>Jul. 2020</b> |
| 3. Sagan Exoplanet Summer Workshop, Pasadena, CA<br>"Differentiated collisions and their effect on terrestrial planet composition"                    | <b>Jul. 2019</b> |
| 2. Kepler & K2 Science Convention V, Glendale, CA<br>"The effect of differentiated collisions on the interiors of terrestrial planets"                | <b>Mar. 2019</b> |
| 1. 227th American Astronomical Society Meeting, Kissimmee, FL<br>"Understanding dynamical instability in 4-planet systems with equal orbital spacing" | <b>Jan. 2016</b> |

